University of California
Los Angeles

Toward Production of Ultracold Molecular Ions

A dissertation submitted in partial satisfaction
of the requirements for the degree
Doctor of Philosophy in Physics

by

Kuang Chen

2013

Abstract of the Dissertation

Toward Production of Ultracold Molecular Ions

by

Kuang Chen

Doctor of Philosophy in Physics

University of California, Los Angeles, 2013

Professor Eric Hudson, Chair

Ultracold cold molecular ions promise new directions in various studies of fundamental physics, such as precision measurements, ultracold chemistry and quantum information sciences. All these exciting applications require the molecular ion to be prepared at ground state of motional and internal degrees of freedom. It has been proposed that this stringent goal could be achieved through sympathetic cooling via collisions with laser-cooled neutral atoms. Three fundamental issues of this method are addressed in this thesis.

First, an analytical model is established to accurately describe collision-induced heating of a single ion in contact with cold neutral atoms. This model reveals that micromotion interruption is the cause of heating, and gives results about steady-state temperature and sympathetic cooling rate verified by Monte-Carlo simulations. It also provides insight into the power-law tails observed in the energy distribution of the trapped ion.

Next, we consider the case of multiple ions, whose inter-particle Coulomb repulsion causes ions in the Coulomb crystal state to spontaneously melt into a gas phase ion cloud, due to the same micromotion interruption mechanism. The analysis of this problem with a plasma model leads to the experimental determination of a quantity central to plasma physics, *Coulomb Logarithm*, in an ion trap.

Finally, we demonstrate a molecular ion spectroscopy technique through the example of trap-depletion photodissociation of $BaCl^+$. Although not sensitive to rotational structure, this method already reveals much about the fundamental quantum physics in the photodis-

sociation process. The measured cross-section results paves the road toward state-selective spectroscopy currently going on in our lab.

The dissertation of Kuang Chen is approved.

Louis Bouchard

Karoly Holczer

Stuart Brown

Brian Regan

Eric Hudson, Committee Chair

University of California, Los Angeles

2013

Table of Contents

List of Figures

List of Tables

Acknowledgments

First I am greatly grateful to my advisor Eric Hudson. Eric is an excellent mentor and great research supervisor. Just like the way any graduate student look up to his advisor, Eric sets an example of diligent young physicist with a broad knowledge about physics and great passion for science. From him, I also learned to seek practical solutions when the problem at hand is too complicated. Eric is also committed to the growth of his students. He allowed me to travel to conference to explore career opportunities which is very important to me. A good quality in Eric which is not always found in a physics professor is that he pays great attention to build a good bonding relationship between lab members. Because of his efforts, as a foreigner I could feel comfortable hanging around with other lab members just like a big family. There are so many other good qualities in him which I admire, and he will be a role model to me for my future career path.

I would also like to show my gratitude to other lab members. I met Wade Rellergert during my first lab visit, when the lab was only half full as it is now. Wade showed me and later Steven how to built the first ion trap in the lab. He is always relaxed, and he can always explain things in an easy way to me. Steven and I worked together on $BaCl^+$ spectroscopy experiment. The experiment was quite frustrating in the beginning, as no one in the lab knew how to make stable laser ablation target as a source of molecular ions. During the most difficult time of the experiment, we constantly cheered each other up. Having tried so many times with different methods, we finally found the magical recipe for ablation target. I also had the pleasure to work with Scott Sullivan. Scott is a master of handy Mathematica tricks which often give fast results when we discuss physics problems. It is him who found reference to the theory of micromotion interruption that later led to ion-ion heating measurement in ion trap. Although Christian Schneider joined the lab as a post-doc only since last year, he helped me tremendously with parallel Monte Carlo simulations with just a few magical keystrokes. Hanging out and discussing physics with Justin Jeet and Prateek Puri is fun too. Our theory collaborator, Prof. Svetlana Kotochigova and Alexandar Petrov gave us enormous help for $BaCl^+$ photodissociation and predissociation experiment. Their accurate

calculation saved us from many hours of aimless search.

I am extremely indebted to my parents, Yi Chen and Ju Ni. They did everything to ensure I could receive high quality education since childhood. It is this good education in China that made me qualify for admission into the physics Ph.D. program at UCLA physics department. During the six years at UCLA, they have been a constant source of love and support that helped me reach my goals.

I owe a lot to my wife, Jing. When I come home stressed from long hours of work in the lab everyday, she is always there being very supportive. She knows the physics of my emotions and feelings, and always manages to make me relax and recharge so I can continue to work hard the next day. This is not easy at all for her, because she too is struggling for her life as a Ph.D. student both physically and emotionally. I couldn't imagine how weak, stressed and worried I would be when I was lying on the hospital bed in the ICU room of UCLA hospital just two months before graduation, if she were not there at the bedside taking care of me and everything. It is also because of her, I was able to recover so fast after discharge from hospital, put all my publications into a coherent dissertation and survived the dissertation defense. This dissertation is dedicated to her.

Vita

2007	B.S. Physics, Nanjing University, Nanjing, China
2007	Graduate Division Fellowship, UCLA
2007-2009	Teaching Assistant, Department of Physics and Astronomy, UCLA
2009-2013	Research Assistant, Atomic, Molecular and Optical Physics with Professor Eric R. Hudson, UCLA

Publications

Kuang Chen, Steven J. Schowalter, Svetlana Kotochigova, Alexander Petrov, Wade G. Rellergert, Scott T. Sullivan, and Eric R. Hudson, "Molecular-ion trap-depletion spectroscopy of $BaCl^+$", Phys. Rev. A 83, 030501(R) (2011)

Scott T. Sullivan, Wade G. Rellergert, Svetlana Kotochigova, Kuang Chen, Steven J. Schowalter, Eric R. Hudson, "Trapping molecular ions formed via photo-associative ionization of ultracold atoms", Phys. Chem. Chem. Phys. 13, 18859-18863 (2011)

Wade G. Rellergert, Scott T. Sullivan, Svetlana Kotochigova, Alexander Petrov, Kuang Chen, Steven J. Schowalter, Eric R. Hudson, "Measurement of a Large Chemical Reaction Rate between Ultracold Closed-Shell ^{40}Ca Atoms and Open-Shell $^{174}Yb^+$ Ions Held in a Hybrid Atom-Ion Trap", Phys. Rev. Lett. 107, 243201 (2011)

Steven J. Schowalter, Kuang Chen, Wade G. Rellergert, Scott T. Sullivan, and Eric R.

Hudson, "An Integrated Ion Trap and Time-of-Flight Mass Spectrometer for Chemical and Photo-reaction Dynamics Studies", Rev. Sci. Instrum. 83, 043103 (2012)

Wade G. Rellergert, Scott T. Sullivan, Steven J. Schowalter, Svetlana Kotochigova, Kuang Chen and Eric R. Hudson, "Evidence for Sympathetic Vibrational Cooling of Translationally Cold Molecules", Nature 495, 490494 (2013)

Kuang Chen, Scott T. Sullivan, Wade G. Rellergert, Eric R. Hudson, "Measurement of the Coulomb Logarithm in a Radio-Frequency Paul Trap", Phys. Rev. Lett. 110, 173003/1-5 (2013)

CHAPTER 1

Introduction

1.1 Why molecular ions

The twentieth century has witnessed humanity's unprecedented control over atoms, prompted by precise knowledge of the atom's finest structures and revolutionizing techniques such as laser-cooling. It is natural that at the turn of the new century, scientists started to extend these techniques to molecules. Molecule's rotational and vibrational degrees of freedoms, which are not present in atoms, can lead to exciting possibilities for study of fundamental physics. For example, the sensitivity to parity-violating effects [10, 11, 12, 13], or variation of fundamental constants [14, 15, 16] are enhanced in certain molecules, which can be revealed by high-resolution molecular spectroscopy. The anisotropic dipole-dipole interactions [17] between molecules means enormous opportunities for experimentally exploring novel phases of matter [18, 19]. Furthermore, the long-lived rotational states in molecules coupled with this dipole-dipole interactions, are promising candidates for quantum computations [20, 21].

Most of these potential applications require high phase-space density [22], which generally means molecules need to be kept at an extremely low translational temperature, and internally molecules need to be cooled to the ro-vibrational ground state. Now the complicated molecular structure poses a series of challenges. The general lack of cycling transitions in most molecules makes laser-cooling, the routine method to prepare translationally cold atoms samples, limited to only a few molecules species with diagonal Frank-Condon factors (FCFs) [23, 24]. Photoassociation from laser-cooled atoms successfully achieved the goal of making cold molecules in a single ro-vibrational state [25]. Nevertheless it is only applicable to atoms that can be laser cooled, and therefore not amenable to many of the precision mea-

surement and quantum computation/information experiments. Buffer gas cooling, another technique that relies on cooling from heat exchange of molecules with helium [26], often results in relatively warm temperature and low density.

Molecular ions, on the other hand, offers an alternative to achieving the aforementioned ambitious goals for neutral molecules. Trapping molecular ions in quadrupole ion trap only relies on the ion's mass-to-charge ratio, thus a much broader range of ions could be potentially used. Quadrupole ion traps also have a large trap depth, and typical trap time of minutes have been observed. The trapping potential is independent of the molecule's internal state, which could help to achieve a long coherence time for quantum computation/information experiments. Therefore most of the applications of neutral molecules find their counterpart in molecular ions [27, 28, 29, 30]. Despite these advantages, the problem of preparing internally and externally cold samples of molecular ions still needs to be addressed.

1.2 Sympathetic cooling of molecular ions using neutral atoms

Various theoretical and experimental effort has been carried out to solve this problem. First, certain types of molecular ion species have been proposed as candidate for direct laser-cooling [31, 32], or experimentally produced using threshold photoionization of neutral molecules [33]. Same as the case in neutral molecules these methods are not amenable to any general molecular ion species and typically require a few more repump lasers.

Sympathetic cooling of molecular ions with laser-cooled co-trapped atomic ion is a species non-specific method. The Coulomb interaction with the coolant ions quickly reduce the molecular ions' kinetic energy, and an ordered structure called Coulomb crystal is formed with a typical temperature less than 100 mK desirable for various precision spectroscopy experiment [34, 35, 36, 27], shown in Fig. 1.1. However, the long-range nature of the Coulomb repulsion also prevents molecular ions and coolant atomic ions from approaching each other close enough to make internal state relaxation happen effectively [37], leaving the rotational temperature at $\sim$ 300K. Subsequent optical pumping schemes [1, 38] can further lower the rotational temperature to $\sim$ 20K (shown in Fig. 1.2), limited by redistribution of

population due to the black-body radiation.

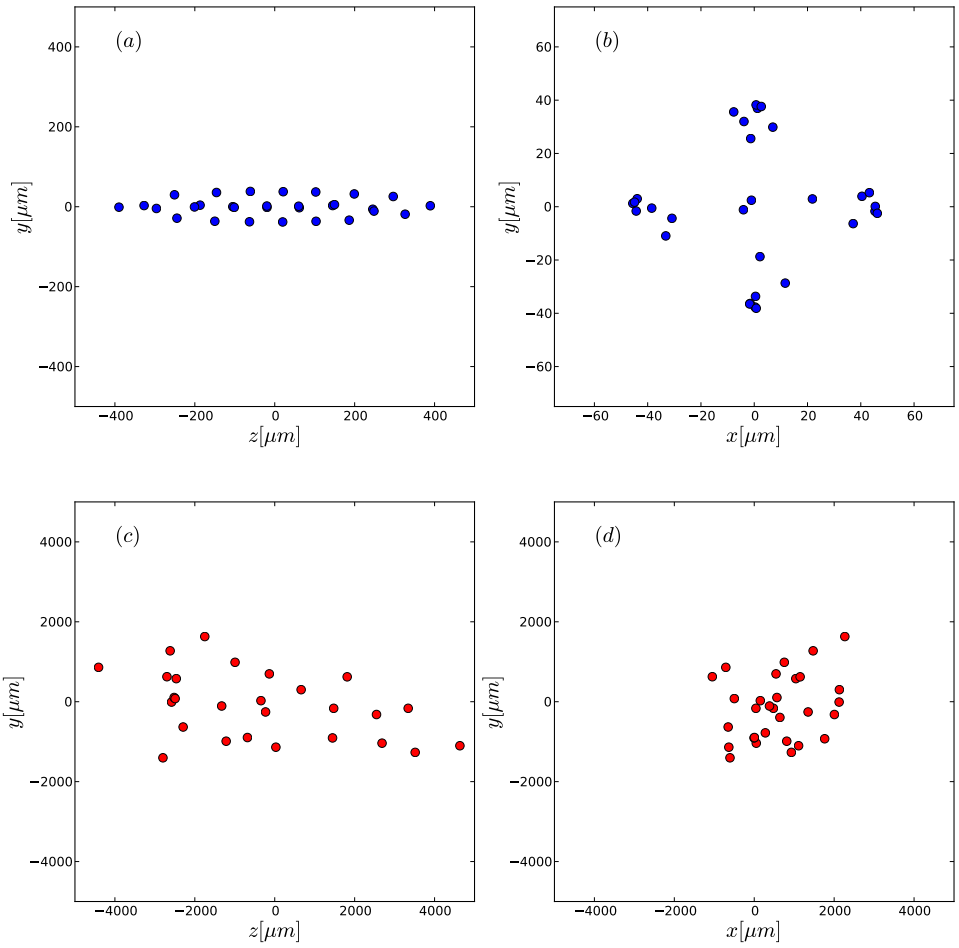

Figure 1.1: Simulation results of 30 trapped ions in the form of Coulomb crystal at temperature of $\sim$ mK shown in panel a (axial view) and b (side view). For comparison, the same ions in gas phase at temperature of 300K are shown in panel c and d. Note the change of figure scale.

In 2009, we proposed that sympathetic cooling with laser-cooled *neutral* atoms is capable of providing both external and internal relaxation [39]. The key ingredient is to replace the Coulomb repulsion $V(r) \sim \frac{1}{r}$, by the attractive potential induced from the polarization of

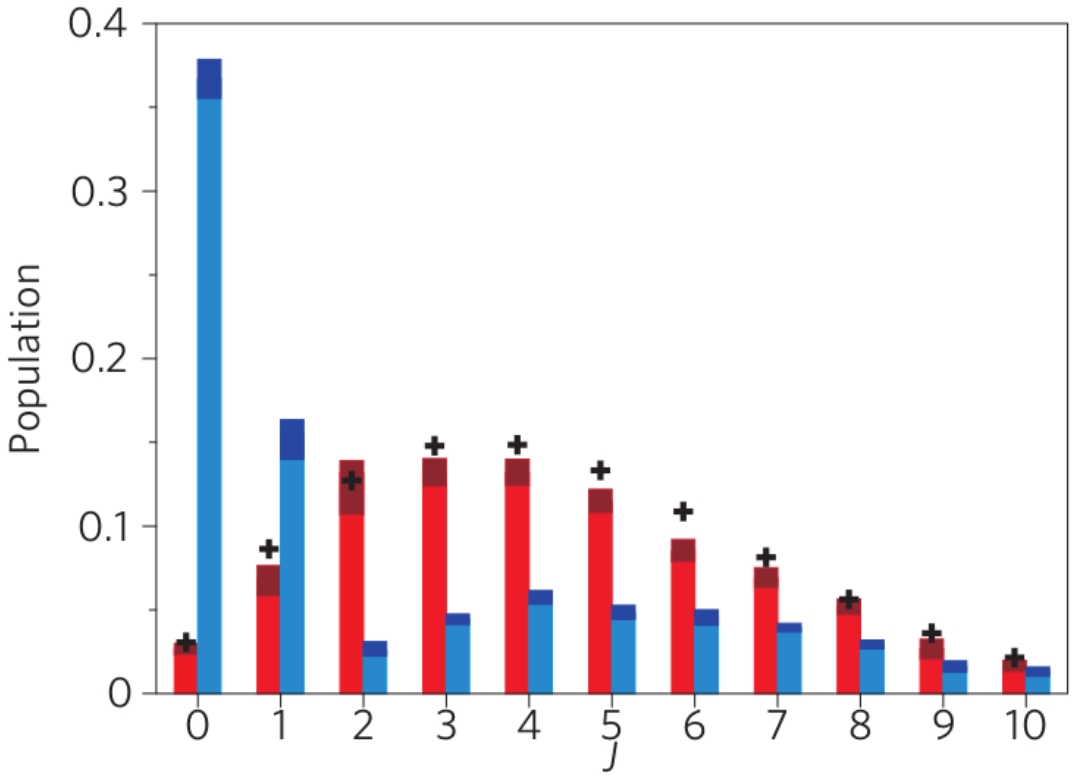

Figure 1.2: Population distribution on rotational states of MgH^+ in a Coulomb crystal co-trapped with Mg^+. Red and blue bars are population before and after optical pumping schemes, respectively. A thermal distribution at 293K is presented by crosses. Figure taken from [1].

the coolant atom by the charge of the molecular ion,

$$V(r) = -\frac{1}{2}\alpha E(r)^2 \equiv -\frac{C_4}{2r^4} \tag{1.1}$$

where $E(r) = \dfrac{e}{4\pi\epsilon_0 r^2}$ is a singly-charged ion's electric field at distrance r from the atom, and α is atom's polarizability. Compared to earlier experimental studies where helium was used as the coolant atom [40], laser-cooled atoms have a much larger polarizability. For the particular choice of neutral atom, *i.e.* Ca, $\alpha_{\mathrm{Ca}} \sim 100\alpha_{\mathrm{He}}$ [41]. As a result, this attractive potential greatly enhances the chance that the molecule-atom complex tunnel into short separation, also known classically as Langevin capture [42].

Recent measurement in a hybrid system shows near unit probability of inelastic collision happening once the complex is in short separation [43, 44, 45, 9]. For the $BaCl^+$ and Ca

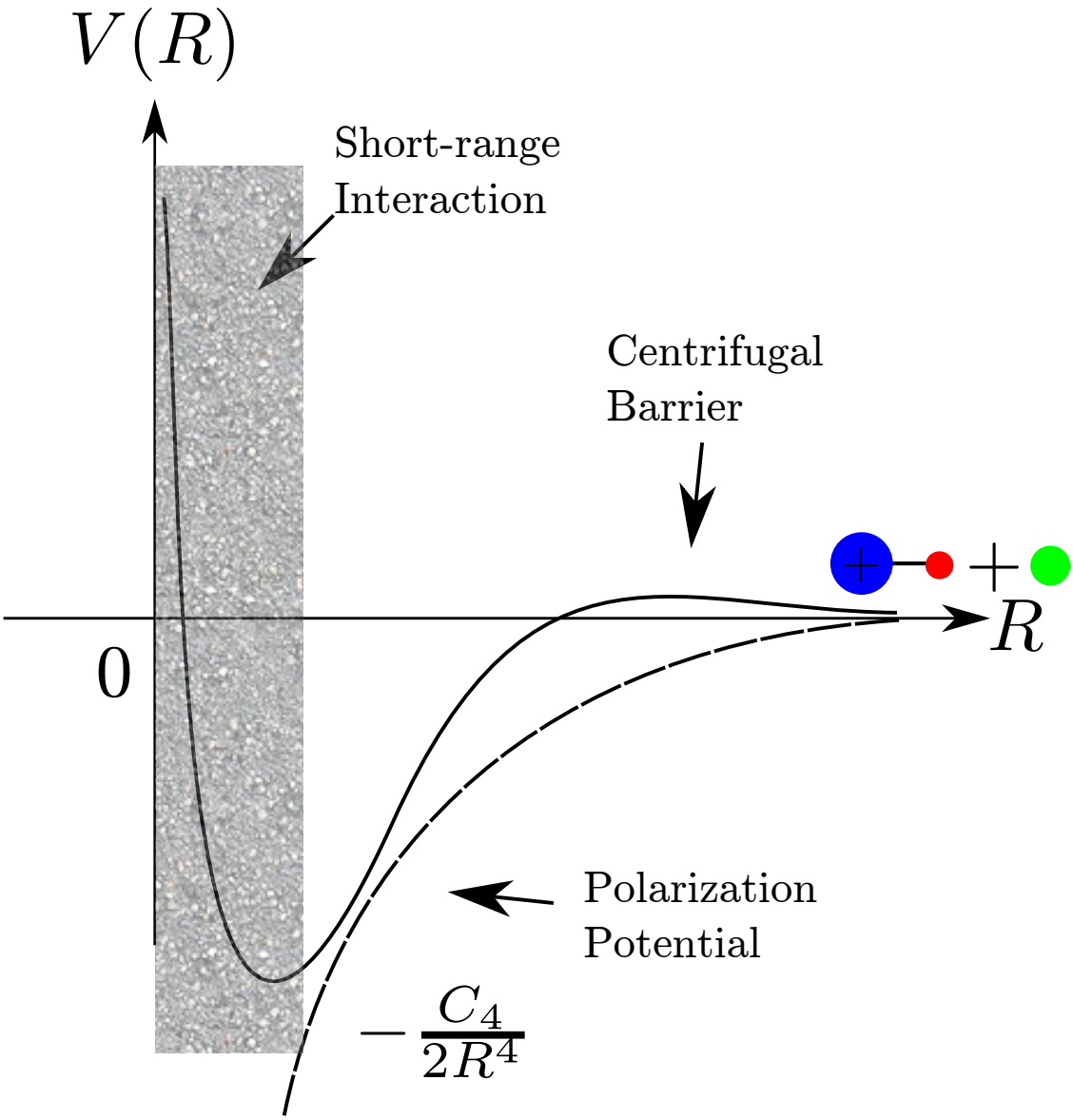

Figure 1.3: Interaction potential between molecular ion and neutral atom. The gray rectangle indicated the range of separation where inelastic collisions happen.

system, undesirable inelastic collision channels, including charge-exchange and substitution, are energetically forbidden [39]. Thus vibrational and rotational relaxations are expected to occur with high efficiency for $BaCl^+$ and Ca system.

1.3 Challenges

Many theoretical and experimental challenges are associated with producing cold molecular ions. First of all, compared to neutral atoms, there is a relative paucity of spectroscopic data on molecular ions [46, 47], which is critial for characterizing the population on each individual ro-vibrational level of the molecular ion to prove if our method works. In particular, the spectroscopic knowledge about rotational states are important for future experiments where microwaves are used to manipulate the rotational levels [48] of molecular ions as qubits.

For $BaCl^+$, despite the observation that it has similar electronic structure to alkaline-earth chalcogens and an ionically bonded complex of two closed-shell atoms ($M^{2+}X^-$), there is no spectroscopic information of $BaCl^+$ available to us. Due to space-charge effects, realistic ion traps can only trap $10^3 \sim 10^4$ ions [49], a number difficult for many conventional spectroscopic methods [50] on neutral molecules. Based on these observations, we performed (crude) photodissication spectroscopy of $BaCl^+$ [51] as the first step toward a fully resolved ro-vibrational $BaCl^+$ spectrum. As shown in Chapter 5, with this information, very important results regarding vibrational relaxation [9] have already been found.

Second, the kinetics in ion trap have not yet been fully understood. In the simplest case of sympathetic cooling of a single ion, ion's trajectory is constantly interrupted due to collisions with laser-cooled atoms. But quite contrary to the classical Brownian motion, collisions in ion trap could on average lead to dramatic exponential-like heating of the ion, which is certainly detrimental to any ultracold molecular ion experiment! Thus a quantitative understanding ion's kinetics is fundamental to the design, optimization and interpretation of both the cold molecular ion experiment, and the recent surge of ultracold quantum chemistry experiments in hybrid traps [43, 52, 53, 54, 55, 9, 45, 56, 44, 57]. Futher, the significance of this understanding reaches beyond the scope of atomic physics, to areas including fundamental thermodynamics and statistical physics.

Finally, it is observed that multiple atomic ions trapped and initialized at a Coulomb crystal state will spontaneously heat and melt into liquid and gas phase after active laser-cooling is turned off. Since the inter-particle force is the same in the molecular ions, similar

heating phenomenon is expected to exist in the preparation cold molecular ion crystals, causing problems in ion based quantum computation experiments. Microscopically, this heating phenomenon is explained as a result of interruption of one ion's micromotion by a collision with another nearby ion. Nevertheless, due to the long-range nature of the Coulomb force, the microscopic understanding of single ion kinetics need to be combined with plasma physics model to solve this complicated this many-body problem [58]. From the perspective of plasma physics, trapped ions in Coulomb crystals realize a strongly-coupled one-component plasma, which is not often explored by plasma physicists. Therefore, the study of heating of trapped ions could provide additional insights for plasma physics.

1.4 Dissertation Outline

The overall structure of the dissertation takes the form of six chapters. As the common theme of the following chapters, we first review the basic theory of ion trapping and detection in Chapter 2. In Chapter 3, we present our experiment result on the direct photodissociation spectroscopy of $BaCl^+$. Then we switch gears to show our analytic theory of sympathetic cooling of single ion by neutral gas, along with comparison with numerical simulations in Chapter 4. Chapter 5 connects the problem of self-heating phenomenon of multiple trapped ions to an experimental measurement of the quantity *Coulomb logarithm* in plasma physics. In Chapter 6, we briefly explain some ongoing experiment and theoretical efforts. For the ease of reading, some technical details are arranged into the appendix.

CHAPTER 2

Review of Ion Trapping and Detection

2.1 Ion Trapping

Trapping, i.e. containing a particle within a given volume, generally relies on the existence of a restoring force and thus a *static* confining potential in its simplest form

$$V(\mathbf{r}) = \frac{m}{2}(\omega_x^2 x^2 + \omega_y^2 y^2 + \omega_z^2 z^2) \tag{2.1}$$

where $\omega_{x,y,z}$ are the oscillation frequency. This is the foundation of a vast majority of particle trapping techniques, including the magneto-optical trap [59], the magnetic trap [60], the optical dipole trap [61] and so on.

However, trapping an ion of charge e in a charge-free space using static electric potentials turns out to be impossible. Proved by Earnshaw [62], a confining potential in the form of Eq. 2.1 violates $\nabla\phi(\mathbf{r}) = \nabla V(\mathbf{r})/e = 0$, the zero gradient of electric potential in vacuum dictated by Maxwell's equation. In other words, a static trapping potential can at best create a saddle potential for the ion. Focused in $x - y$ dimensions, the ion is de-focused in the z dimension.

Nevertheless, trapping is still possible if the field is made to oscillate in time. In this case, the time-dependent potential prevents the ion from leaking out by rapidly flipping the sign of potential, and the ion has stable trajectories in each direction. The alternating feature of the trapping field is imprinted onto the ion's motion, which leads to distinct features in ion's kinetics that are not seen in static trapping. The details of ion's motion, along with the physical trapping device are described in the following sections.

2.1.1 Linear Quadrupole Trap

The trapping field is created by a **L**inear **Q**uadrupole **T**rap (LQT), a device which usually consists of four parallel electrodes and two end-caps. Shown in Fig. 2.1, radio-frequency (rf) [1] applied to the four electrodes create a quadrupole field that provides trapping in the radial direction. Axial confinement on the other hand is accomplished by a dc voltage applied onto two end-caps.

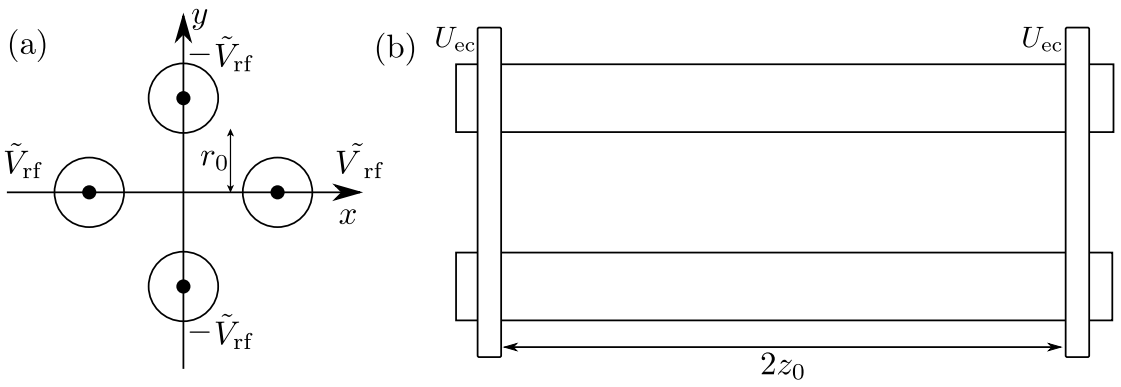

Figure 2.1: Schematic of a linear quadrupole trap viewed from axial direction (panel a), and from side (panel b).

From the superposition principle, the electric potential $\phi(\mathbf{r},t)$ near the center of the trap is the sum of two parts,

$$\phi(\mathbf{r},t) = \phi_1(\mathbf{r},t) + \phi_2(\mathbf{r},t) \tag{2.2}$$

where $\phi_1(\mathbf{r},t)$ and $\phi_2(\mathbf{r},t)$ electric potential due to the electrodes and endcaps respectively. Under the quadrupole approximation, the potentials are given by

$$\phi_1(\mathbf{r},t) = \frac{\tilde{V}_{rf}}{r_o^2}(x^2-y^2) = \frac{V_{rf}}{r_o^2}(x^2-y^2)\cos(\Omega t) \tag{2.3}$$

$$\phi_2(\mathbf{r},t) = \frac{\alpha U_{ec}}{z_o^2}\left(z^2 - \frac{1}{2}(x^2+y^2)\right) \tag{2.4}$$

where r_o is the field radius, z_o is the distance from trap center to the end cap used for axial confinement, V_{rf} and U_{ec} are the radio-frequency (rf) and end cap voltages, respectively, Ω is the radial frequency of the rf voltage, and α is a geometric factor less than unity.

[1] Canonical operation of LQT also involves a static (dc) voltage on the four parallel electrodes. However, the trap in our lab is usually operated with this voltage set to zero.

2.1.2 Equation of Motion, Mathieu Functions

Ion's trajectory in the trap is described by Newton's equation $m\ddot{\mathbf{r}} = -e\nabla\phi$, which can be simplified into

$$\frac{d^2 r_j}{d\tau^2} + (a_j - 2q_j(\cos 2\tau))r_j = 0, \tag{2.5}$$

where $\tau = \frac{\Omega}{2}t$ and $j = x, y, z$. The Mathieu parameters a_j and q_j are given by $\{a_x, a_y, a_z\} = \{a, a, -2a\}$ and $\{q_x, q_y, q_z\} = \{q, -q, 0\}$ with $q = \frac{4eV_{rf}}{mr_0^2\Omega^2}$ and $a = -\frac{4\alpha eU_{ec}}{mz_0^2\Omega^2}$, where m is the ion mass. The fact that the equation of motion depends only on the combination of m/e is the cornerstone of quadrupole mass-spectrometry.

The general solution to Eq. 2.5 is a linear superposition of two real orthogonal Mathieu functions $c(a_j, q_j, \tau)$ and $s(a_j, q_j, \tau)$,

$$\begin{aligned} r_j(\tau) &= A_j\ c_j(\tau) + B_j\ s_j(\tau) \\ v_j(\tau) &= A_j\ \dot{c}_j(\tau) + B_j\ \dot{s}_j(\tau) \end{aligned} \tag{2.6}$$

where the coefficient A_j, B_j are set by initial conditions.

2.1.3 Secular Motion and Micromotion

The dynamical system described by Eq. 2.5 has a periodic coefficient. By the Floquet theorem, the solutions to Eq. 2.5 have a discrete Fourier spectrum [63],

$$c_j(\tau) + \imath s_j(\tau) = \sum_{n=-\infty}^{\infty} C_{2n} e^{\imath(\beta_j + 2n)\tau} \tag{2.7}$$

The $n = 0$ term corresponds to the 'typical' motion of a harmonic oscillator – i.e. the secular ion motion. Correspondingly, keeping only this term in the Fourier transformation of Mathieu sine and cosine functions is dubbed "*secular approximation*". The remaining terms with $n \neq 0$ represent the component of the ion motion driven by the rf field – i.e. the so-called micromotion. Shown in Fig. 2.2 is a sample trace of the ion's trajectory, where the fast micromotion appears as the wiggles on top of the slow secular motion.

The frequency of the secular motion is given by $\omega_j = \frac{\Omega}{2}\beta_j$, where β_j is the so-called

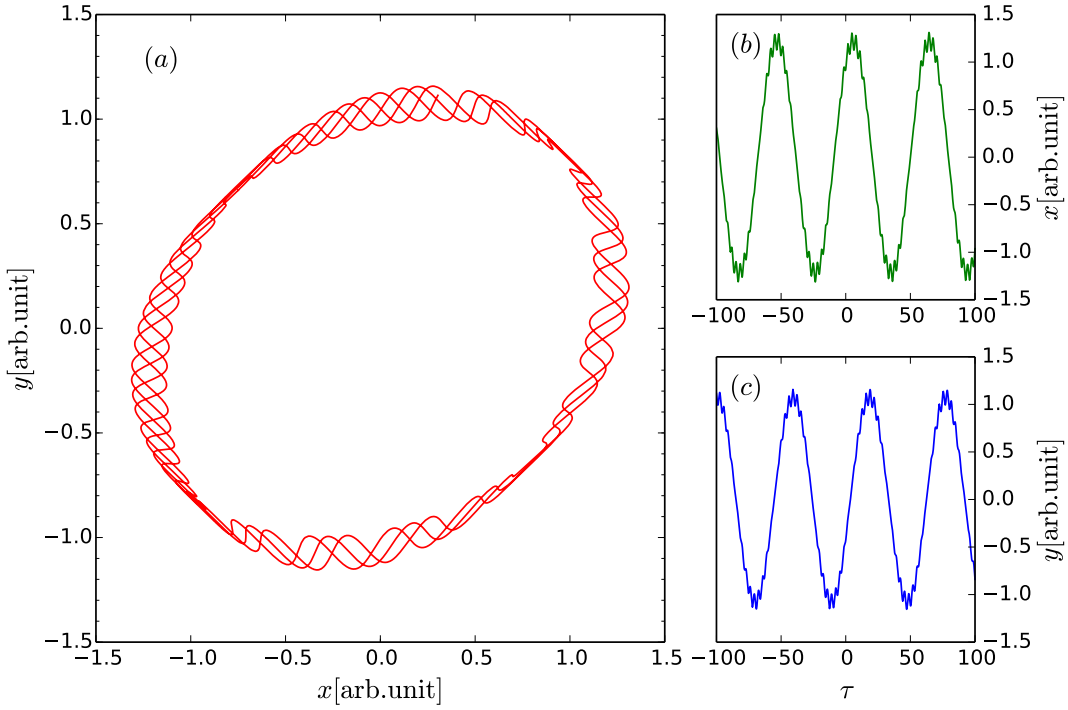

Figure 2.2: A sample trace of ion's trajectory in $x-y$ plane (panel a). x and y component are presented in panel b and c respectively. Mathieu parameters $a = 0$ and $q = 0.15$.

Mathieu characteristic exponent. β_j can be found numerically [64],

$$\beta_j^2 = a_j - \frac{(a_j-1)q_j^2}{2(a_j-1)^2 - q_j^2} - \frac{(5a_j+7)q_j^4}{32(a_j-1)^3(a_j-4)} - \frac{9(a_j^2+58a_j+29)q_j^6}{64(a_j-1)^5(a_j-4)(a_j-9)} + \mathcal{O}(q_j^8) \quad (2.8)$$

For ion traps operating at $a = 0$ and $q < 0.4$ values, Eq. 2.8 is further simplified into

$$\beta_j \approx \frac{q_j}{\sqrt{2}} \quad (2.9)$$

and keeping the expansion Eq. 2.7 to $n = \pm 1$, we have

$$r_j \sim (1 + \frac{q_j}{2}\cos(2\tau))(A_j \cos(\beta_j \tau) + B_j \sin(\beta_j \tau)) \quad (2.10)$$

2.1.4 Stability Region

It can be seen that β_j in Eq. 2.8 is real only for certain values of (a, q). For these trap parameters, the ion has stable trajectories in the trap. Otherwise the imaginary part of β_j

causes $c_j(\tau)$ and $s_j(\tau)$ to diverge, and experimentally the ion escapes the trap after just a few rf cycles. Shown as the shaded region in Fig. 2.3, the lowest order stability region of an ion trap defines values of (a, q), for which an ion would have stable trajectories *simultaneously* in all three dimensions.

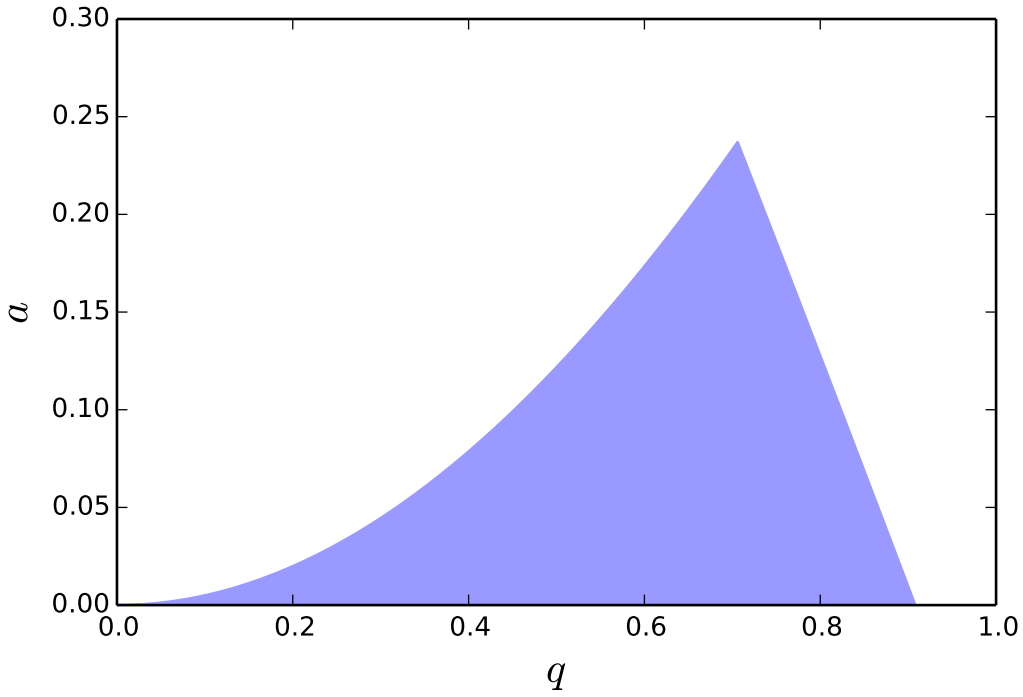

Figure 2.3: LQT stability region indicated by the blue region.

The universality of the stability region is useful in many ways. For instance, the boundary of the stability region ends at $q_{max} \approx 0.908$. Therefore, the mass-to-charge ratio of an unknown ion species m can be inferred from the maximum value of V_{rf} that can still trap ion [3] through the following relation,

$$\frac{4eV_{\text{rf},max}}{mr_0^2\Omega^2} = q_{max} \tag{2.11}$$

Explained in Chapter 5, the stability region can also be used to selectively load or remove certain ion species, by properly setting or ramping the (a, q) parameters [51].

2.1.5 Trap Depth

Even for Mathieu parameters (a, q) inside the stability region, an ion can still escape the trap if its energy exceeds the depth of the trap D. Under secular approximation D is given by [65]

$$D_{x,y} = \frac{m}{2}\omega_{x,y}^2 r_0^2 = \frac{qV_{\mathrm{rf}}}{4} \tag{2.12}$$

$$D_z = \frac{m}{2}\omega_z^2 z_0^2 = \alpha U_{ec} \tag{2.13}$$

Typical values of $D_{x,y}$ and D_z is on the order of $10^3 \sim 10^4$ K. Note this trap depth is large compared to other types of trap [61] (depth of magneto-optical trap ~ 1 K , magnetic trap $\sim 100m$K, optical trap $\sim m$K). This large trap depth makes it straightforward to load and trap ions. For instance, 10^3 ions with a typical translational temperature of 10^3 K [51, 9] can be routinely loaded from the laser ablation plume of a target.

2.2 Ion Detection

Detection of trapped ions generally falls into two categories: the destructive method which detects using a channel electron multiplier (channeltron), and non-destructive method which detects the ion's fluorescence.

2.2.1 Channeltron Detection

In this method, ions extracted from the trap hit the multiplier under a voltage gradient. The incident charges impinging on multiplier's surface is amplified through the repeated processes of secondary emission, thus making the gain of detection very large. However, channeltron detection by itself is not capable of identifying ion species, an important task in molecular ion experiment. For this reason, channeltron detection is usually combined with various other techniques to differentiate ion species.

One technique is resonance excitation, where a small tickle AC voltage (typically a few volts) in resonance with ion's secular frequency ω_j is applied to the ion trap electrodes [49, 2].

As a result, ion's secular motion energy is excited beyond the trap depth D, causing the ion to escape the trap. This trap loss is selective, because ω_j depends on the specific mass of the ion. Shown in Fig. 2.4 is the secular excitation spectrum for Ca_2^+ (m=80 amu) from Ref [2], demonstrating decent accuracy of this method.

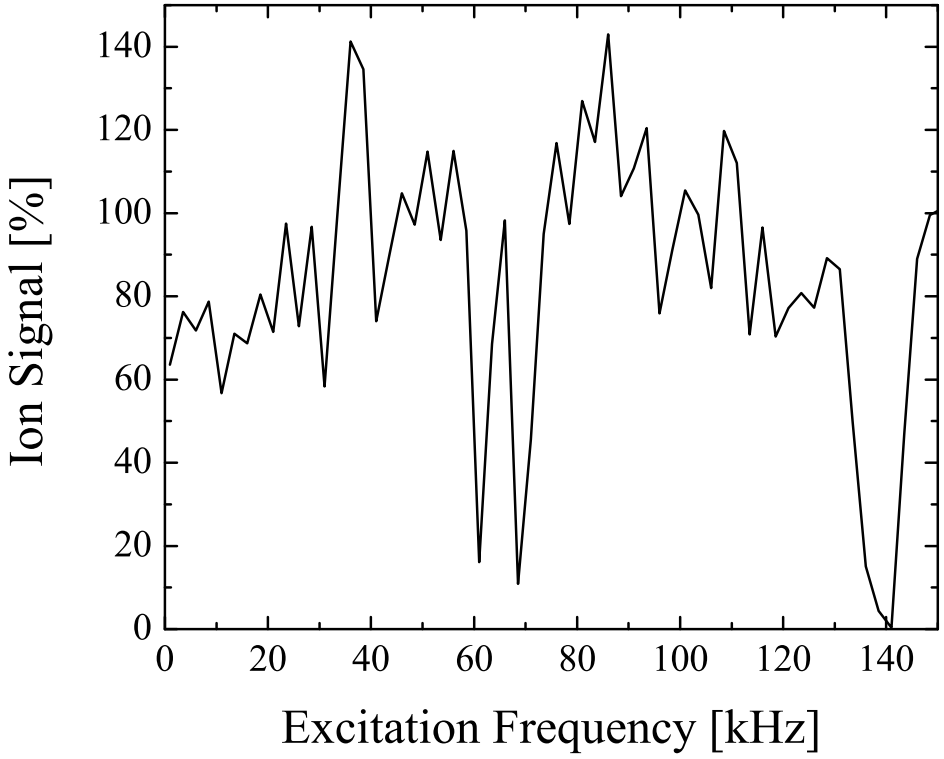

Figure 2.4: Secular excitation spectrum taken from Ref [2]. The observed loss near 70 KHz (and its second harmonic at 140 KHz) is within 10% of the predicted secular frequency for Ca_2^+ ($m = 80$ amu). The split peak feature is likely due to trap imperfections.

Another technique is time-of-flight mass spectrometry. In this method, ions are first rapidly accelerated to the same energy E over a short distance, and they drift freely a long distance of l to reach the channeltron detector. The arrival time of ion species i is connected to its mass m_i through

$$t_i = \frac{l}{v_i} = l\sqrt{\frac{m_i}{2E}} \tag{2.14}$$

Thus, the mass of an unknown species can be inferred from its time-of-flight by

$$m_i = m_c \left(\frac{t_i}{t_c}\right)^2 \tag{2.15}$$

where m_c and t_c is the (pre-determined) calibration ion's mass and its time-of-flight.

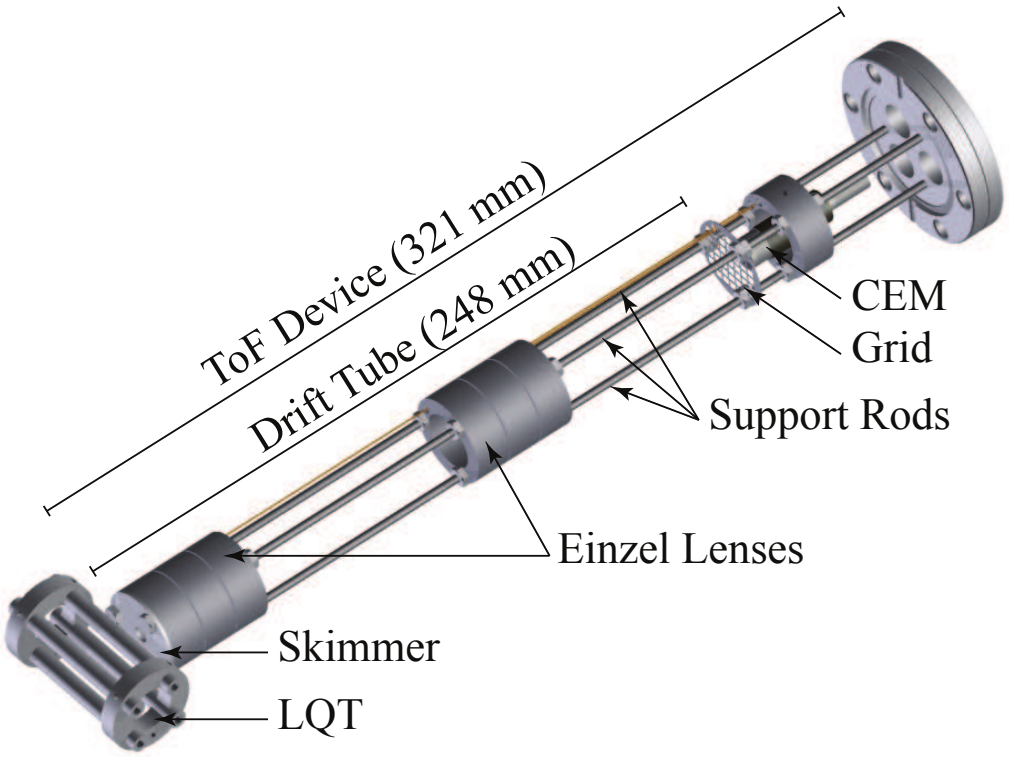

Figure 2.5: A 3D model of the LQT-ToF device, taken from Ref. [3]

Based on this principle, an integrated ion trap and time-of-flight (LQT-ToF) spectrometer [3] (shown in Fig. 2.5) has been constructed in our lab for chemical and photo-reaction dynamical studies. Trapped ions are extracted radially into the drift tube by a two-stage acceleration scheme, and register voltage signals on the channeltron as shown in Fig. 2.6. Near isotope resolution for atomic and molecular ions with masses of a few 100 amu has been achieved. Equipped with the resolving capability of LQT-ToF, we measured the photodissociation (listed in Eq. 2.16) cross-section of $BaCl^+$ with almost 100 times more precisely than in Ref. [51].

$$BaCl^+ + h\nu \rightarrow Ba^+ + Cl \tag{2.16}$$

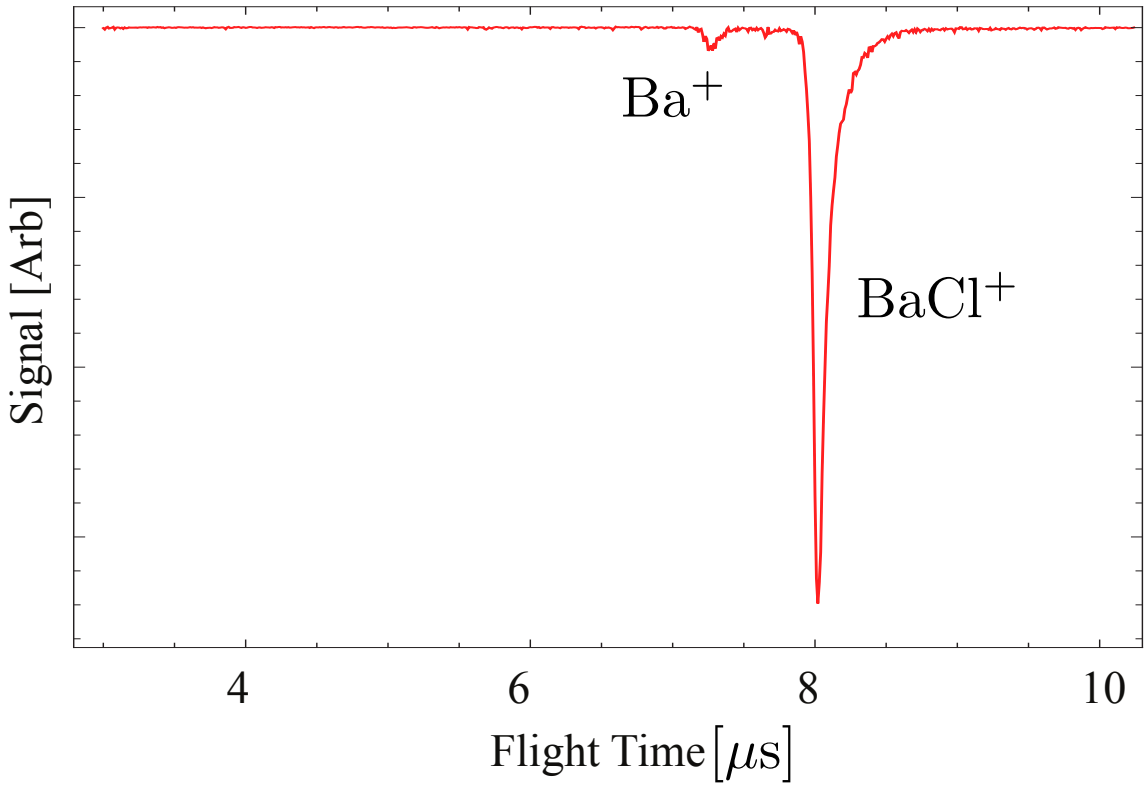

Figure 2.6: A sample trace from LQT-ToF [3]. The parent ion $BaCl^+$ and its photodissociation product Ba^+ are well-resolved.

2.2.2 Fluorescence Detection

A few atomic ions (*e.g.* Ba^+, Yb^+, Ca^+) with strong cycling transitions can be detected by their fluorescence. Because of the distinct optical wavelength associated with the excitation and emission, fluorescence identification of ions can be applied without complications usually present in channeltron-based detection, which for instance include isotopes ($^{137}Ba^+$ and $^{138}Ba^+$) or accidental interference ($^{173}Yb^+$ and $^{173}BaCl^+$).

The physical device to collect the fluorescence photon is a photon multiplier tube (PMT), usually coupled with sophisticated imaging system to maximize photon collection. A typical fluorescence image of trapped ion is shown in Fig. 2.7.

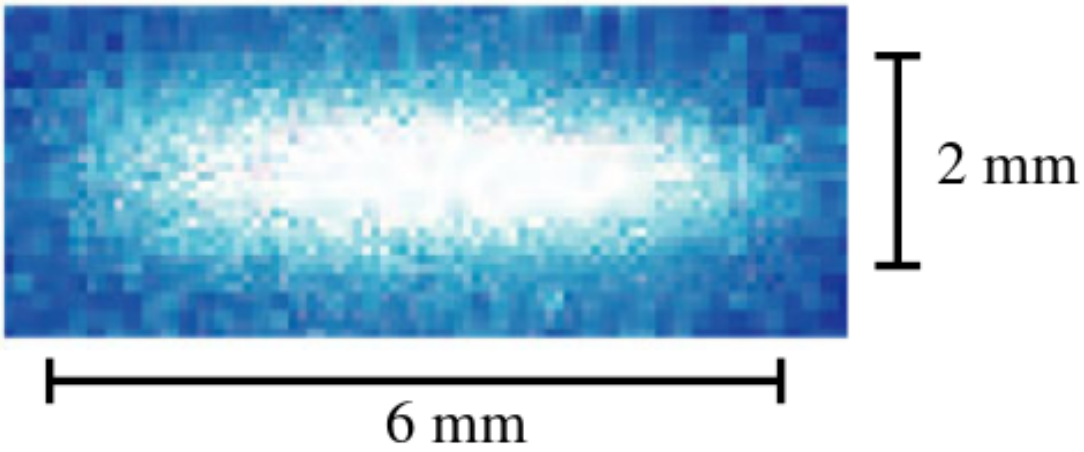

Figure 2.7: The fluorescence image (false color) of trapped $^{174}Yb^{+}$ ion cloud.

CHAPTER 3

Neutral gas sympathetic cooling of an ion in a Paul trap

3.1 Introduction

The fact that two isolated objects in thermal contact tend to the same temperature is the most basic tenet of thermodynamics. It is also the essence of the technique of sympathetic cooling, where a sample is prepared at a desired temperature by bringing it into thermal contact with a much larger body already at the desired temperature. It is difficult to overstate the importance of this technique as it underpins applications ranging from basic refrigeration to quantum information science.

It may be considered surprising then that a gas of ions trapped in a radio-frequency Paul trap and immersed in a reservoir of neutral atoms, does not equilibrate to the same temperature as the neutral atoms. Instead, the ions are found to have a higher temperature than the neutral gas, and in some cases are heated so much that they escape the trap. Since the early work of Dehmelt [5] it has been known that this apparent contradiction with the laws of thermodynamics is due to the fact that ions are subject to a time-dependent confining potential and are therefore not an isolated system. However, despite pioneering work by Dehmelt and others, an accurate analytical description of the relaxation process has not yet been achieved. Given the recent surge in interest in hybrid atom-ion systems [43, 52, 53, 54, 55, 9, 45, 56, 44, 57], where ions are immersed in baths of ultracold atoms, there is currently a strong need for such a description so that these systems can be understood and optimized.

Building upon the important result of Moriwaki [4], here we present a simple kinematic model, which accurately describes the ion relaxation process. This model, which has been verified by detailed molecular dynamics simulations, provides a simple and accurate means to calculate both the relaxation dynamics and the properties of the ion steady state. This model also provides significant physical intuition for the problem and as such suggests several ways for optimizing ongoing and planned experiments in fields as diverse as quantum chemistry [43, 52, 53, 54, 55, 45, 56, 44, 57, 66, 67], mass spectrometry [68], and quantum information [48].

In the remainder of this work, we first review the basics of ion trapping and introduce the time-averaged ion kinetic energy. We then consider the effect of a collision with a neutral particle on the evolution of the kinetic energy of a single ion in a Paul trap, and show that due to the presence of the time-dependent potential the collision center-of-mass frame energy is not conserved. Following this result, we develop a rate equation model, which accounts for the relaxation and exchange of the ion energy in all three dimensions. We then present simple formulae for the calculation of the ion temperature relaxation rate and steady-state value, as well as the dependency of these values on the ion trapping parameters and particle mass. We establish the validity of these results by comparing them to a detailed molecular dynamics simulation. We conclude with a qualitative explanation for the recent observation [6] of non-Maxwellian distribution functions for these systems.

3.2 Time-averaged kinetic energy

Before proceeding to the theory of energy relaxation, an ambiguity regarding the definition of ion's "energy" needs to be resolved first. Although collisions with neutral atoms pertains to ion's instantaneous velocity $\mathbf{v}$ and thus instantaneous energy $\frac{1}{2}m_i\mathbf{v}^2$, their values are constantly fluctuating (shown in Fig. 3.1), because energy coherently flows back and forth between the kinetic energy of the ion and the confining electric field at frequency Ω.

Therefore, it is useful to define the time-averaged kinetic energy

$$W_j = \frac{m}{2} \lim_{T\to\infty} \frac{1}{2T} \int_{-T}^{T} v_j^2 d\tau = \frac{m}{2} \overline{\dot{c}_j^2} (A_j^2 + B_j^2), \tag{3.1}$$

where the bar denotes the time average. W_j includes contributions from both the random thermal motion of the ion, i.e. the secular energy, and the micromotion. The ratio of the secular energy U_j to the total average kinetic energy is simply

$$\eta_j \equiv \frac{U_j}{W_j} = \frac{|C_0|^2}{\sum_{n=-\infty}^{\infty} |C_{2n}|^2}. \tag{3.2}$$

In the x and y directions, $\eta_{x,y} \approx \frac{1}{2}$ for $q < 0.4$ and the micromotion energy is given by $W_{mm,j} = W_j - U_j$. In the z direction where the trapping field is time-independent ($a, q \to 0$), $c_z(\tau)$ and $s_z(\tau)$ simply become the cosine and sine functions. Thus, all micromotion sidebands vanish and $\eta_z = 1$.

3.3 Modeling the collision process

When the ion trap is immersed in a buffer gas of neutral atoms, the Mathieu trajectory of the ion is modified by interactions with the neutral atoms. The ion-neutral interaction potential is comprised of a long-range attraction $V(r) = -C_4/2r^4$ and short-range repulsion, where C_4 is given by $C_4 = \alpha e^2/(4\pi\epsilon_0)^2$, and α is the polarizability of the neutral atom. Recent work [5], has explored effects of this potential at ultracold temperatures, showing that the perturbations of the ion trajectory by the C_4 potential can lead to heating of the ion. Here we do not consider this effect, but given that the characteristic length of the C_4 interaction [69] is small compared to the trap dimension we treat the collision as a point-like interaction. As will be seen, this approximation is justified, despite the important result of Ref. [70], as the effects considered here typically lead to temperatures that preclude the observation of the effects considered in Ref. [70]. We also make the additional simplifying assumptions that the density of the neutral atoms is constant and that inelastic processes, such as charge exchange, do not occur.

Because the motion of the ion differs significantly in the radial and axial directions of a linear Paul trap, the relaxation and redistribution of energy is significantly more complicated

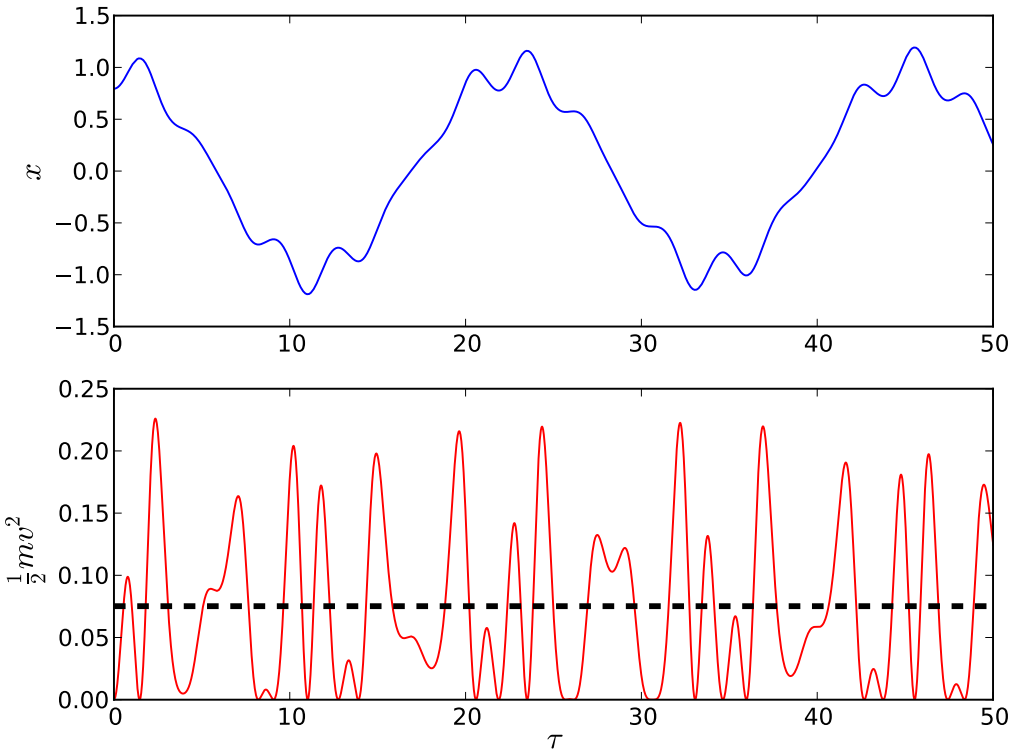

Figure 3.1: A sample of ion's trajectory in 1D (top panel) and instaneous energy for $m = 1$ (bottom panel, red line). The time-averaged energy W is shown in the black dashed line.

than in a time-independent harmonic trap [71]. We therefore describe the evolution of the average ion kinetic energy $\mathbf{W} = [W_x, W_y, W_z]^{\mathrm{T}}$ by a three-dimensional rate equation,

$$\frac{d\mathbf{W}(t)}{dt} = -\Gamma \mathbf{M}(\mathbf{W}(t) - \mathbf{W}_{st}) \tag{3.3}$$

where Γ is an average collision rate (which may depend on energy), $\mathbf{M}$ is a 3×3 "relaxation matrix" that accounts for energy damping and redistribution among the three trap directions, and $\mathbf{W}_{st}$ is the steady-state kinetic energy.

3.3.1 Collision cross-section

In order to calculate both Γ and $\mathbf{M}$, it is necessary to know the ion-neutral differential elastic scattering cross-section, which, given the spherical symmetry of the interaction potential, can

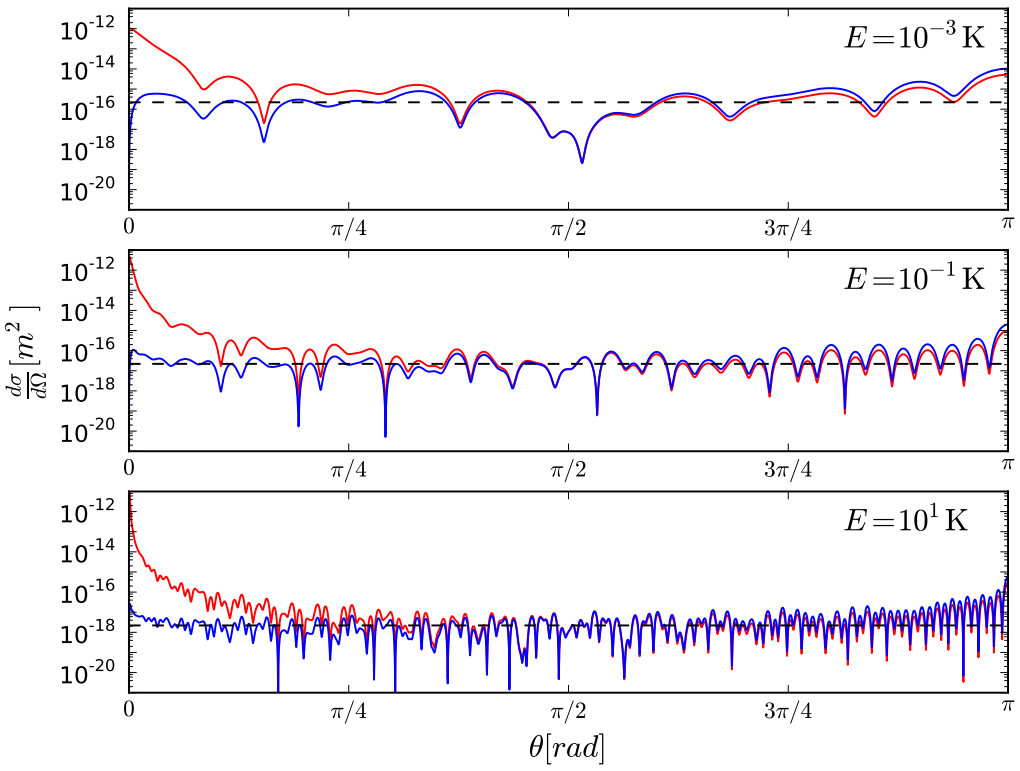

Figure 3.2: Comparison of the elastic (red solid line), diffusion (blue solid line) and isotropic Langevin cross-section (black dashed line) for three different collision energy for Yb^+ and Ca system.

be calculated from [72]

$$\frac{d\sigma_{el}}{d\Omega}(\theta, E) = \left| \sum_{\ell} (2\ell + 1) P_\ell(\cos\theta) \frac{e^{2\imath\eta_\ell} - 1}{2\imath k} \right|^2 \tag{3.4}$$

where E is the collision energy and η_ℓ is the phase shift of the ℓ-th partial wave induced by the interaction potential. For a specific ion-neutral combination, and thus for a specific interaction potential, it is straightforward to calculate this differential cross-section numerically [73]. For reference, we have calculated $\frac{d\sigma_{el}}{d\Omega}$ for the Yb^+ and Ca system as the necessary interaction potential was available to us [55]. The results are shown in Fig. 3.2 for three different collisional energies and expected to be similar for other atom-ion combinations [74].

As can be seen in Fig. 3.2 the differential cross-section exhibits a large forward scattering

peak at all energy scales. Thus, the majority of ion-neutral collisions lead to only slightly deflected trajectories, resulting in a very small change in $\mathbf{W}$. Therefore, as originally argued by Dalgarno and co-workers [75], to prevent an overestimate of the energy redistribution due to collisions the momentum transfer (diffusion) differential cross-section, i.e. $\frac{d\sigma_d}{d\Omega} = \frac{d\sigma_{el}}{d\Omega}(1 - \cos\theta)$, also shown in Fig. 3.2, should be used to calculate the total ion-neutral collision rate. Fortuitously, the diffusion differential cross-section is approximately isotropic in scattering angle, especially after thermal averaging, and agrees quite well with the simple Langevin cross-section [42] $\sigma_d \approx \sigma_L = \pi\sqrt{\frac{2C_4}{E}}$, as seen in Fig. 3.2. Therefore, we replace the cross-section by an isotropic profile which integrates to σ_L. Under this approximation, the collision rate $\Gamma = 2\pi\rho\sqrt{\frac{C_4}{\mu}}$ becomes energy independent and the calculation of $\mathbf{M}$ is greatly simplified. As demonstrated below, the validity of this approximation is confirmed by comparing the model to a detailed molecular dynamics simulation, which uses the full differential cross-section.

3.3.2 Relaxation matrix

With the collision rate in hand, the relaxation matrix $\mathbf{M}$ is calculated by considering the kinematics of a collision between an ion and neutral atom as follows. Suppose that at time τ_c an ion undergoes an elastic collision with an incoming neutral atom of mass m_n and velocity $\mathbf{v}_n$. Conservation of momentum and energy for the collision dictate that the velocity of the ion after the collision with neutral atom is given by the sum of center-of-mass velocity and the scattered relative velocity [76],

$$\mathbf{v}' = \frac{1}{1+\tilde{m}}\mathbf{v} + \frac{\tilde{m}}{1+\tilde{m}}\mathbf{v}_n + \frac{\tilde{m}}{1+\tilde{m}}\mathcal{R}(\mathbf{v} - \mathbf{v}_n) \tag{3.5}$$

where $\tilde{m} = \frac{m_n}{m_i}$ is the mass ratio and $\mathcal{R}$ is the collision rotation matrix, which following the above discussion is isotropic. Likewise, because the characteristic length of the C_4 interaction [69] is small compared to the trap dimension, the position of the ion is assumed to be unchanged during the collision, i.e. $\mathbf{r}' = \mathbf{r}$. By requiring that $\mathbf{r}'$ and $\mathbf{v}'$ also corresponds to a Mathieu solution through Eq. 2.6, a new set of oscillation amplitude $(\mathbf{a}', \mathbf{b}')$ and the energy after the collision $\mathbf{W}'$ can be found.

This last step is the critical difference between sympathetic cooling in a static and time-dependent trap, which is illustrated with the following one-dimensional example. In a static trap, like that in Ref. [77], if a collision happens at position $x = a$ that reduces the velocity such that $v'_x = 0$, the trapped particle with m begins a 'new' oscillation trajectory, described by a $x' = a\cos(2\pi\sqrt{k/m}\ t)$, where k is the trap spring constant. This collision always reduces the total energy of the particle. By contrast in the time-dependent potential of a linear Paul trap, because of the terms in Eq. 2.7 with $n \neq 0$, it is possible that even though the collision brings the particle to rest, the particle may have a *higher* energy after the collision. This can be seen by considering the time derivative of Eq. 2.7 as follows. Suppose the collision happened at a time when one of the $n \neq 0$ terms was maximal, which corresponds to a large micromotion velocity. If the collision brings the total velocity to zero, this can be accomplished by having a large (and opposite) contribution to the velocity from the $n = 0$ (secular) mode. Thus, even though the particle is momentarily stopped, it leaves the collision on a trajectory of higher amplitude.

With this prescription the calculation of $\mathbf{M}$ is straightforward. First we rewrite, Eq. 3.1 in terms of the instantaneous coordinates for x direction,

$$W_x = \frac{m\overline{\dot{c}_x^2}}{2w_{0,x}^2}\left((\dot{c}_x^2 + \dot{s}_x^2)x^2 + (c_x^2 + s_x^2)v_x^2 - 2(c_x\dot{c}_x + s_x\dot{s}_x)xv_x\right) \tag{3.6}$$

where $w_{0,x} = c_x\dot{s}_x - s_x\dot{c}_x$ is the Wronskian and constant in time [63]. The change in energy with a collision is then

$$\begin{aligned} W'_x - W_x &= -\frac{m\overline{\dot{c}_x^2}}{w_{0x}^2}\overline{(c_x\dot{c}_x + s_x\dot{s}_x)(x(\langle v'_x\rangle - v_x))} \\ &\quad + \frac{m\overline{\dot{c}_x^2}}{2w_{0x}^2}\overline{(c_x^2 + s_x^2)(\langle v'^2_x\rangle - v_x^2)} \\ &\equiv \Delta W_{x,1} + \Delta W_{x,2}. \end{aligned} \tag{3.7}$$

For $\Delta W_{x,1}$ because v_{nx} is a normally distributed random variable, and $\mathcal{R}$ is a random rotation matrix, both $\langle v_{nx}\rangle$ and $\langle\mathcal{R}(\mathbf{v} - \mathbf{v_n})_x\rangle$ vanish, so $\langle v'_x\rangle = \frac{1}{1+\tilde{m}}v_x$. Therefore, using Eq.

2.6 and 3.1 we obtain,

$$\begin{aligned}\Delta W_{x,1} &= \frac{\tilde{m}}{1+\tilde{m}}\frac{m\overline{\dot{c}_x^2}}{w_{0x}^2}\overline{(c_x\dot{c}_x + s_x\dot{s}_x)(xv_x)} \\ &= \frac{\tilde{m}}{1+\tilde{m}}\frac{\overline{(c_x\dot{c}_x + s_x\dot{s}_x)^2}}{w_{0,x}^2}\frac{m}{2}\overline{\dot{c}_x^2}(a_x^2+b_x^2) \\ &= \frac{\tilde{m}}{1+\tilde{m}}\epsilon_x W_x,\end{aligned} \tag{3.8}$$

where $\epsilon_x = \frac{\overline{(c_x\dot{c}_x+s_x\dot{s}_x)^2}}{w_{0,x}^2}$.

To evaluate $\Delta W_{x,2}$, we note that v_{nx}, $\mathcal{R}$ and v_x are uncorrelated, so $\langle v_x v_{nx}\rangle = \langle v_x \mathcal{R}(\mathbf{v}-\mathbf{v_n})_x\rangle = \langle v_{nx}\mathcal{R}(\mathbf{v}-\mathbf{v_n})_x\rangle = 0$. Furthermore, since $\mathcal{R}$ is random rotation, $\langle \mathcal{R}(\mathbf{v}-\mathbf{v_n})_x^2\rangle = \langle \frac{1}{3}(\mathbf{v}-\mathbf{v_n})^2\rangle$. Rearranging terms we obtain,

$$\langle v_x'^2\rangle - v_x^2 = \frac{\tilde{m}^2}{(1+\tilde{m})^2}\left(\left(-\frac{2}{3}-\frac{2}{\tilde{m}}\right)v_x^2 + \frac{1}{3}v_y^2 + \frac{1}{3}v_z^2 + 2\sigma_{v_n}^2\right) \tag{3.9}$$

where σ_{vn} is the thermal width of neutral atom velocity distribution. Thus, we find

$$\Delta W_{x,2} = \frac{\tilde{m}}{(1+\tilde{m})^2}\Big(\Big(-\frac{2\tilde{m}+2}{3}\Big)(1+\epsilon_x)W_x + \frac{\tilde{m}\alpha_x}{6}W_y + \frac{\tilde{m}\alpha_x}{6}W_z + \alpha_x W_n\Big) \tag{3.10}$$

where $\alpha_x = \frac{\overline{(c_x^2+s_x^2)}\cdot\overline{(\dot{c}_x^2+\dot{s}_x^2)}}{w_{0,x}^2}$, and $W_n = \frac{m_n}{2}mv^2$ is the average kinetic energy of the neutral atom.

Combining the results of $\Delta W_{x,1}$ and $\Delta W_{x,2}$, and the results for the y and z directions, finally we have

$$\begin{aligned}\mathbf{W}' - \mathbf{W} &= -\mathbf{M}\mathbf{W} + \mathbf{N} \\ &= -\mathbf{M}(\mathbf{W}-\mathbf{W}_{st})\end{aligned} \tag{3.11}$$

where

$$\mathbf{M} = \frac{\tilde{m}^2}{(1+\tilde{m})^2}\begin{bmatrix} \frac{2\epsilon-1}{3}-\frac{1}{\tilde{m}} & \frac{\alpha}{6} & \frac{\alpha}{6} \\ \frac{\alpha}{6} & \frac{2\epsilon-1}{3}-\frac{1}{\tilde{m}} & \frac{\alpha}{6} \\ \frac{1}{6} & \frac{1}{6} & -\frac{1}{3}-\frac{1}{\tilde{m}} \end{bmatrix} \tag{3.12}$$

and

$$\mathbf{N} = \frac{\tilde{m}}{(1+\tilde{m})^2}\begin{bmatrix} \alpha W_n \\ \alpha W_n \\ W_n \end{bmatrix} \tag{3.13}$$

And, the steady-state kinetic energy is given by,

$$\begin{aligned}\mathbf{W}_{st} &= -\mathbf{M}^{-1}\mathbf{N} \\ &= \left(\mathbf{I} - \tilde{m} \begin{bmatrix} \frac{2\epsilon-1}{3} & \frac{\alpha}{6} & \frac{\alpha}{6} \\ \frac{\alpha}{6} & \frac{2\epsilon-1}{3} & \frac{\alpha}{6} \\ \frac{1}{6} & \frac{1}{6} & -\frac{1}{3} \end{bmatrix} \right)^{-1} \begin{bmatrix} \alpha W_n \\ \alpha W_n \\ W_n \end{bmatrix}\end{aligned} \tag{3.14}$$

where $\alpha \equiv \alpha_x = \alpha_y$ and $\epsilon \equiv \epsilon_x = \epsilon_y$. Because in z direction the trapping field is time-independent, $\alpha_z = 1$ and $\epsilon_z = 0$. For $q < 0.4$, the numerical values of α and ϵ are approximated by [58],

$$\alpha \approx 2 + 2q^{2.24} \tag{3.15}$$

$$\epsilon \approx 1 + 2.4q^{2.4} \tag{3.16}$$

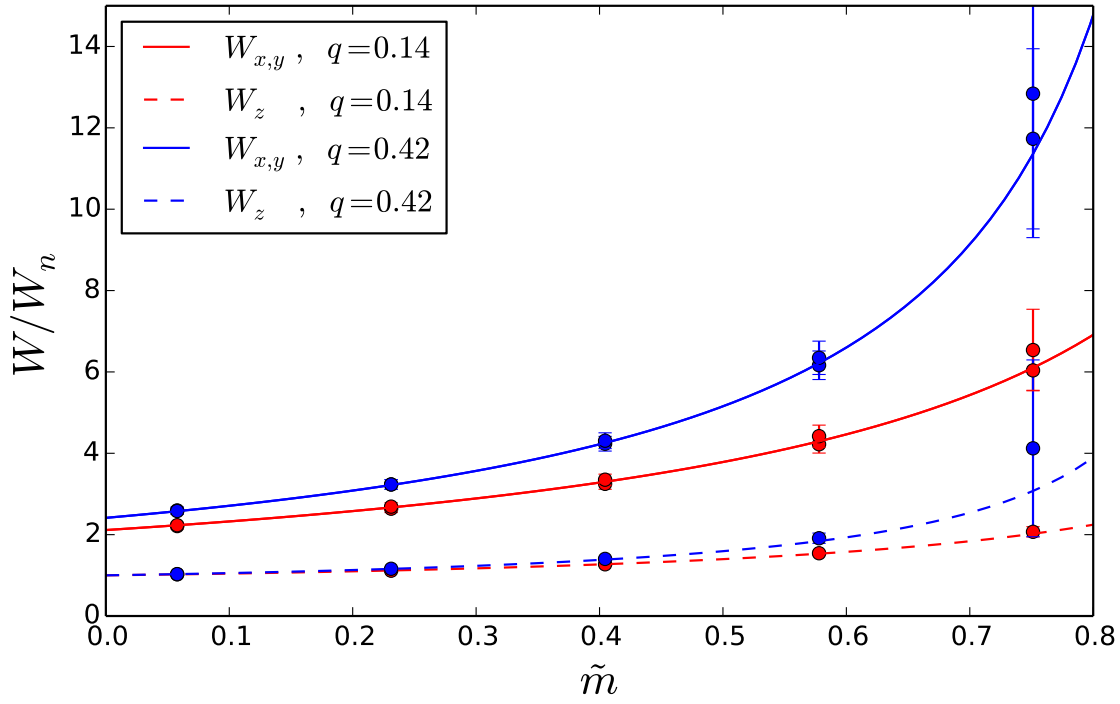

Figure 3.3: $\mathbf{W}_{st}$ as a function of mass ratio $\tilde{m}$ for $q = 0.14$ (red) and $q = 0.42$ (blue). The axial and radial component of $\mathbf{W}_{st}$ are denoted by dashed and solid lines (theory) and dots (simulation).

3.4 Model results

Simply put, the main difference between sympathetic cooling in a linear Paul trap and traditional buffer-gas cooling [71] is that, because the trapping potential is time-dependent, a collision with a neutral atom can lead to heating of the trapped ion, regardless of the atom energy. This, perhaps surprising, effect depends on $\tilde{m}$ and q, and can best be seen in the steady-state energy and the asymptotic sympathetic cooling rate.

3.4.1 Steady-state energy

First shown in Fig. 3.3 are the three components of $\mathbf{W}_{st}$ normalized by W_n obtained from Eq. 3.14. Also, shown in this figure are the results of a detailed molecule dynamics simulation, described in the Appendix B. In the case of a light neutral atom $\tilde{m} \approx 0$ and low rf-drive $q = 0$, $\alpha \approx 2$ from Eq. 3.15, $\mathbf{W}_{st} \approx [2W_n, 2W_n, W_n]^{\mathrm{T}}$ from Eq. 3.14. As discussed earlier, this means that at steady state,

$$U_x = U_y = U_z = W_{mm,x} = W_{mm,y} = W_n \tag{3.17}$$

a result often referred to as the "equipartition" [78] of kinetic energy between secular motion and micro-motion in each direction. As $\tilde{m}$ increases, the steady-state secular energy deviates from equipartition and also become much higher than W_n. For high q values, this deviation become more significant. The analytical steady-state energy are given by

$$\begin{aligned} \frac{W_{x,y}}{W_n} &= \frac{9(2+\tilde{m})\alpha}{18 - 3\tilde{m}(\alpha + 4\epsilon - 4) - 2\tilde{m}^2(\alpha + 2\epsilon - 1)} \\ \frac{W_z}{W_n} &= \frac{3(6 + \tilde{m}(2 + \alpha - 4\epsilon))}{18 - 3\tilde{m}(\alpha + 4\epsilon - 4) - 2\tilde{m}^2(\alpha + 2\epsilon - 1)} \end{aligned} \tag{3.18}$$

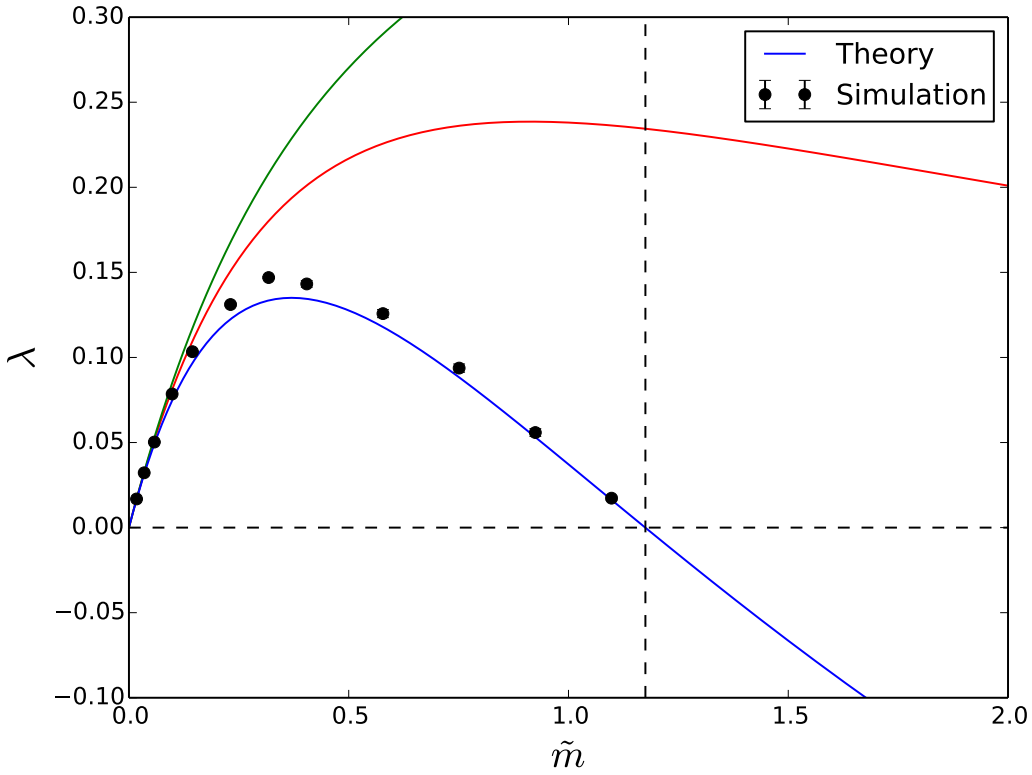

Figure 3.4: Eigenvalues of $\mathbf{M}$ as a function of $\tilde{m}$ for fixed $q = 0.14$ and $a = 0$. Black dots are asymptotic relaxation rates (normalized by Γ) from numerical simulations. Lines are three calculated eigenvalues of $\mathbf{M}$. The smallest one (blue line) intersects $\lambda = 0$ line at $\tilde{m} = \tilde{m}_c$, which separates cooling from heating.

3.4.2 Energy relaxation rate

By multiplying the diagonalizing matrix $\mathbf{P}$ of matrix $\mathbf{M}$ to Eq. 3.3 and defining $\mathbf{W}' \equiv \mathbf{PW}, \mathbf{W'}_{st} \equiv \mathbf{PW}_{st}$ and $\mathbf{M}' \equiv \mathbf{PMP^{-1}}$, we have

$$\begin{aligned} \frac{d\mathbf{PW}(t)}{dt} &= -\Gamma(\mathbf{PMP}^{-1})(\mathbf{P}(\mathbf{W}(t) - \mathbf{W}_{st})) \\ \Rightarrow \frac{d\mathbf{W}'(t)}{dt} &= -\Gamma\mathbf{M}'(\mathbf{W}'(t) - \mathbf{W'}_{st}) \end{aligned} \tag{3.19}$$

The solution to Eq. 3.3 is thus linear combination of three fundamental relaxation processes, whose rates are determined by the three eigenvalues of $\mathbf{M}$. The asymptotic behavior of the energy evolution is governed by the slowest relaxation rate, which is proportional to λ, the

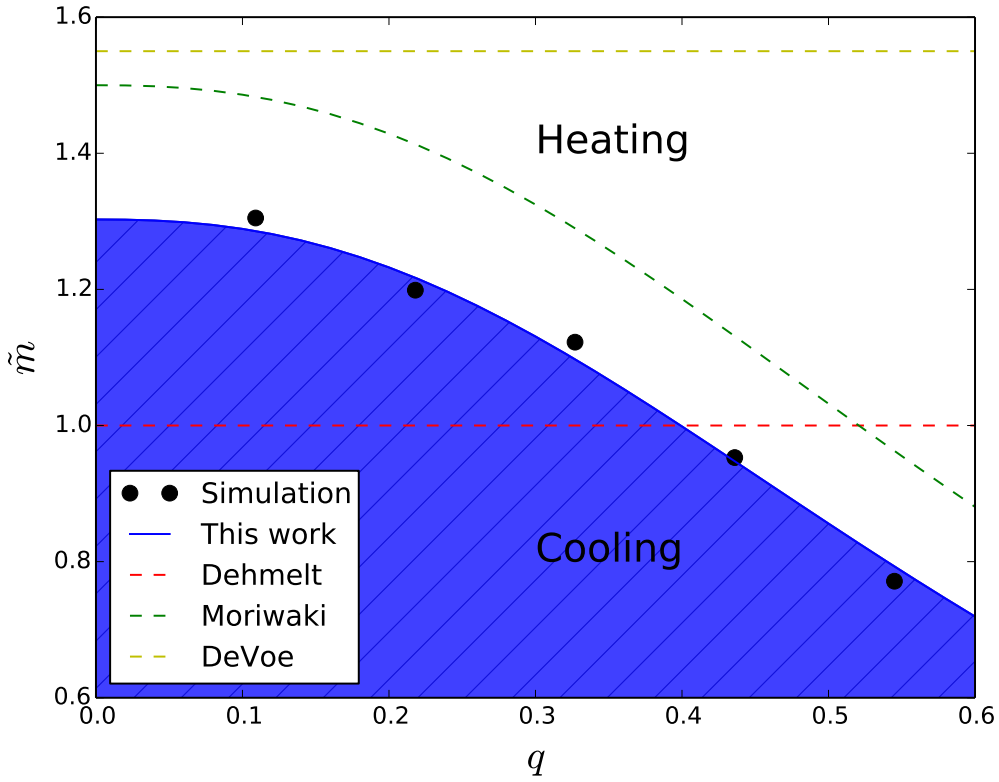

Figure 3.5: Simulated (dots) and calculated (blue line) critical mass ratio $\tilde{m}_c$ as a function of trap q parameter, as compared to previous results in Ref. [4, 5, 6].

smallest eigenvalue of $\mathbf{M}$, and given by

$$\lambda = \frac{\tilde{m}}{(1+\tilde{m})^2}\left(1 - \frac{\tilde{m}}{\tilde{m}_c}\right) \tag{3.20}$$

where $\tilde{m}_c$ is the critical mass ratio given in terms of trap parameters,

$$\tilde{m}_c = \frac{3(4 - \alpha - 4\epsilon + \sqrt{\alpha^2 + 8\alpha(1+\epsilon) + 16\epsilon^2})}{4(-1 + \alpha + 2\epsilon)} \tag{3.21}$$

Shown in Fig. 3.4 is the relaxation rate given by Eq. 3.20, compared to numerical fit to asymptotic energy from simulation. For $\tilde{m} \ll \tilde{m}_c$, the cooling rate from Eq. 3.20 is similar to the traditional sympathetic cooling result up to a numerical factor [71]. In this regime, the initial positive slope of λ indicates an enhancement of energy transfer efficiency through collisions with neutral atoms of similar mass. However, the additional factor $1 - \frac{\tilde{m}}{\tilde{m}_c}$ soon causes λ to reach a maximum and decrease to negative values once $\tilde{m}$ exceeds $\tilde{m}_c$. At

this point, it is observed in the simulation that oscillation amplitude of the ion grows with collisions, until the ion become too energetic to be trapped.

The critical mass ratio $\tilde{m}_c$ depends on the trapping q parameter. Shown in Fig. 3.5, the analytical result from Eq. 3.21 are calculated for a range of q values, shows the cooling-heating boundary moves toward smaller $\tilde{m}$ and matches accurately with simulation results. This is a major improvement over previous results from various crude models in Ref. [5, 4, 6].

3.5 Ion's energy distribution - power-law tails

The peculiarity of sympathetic cooling in ion trap is also manifested in ion's steady-state energy distribution, which features a heavy power-law tail [6] instead of Maxwell-Boltzmann, due to the random amplifications of ion's energy caused by collision. To gain a quantitative understanding, consider a simplified one-dimensional model, in which ion and neutral atom's motion are restricted in one dimension, and $\mathcal{R} = -1$ in Eq. 3.5. In (A, B) space, ion undergoes random jumps followed by

$$\begin{bmatrix} A_{N+1} \\ B_{N+1} \end{bmatrix} = \left(\mathbf{I} + \frac{\zeta}{w_0} \begin{bmatrix} s\dot{c} & s\dot{s} \\ -c\dot{c} & c\dot{s} \end{bmatrix}_{\tau_N} \right) \begin{bmatrix} A_N \\ B_N \end{bmatrix} + \frac{\zeta v_n}{w_0} \begin{bmatrix} s \\ c \end{bmatrix}_{\tau_N} \tag{3.22}$$

where $\zeta = \frac{2\tilde{m}}{1+\tilde{m}}$, $[A_{N+1}, B_{N+1}]^{\mathrm{T}}$ are the coordinates after N-th collision which occurs at $\tau = \tau_N$. τ_N $(N = 1, 2, \cdots, \infty)$ constitute an array of Poisson variables, with average interval equal to Γ^{-1}. A recurrence relation for W_N can be derived from Eq. 3.1, given by,

$$W_{N+1} = C\ W_N + D\ W_N^{\frac{1}{2}} W_n^{\frac{1}{2}} + E\ W_n \tag{3.23}$$

If distribution of high energy ions i.e. $W_N \gg W_n$ are considered, then only the term linear in W_N is kept, changing Eq. 3.23 into

$$W_{N+1} = C W_N \tag{3.24}$$

The full mathematical expression of the multiplicative coefficient C is given by,

$$\begin{aligned} C(\tau_N, \theta_N) = &\cos^2\theta_N \left(\left(1 + \zeta \frac{s\dot{c}}{w_0}\right)^2 + \zeta^2 \frac{c^2\dot{c}^2}{w_0^2} \right)_{\tau_N} \\ &+ \sin^2\theta_N \left(\left(1 - \zeta \frac{c\dot{s}}{w_0}\right)^2 + \zeta^2 \frac{s^2\dot{s}^2}{w_0^2} \right)_{\tau_N} \\ &+ 2\sin\theta_N \cos\theta_N \left(\zeta \frac{s\dot{s} - c\dot{c}}{w_0} + \zeta^2 \frac{\dot{c}\dot{s}(c^2 + s^2)}{w_0^2} \right)_{\tau_N} \end{aligned} \tag{3.25}$$

where θ_N is the polar angle given by $\theta_N = \arctan(B_N/A_N)$. Because W only depends on $A^2 + B^2$, it is expected that as $N \to \infty$, θ_N becomes uniformly distributed in the range of $[0, 2\pi]$ and uncorrelated with τ_N. $Q(C)$, the probability density of C, are calculated from Eq. 3.25 for fix q and $\tilde{m}$ values and exhibits random amplifications shown in Fig. 3.6 panel (a) and (c).

Due to this random amplification, W develops a power-law tail $P(W) \propto W^{-(\nu+1)}$ at steady state [79]. Self-consistency condition requires that $P(W_{N+1})$, the probability density of W_N, is equal to the product of $P(W_N)$ and $Q(C)$, under the constraint Eq. 3.24, namely,

$$\begin{aligned} P(W_{N+1}) &= \iint Q(C)P(W_N)\delta(W_{N+1} - CW_N)\, \mathrm{d}C\, \mathrm{d}W_N \\ &= \int Q(C)P\left(\frac{W_{N+1}}{C}\right)\frac{1}{C}\mathrm{d}C \end{aligned} \tag{3.26}$$

If $P(W) \propto W^{-(\nu+1)}$ is plugged in, then ν is found to satisfy

$$\langle C^\nu \rangle = 1 \tag{3.27}$$

This energy distribution have been verified numerically, by subjecting the ion to 10^6 simulations, in each of which the ion undergoes 10^4 collisions, for each $\tilde{m}$ and q parameter. The statistics of ion's energy W is presented in Fig. 3.6, panel (b) and (d), showing full agreement with the numerical calculation given by Eq. 3.27. As $\tilde{m}$ and q increases random amplifications become more frequent, causing the energy distribution to deviate more from Maxwell-Boltzmann and become flatter.

In sharp contrast, a particle confined in a static potential $V(x) = \frac{m}{2}\omega^2 x^2$ and in contact with a reservoir at temperature T would have the same thermal distribution, regardless of

the reservoir particle's mass m_n, or the trapping frequency ω. This is because for static traps Mathieu functions $c(\tau)$ and $s(\tau)$ are replaced by $\cos(\omega\tau)$ and $\sin(\omega\tau)$, which simplifies Eq. 3.25 into

$$C = 1 - (2 - \zeta)\zeta \sin^2(\omega\tau - \theta) \tag{3.28}$$

Since $0 \leq \zeta \leq 1$, $C \leq 1$. Thus the energy of such system is never amplified. From a mathematical perspective, the solution for Eq. 3.27 is $\nu \to \infty$, meaning the predicted energy distribution falls faster than any power-law tail of finite ν, consistent with the thermal distribution $\exp(-E/k_BT)$.

To extend the above discussion to a full three-dimensional model, C necessarily become 3×3 stochastic matrices, and theory of stochastic matrix products [80] needs to be considered.

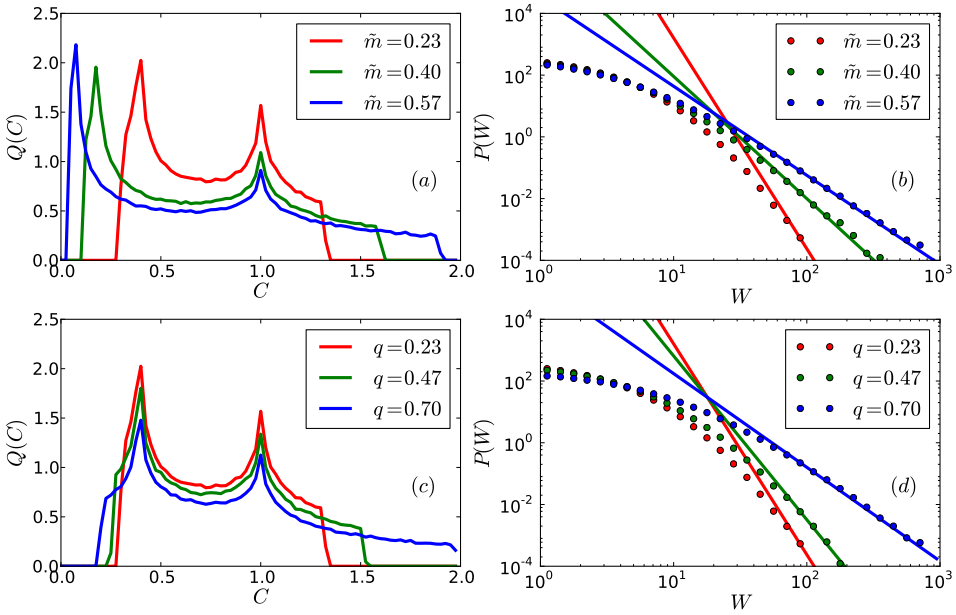

Figure 3.6: Probability density of the multiplicative noise $Q(C)$ and corresponding ion's energy $P(W)$ for 1-D model from simulations for fixed $q = 0.23$ (lines in panel a and b), and fixed $\tilde{m} = 0.23$ (dots in panel c and d). The tail of $P(W)$ is fitted to the power-law form of $W^{-(\nu+1)}$ (solid line in panel c and d), where ν is given by Eq. 3.27.

3.6 Conclusion

In summary, we have developed an analytical theory for the kinetic energy of a single ion in contact with ultracold atoms, based on the approximation of isotropic collision cross-section. The calculation of ion's steady-state energy from our model quantifies the deviation of equipartition of ion's energy. The transition from cooling to heating, and its dependence on trap parameter and mass ratio are also demonstrated, yielding improvements over previous models. With a 1D model, we have shown that ion's nonthermal energy distribution could be attributed to the random amplifications in the ion trap. These results could be critical for the design and interpretation of future experiments [39].

CHAPTER 4

Measurement of the Coulomb Logarithm in a Radio-Frequency Paul Trap

4.1 Introduction

Binary collisions in an ensemble of charged particles are fundamental throughout physics. As such, modeling their behavior plays an important role in applications ranging from thermonuclear fusion [81], to quantum computation [82]. Despite their importance and the large amount of work towards understanding their effects, there is still considerable ambiguity in how to best model these collisions. Since Landau's early work [83], the most straightforward approach handles the divergence associated with collisions of charged particles by introducing both a short-range and long-range cut-off for the $1/r$ interaction potential. The long-range cut-off is typically associated with the Debye screening length, $\lambda_D = \sqrt{\epsilon_o k_B T/\rho e^2}$, where ρ and T are density and temperature respectively. The short-range cut-off is associated with the Landau length, $R_C = e^2/(4\pi\epsilon_o k_B T)$, which is the distance of closest approach. Taken together, the integration bounds give rise to the so-called Coulomb logarithm in its simplest form, $\ln\Lambda = \ln(C\lambda_D/R_C)$, where C is a constant coefficient.

Over the last 75 years, there have been many attempts to calculate an accurate form of $\ln\Lambda$, ranging from straightforward estimations of the coefficient C [84] to sophisticated analytical treatments [85] with reasonable consensus that $C \approx 0.765$ [8]. These results give satisfactory agreement with data for weakly coupled systems, $g = R_C/\lambda_D \ll 1$, but clearly fail to describe strongly-coupled systems, $g \gg 1$, where the collision rate saturates. In this regime, more sophisticated treatments [86], which do not require a short-range cut-off, have recommended several alternative forms for $\ln\Lambda$. And recently, a new approach, motivated by

the need to model thermonuclear ignition, used molecular dynamics simulations to suggest $\ln\Lambda \sim \ln(1 + 0.7/g)$ [7, 87] for $g < 10$.

Given the importance of the Coulomb logarithm, there have also been attempts at a direct measurement of its dependence on the strong-coupling parameter g. These experiment, which have either been confined to the weak-coupling limit[88] or were inconclusive [89], were typically performed in dense, high-energy plasmas produced via laser ablation. In this work, we use an alternate route to realize a strongly-coupled ion system and measure $\ln\Lambda$: laser-cooled $^{174}Yb^{+}$ ions confined in a linear Paul trap. Here, the confining trap potential provides a smoothly varying, neutralizing background for the positively charged ions, resulting in a system described as a one-component plasma. Despite the low density, the low temperature accessible through laser cooling make it possible to realize systems with $g \gg 1$. Further, by laser cooling the sample to a large g and then allowing the ions to heat through micromotion interruption, we are able to measure the evolution of both the temperature and structural phase of the trapped ion cloud over a large range in g. From these measurements, we are then able to determine $\ln\Lambda$ for $10^{-7} \leq g \leq 10^{-2}$. Using a molecular dynamics simulation, we confirm this experimental determination and extend it to $10^{-7} \leq g \leq 10^{3}$. As the values of $\ln\Lambda$ for large g are known to be process dependent [90], this result must be carefully interpreted before it can be applied to other systems. Nonetheless, it offers a complete description of $\ln\Lambda$ for Paul traps, and thus allows a simple analytical description of trapped ion thermodynamics.

In the remainder of this chapter, we review the concept of Coulomb Logarithm and Chandreshakar-Spitzer formula, explain the phenomenon of ion heating by micromotion interruption, detail the method by which $\ln\Lambda$ is extracted, and describe the experimental system. We present experimental and molecular dynamics results and a recommended expression for $\ln\Lambda$ in linear Paul traps. We conclude with a discussion of the implications of this work for trapped-ion quantum information efforts.

4.2 Theoretical background

In a linear Paul trap, a singly charged ion experiences both a time-dependent force from the confining electric potential of the trap and Coulomb repulsion from the other ions, resulting in trajectories given by:

$$m\frac{d^2\mathbf{r}_i}{dt^2} = -e\nabla\phi(\mathbf{r}_i, t) + \sum_{i\neq j}^{N} \frac{e^2}{4\pi\epsilon_o}\frac{\mathbf{r}_i - \mathbf{r}_j}{|\mathbf{r}_i - \mathbf{r}_j|^3}, \tag{4.1}$$

with the trap potential given by Chapter 1. Due to the infinite range of the Coulomb interaction, Eq. (4.1) represents a complicated many-body problem and has no closed-form solution. Therefore, two alternative approaches are usually employed to treat this system.

First, rigorous molecular dynamics (MD) simulations have been performed to study the structure of ion clouds [91] and rf heating rates [92], and for comparison with experimental ion fluorescence images [93]. Despite their successes, these simulations offer little physical intuition, making it difficult to optimize a given system.

The second approach to modeling large ion systems in a Paul trap has been through analytical techniques [94, 95, 78, 4]. Of these, the simplest and most intuitive describes the trapped ion trajectories by the well-known Mathieu solutions and includes the effect of the Coulomb interaction as hard-sphere collisions between ions to calculate, among other things, the evolution of the trapped ion kinetic energy [78, 4]. In this limit, the collision-induced heating rate is given as, $\dot{W} = \gamma\Delta W$, where γ is the collision rate and ΔW is the kinetic energy change per collision [4], which is found by enforcing conservation of momentum and energy for the collision and requiring that the new ion trajectory corresponds to a Mathieu solution. In contrast to static traps, ΔW does not average to zero over time, or over the ensemble, in a rf Paul trap. In fact, as shown in Ref. [4] upon averaging ΔW is always positive, leading to the so-called micromotion-interruption heating phenomenon. Though this heating has been explained in different ways [96, 5, 94], it arises from the simple fact that when ions undergo collisions their trajectories are not given by the stable Mathieu trajectories and as a result the rf trapping field can do net work on them.

To link temperature with W, we introduce T_{sec} and T_{tot} to be proportional to the random thermal energy (secular motion) of the ions and the total kinetic energy (secular motion plus micromotion), respectively [5]:

$$CT_{tot} = W \qquad\qquad CT_{sec} = W_{sec} = \eta(W - W_{ex}) \tag{4.2}$$

where $C = \frac{3}{2}Nk_B$ and η is the ratio of secular energy to total energy – $\eta \approx \frac{3}{5}$ for low Mathieu q parameter as a consequence of equi-partition of energy between secular motion and micromotion [78]. W_{ex} accounts for the excess micromotion energy [97] due to displacement of the ion from the node of the oscillating electric field, as a result of either the location of the ion in the crystal or stray, uncompensated, dc electric fields. Typically, $T_{ex} = W_{ex}/C$ is a few Kelvin for an ion crystal composed of $N \sim 10^3$ ions [97, 93].

Using the Chandrasekhar-Spitzer plasma self-collision rate [84] (also see Eq. B.4 in Appendix for detail), the rate of change of the secular temperature of the ion cloud is given as:

$$\dot{T}_{sec} = \frac{e^4 \rho_i(T_{sec}) \ln\Lambda}{2\pi\epsilon_0^2\sqrt{m}(3k_B T_{sec})^{3/2}}\bar{\epsilon}(T_{sec} + \eta T_{ex}) \tag{4.3}$$

where $\rho_i(T_{sec})$ is the ion density [4] and $\bar{\epsilon} = \Delta W/W$ is the average fractional increase of the ion energy per collision. By averaging over the rf-phase at which the collision takes place, Refs. [78, 4] have calculated $\bar{\epsilon}$ in terms of the Mathieu stability parameters a and q. Through numerical integration of their result, we have found $\bar{\epsilon}$ can be simplified to $\bar{\epsilon} \approx \frac{2}{3}(1 + 2q^{2.24})$ with a relative error $< 0.4\%$ for $q \leq 0.4$, $a = 0$. Thus, by laser cooling a sample of trapped ions to a low initial temperature, extinguishing the laser cooling, and monitoring the ion temperature evolution, we are able to measure $\ln\Lambda$ as a function of g.

4.3 Experiment setup

The experimental apparatus used in this work consists of a sample of $^{174}Yb^+$ ions, loaded via laser ablation, into a linear rf Paul trap with $r_o = 1.2$ cm, $z_o = 1.075$ cm, $\alpha = 0.13$, $\Omega = 2\pi \times 300$ kHz, $V_{rf} = 155$ V and $V_{ec} = 5$ V. A strongly coupled ion ensemble ($N = 10^{2-3}$) is realized by laser-cooling the Yb^+ ions, along the trap axis, with a 369 nm cooling laser

(detuned from resonance by $\delta = -30$ MHz) and 935 nm repump laser ($\delta = 0$ MHz) to a starting secular temperature, measured from the Doppler broadened fluorescence profile, ranging from Doppler limited, $T_D \sim 1$ mK to 100 mK, depending on crystal size, resulting in a one-component plasma with $g = 10^2 \sim 10^3$.

Once the strongly-coupled plasma is established in the trap, the cooling laser is extinguished and the ions evolve in the trap and heat through micromotion interruption. After a variable time delay, the cooling and repump lasers are reapplied and the fluorescence level of the ion cloud immediately recorded. If the ion temperature has increased during the time when the lasers were extinguished, this fluorescence level will be different than the steady-state value reached for the initially cold plasma, see Fig. 4.1(a). By recording the ratio of fluorescence before and after heating, the temperature of the ions can be estimated (see Appendix B) as a function of heating time in a manner similar to Ref. [98], as shown in Fig. 4.1(b)-(c) for a sample of ions with $N = 280$, with the uncertainties of estimation indicated by the representative error bars in Fig 4.1 and 4.2 (for estimation of uncertainty, see Supplementary Material). Typically, the observed fluorescence ratio decreases with increasing temperature since both the fluorescence profile is further Doppler broadened and the higher energy ion trajectories have less overlap with the laser beam inducing the fluorescence, see Fig. 4.1(a)-(b).

As seen in Figs. 4.1(b)-(c), the fluorescence level, and thus the temperature, is relatively unchanged until 10-100 ms after the laser cooing is extinguished, when a sharp increase in temperature occurs, followed by a region of slower heating. As detailed below, the relatively small heating rate observed at early times is a consequence of the suppression of ion-ion collisions, i.e. a small $\ln \Lambda$, for a strongly-correlated plasma, while the sudden jump in temperature coincides with the phase transition from the liquid to gas phase. At the liquid-gas boundary, the ion density is still relatively high, but the ion motion becomes less correlated, i.e. increased $\ln \Lambda$, leading to a larger heating rate. As the ions move into the gas phase, the motion becomes even more uncorrelated, leading to a further increase in $\ln \Lambda$, however, the density, and thus the collision rate drops, leading to a reduced heating rate. Also shown in Figs. 4.1(b)-(c) are the results of a molecular dynamics simulation, which initializes the ions

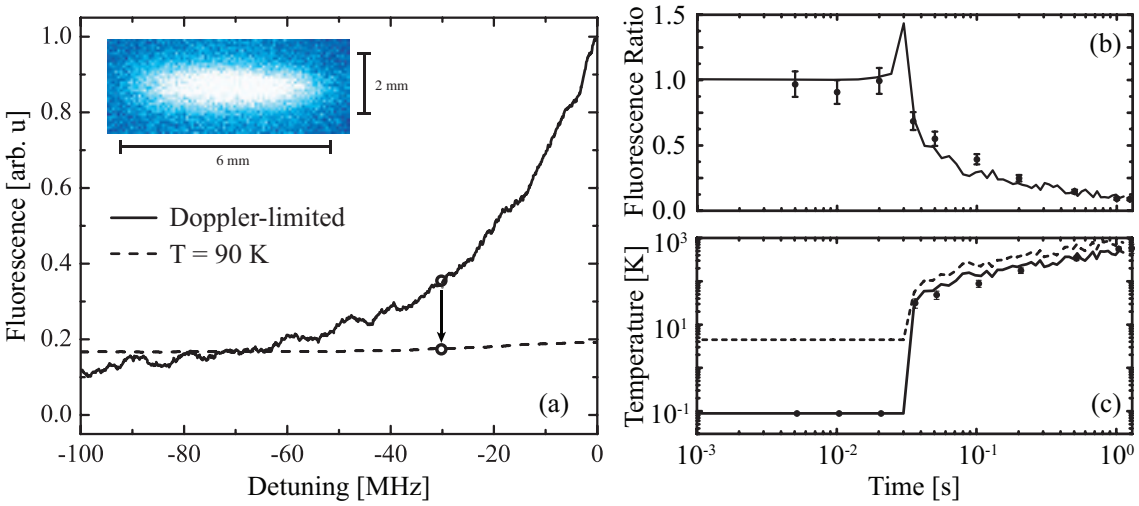

Figure 4.1: (a) Laser fluorescence profile for a sample of ions at the T_D (solid) and at ∼90 K (dashed). The arrow denotes the change in fluorescence at a fixed detuning of δ = -30 MHz. Also shown at the corner is a typical fluorescence image of ion cloud. (b) The observed (dots) and simulated (line) fluorescence ratio for δ = -30 MHz vs. heating time. The inset is a typical fluorescence image of an ion cloud. (c) The extracted (dots) and simulated T_{sec} (line) and T_{tot} vs. heating time.

at the experimentally realized temperature and then integrates Eq. (4.1) numerically using a leapfrog algorithm [99] implemented in ProtoMol software [100]. As the ions heat through micromotion interruption, their fluorescence level is calculated from the known laser intensity profiles and a rate-equation model, which includes the variation of laser intensity and Doppler shift for each ion position and velocity, respectively. Given experimental imperfections, such as stray fields, machining errors, laser amplitude and frequency noise, etc., that are not included in the simulation, the agreement between the simulated and measured fluorescence ratios (Fig. 4.1(b)) is satisfactory. In what follows, we use these results to extract the ion-ion heating rate and ultimately $\ln \Lambda$.

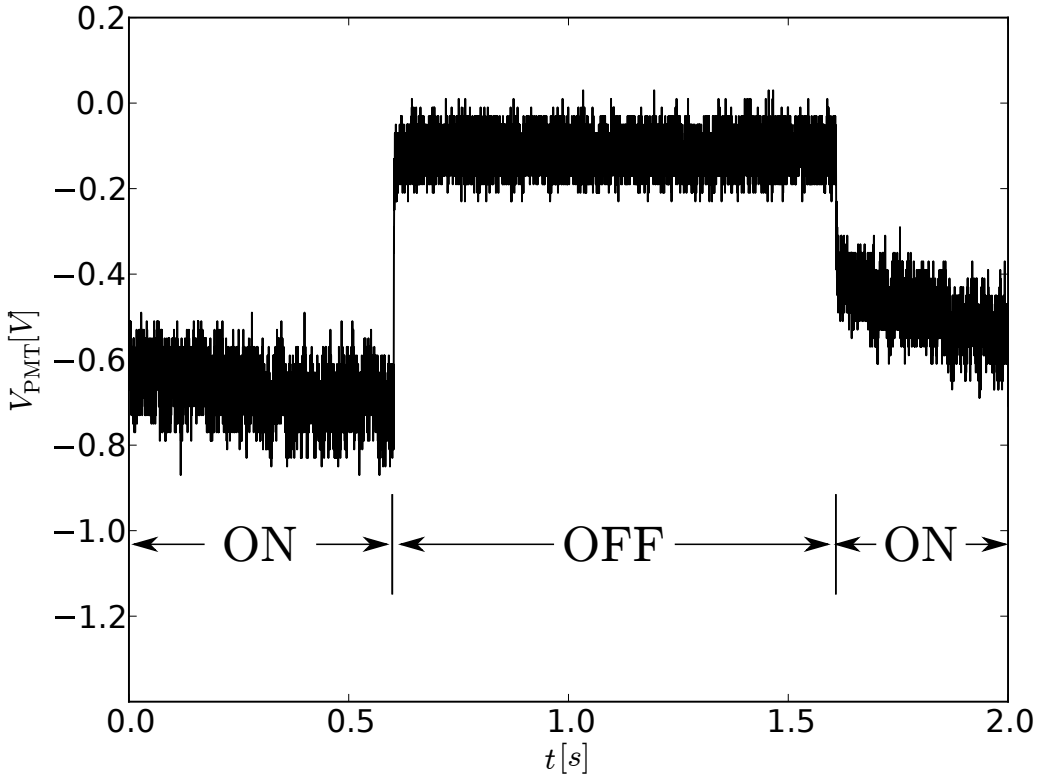

Figure 4.2: A sample trace of ion's fluorescence signal, with the status of the cooling laser denoted below the trace.

4.4 Experiment and simulation results of $\ln\Lambda$

Using experimental data like that shown in Fig. 4.1 for ion clouds with N between 300 and 3000, and modeling the density under the assumption of harmonic potential and thermal equilibrium as

$$\rho_i(T_{sec}) = \begin{cases} \rho_{max} & : T_{sec} \leq T_p \\ \rho_{max}\left(\frac{T_p}{T_{sec}}\right)^{3/2} & : T_{sec} \geq T_p \end{cases} \tag{4.4}$$

where $\rho_{max} = 4\epsilon_0 V_{rf}^2/mr_o^4\Omega^2$, $T_p = \frac{m\overline{\omega}^2}{2k_B}\left[\frac{3N}{4\pi}\frac{mr_o^4\Omega^2}{\epsilon_o V_{rf}^2}\right]^{2/3}$, and $\overline{\omega}$ is the geometric mean of the three secular frequencies, Eq. 4.3 is inverted to find $\ln\Lambda$ and the results are plotted in Fig. 2. As the heating rate is the time derivative of T_{sec}, the coarse granularity of the experimental data in time makes it difficult to calculate reliable values of $\ln\Lambda$ at short time scales. There-

fore, we also determine the heating rate and $\ln\Lambda$ from molecular dynamics simulations. For the simulated data, the heating rate is found by taking the numerical time derivative of the ion temperature, defined by $\frac{3}{2}Nk_BT_{tot} = \frac{m}{2}\sum_{i=1}^{N}\overline{\mathbf{v}_i(t)^2}$ and $\frac{3}{2}Nk_BT_{sec} = \frac{m}{2}\sum_{i=1}^{N}\overline{\mathbf{v}_{sec,i}(t)^2}$ where $\mathbf{v}_i$ and $\mathbf{v}_{sec,i}$ are the total and secular velocity of i^{th} ion and the overline denotes averaging over several secular motion periods. The resulting values for $\ln\Lambda$ are consistent with those extracted from experimental data, as shown in Fig. 4.3, but are expected to be of higher accuracy. Using this technique, molecular dynamics simulations were performed, like those shown in Fig. 4.1, for a range of ion numbers $N = \{50, 100, 500, 900\}$ and ion-cloud radial-to-axial ratios [101] of $R/z = \{0.25, 1, 4\}$) to determine if the parameterization of Eq. 4.3 leads to a universal form for $\ln\Lambda$ in Paul traps.

The values of $\ln\Lambda$ extracted from the simulation are plotted versus g in Fig. 4.3 alongside the Landau-Spitzer result [8] and the result of Ref. [7]. Also shown, as the top x-axis in this figure, is the corresponding plasma coupling parameter $\Gamma = e^2/\left(4\pi\epsilon_o a_{ws} k_B T_{sec}\right)$, which, given the Wigner-Seitz radius $a_{ws} = \sqrt[3]{3/(4\pi\rho_i)}$ and T_{sec}, characterizes the structural phase of the ion cloud as denoted by the three regions of the graph [102]. Clearly, despite the large changes in ion number and ion-cloud geometry, the dependence of $\ln\Lambda$ on g appears universal and can be parametrized by the piece-wise fit:

$$\ln\Lambda = \begin{cases} f_{\mathrm{I}}(g) = \frac{\ln(1+0.7/g)}{1+125\sqrt{g}} & : g < 1 \\ f_{\mathrm{II}}(g) = \frac{f_{\mathrm{I}}(g=1)}{g^2} & : g \geq 1 \end{cases} \tag{4.5}$$

where the form of $f_{\mathrm{I}}(g)$ has been inspired by Ref. [7]. Interestingly, the observed change in dependence of $\ln\Lambda$ on g occurs near the gas-to-liquid phase boundary, which, since $\lambda_D/a_{ws} = 1/\sqrt[3]{3g}$, also coincides with the regime where the Debye length becomes smaller than the average inter-particle spacing. Therefore, assuming Debye theory is approximately valid for $g > 1/3$, it is reasonable to expect the ion-ion cross-section is proportional to λ_D^2 and thus $\ln\Lambda \propto \lambda_D^2 T^2 \propto g^{-2}$ in agreement with the fit.

For reference, the structural phases of the ion cloud are presented in Fig. 4.4 by the pair correlation function [102] $G(r/a_{ws}) = (4\pi\rho_i r^2)^{-1} dN/dr$ for three different g values, as determined by molecular dynamics simulation. For the solid phase $G(r/a_{ws})$ exhibits a sharp peak at $r/a_{ws} \sim 1.7$, confirming a highly-ordered crystal structure, which disappears as the

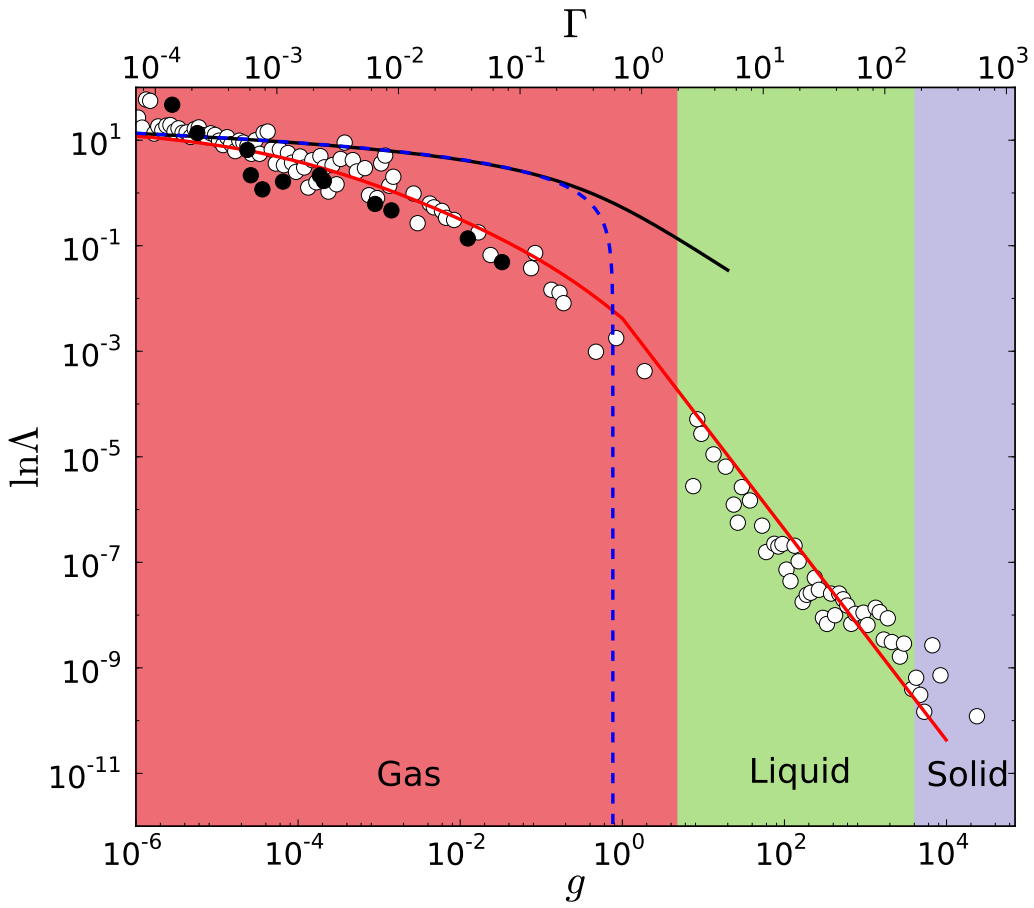

Figure 4.3: The experimental (black dots) and molecular dynamics (white dots) determinations of $\ln \Lambda$ versus g. Despite large variation in trap parameters (see text) the observed values fall along the same curve, indicating a 'universal' form for $\ln \Lambda$. The red line represents the best fit described in the text, while the black and dashed line are the results of Ref. [7] and $\ln(0.765/g)$ [8], respectively.

ion cloud moves into the liquid and gas phases. For the gas phase, $G(r/a_{ws})$ is smoothly falling, a signature of free-moving gas trapped in a parabolic potential.

Shown at the right of Fig. 4.3 are the secular velocity distributions of the ions for three selected g values. In this figure the points are a histogram of the simulated secular velocity distribution, while the solid curve is the Maxwell-Boltzmann (MB) velocity distribution expected for the calculated temperature. Clearly, the simulation results for the gas and liquid phases are consistent with the MB distribution, confirming the appropriateness of the

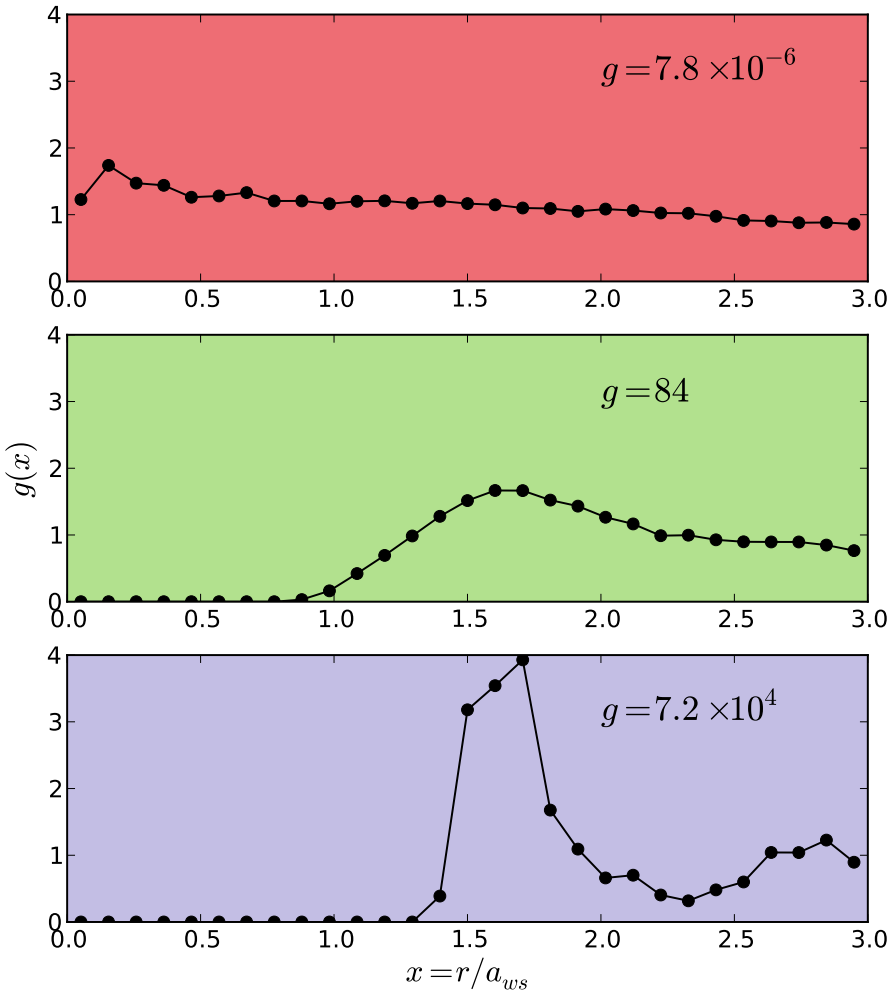

Figure 4.4: Pair correlation function $g(r/a_{ws})$ for selected g-values from molecular-dynamics simulation. From top to bottom are $g(r/a_{ws})$ for gas, liquid and solid phase.

Chandrasekhar-Spitzer rate in deriving Eq. 4.3. For the solid phase, the velocity distribution exhibits a significant power-law tail, violating the assumptions of Eq. 4.3 and preventing an accurate determination of $\ln \Lambda$ in this phase.

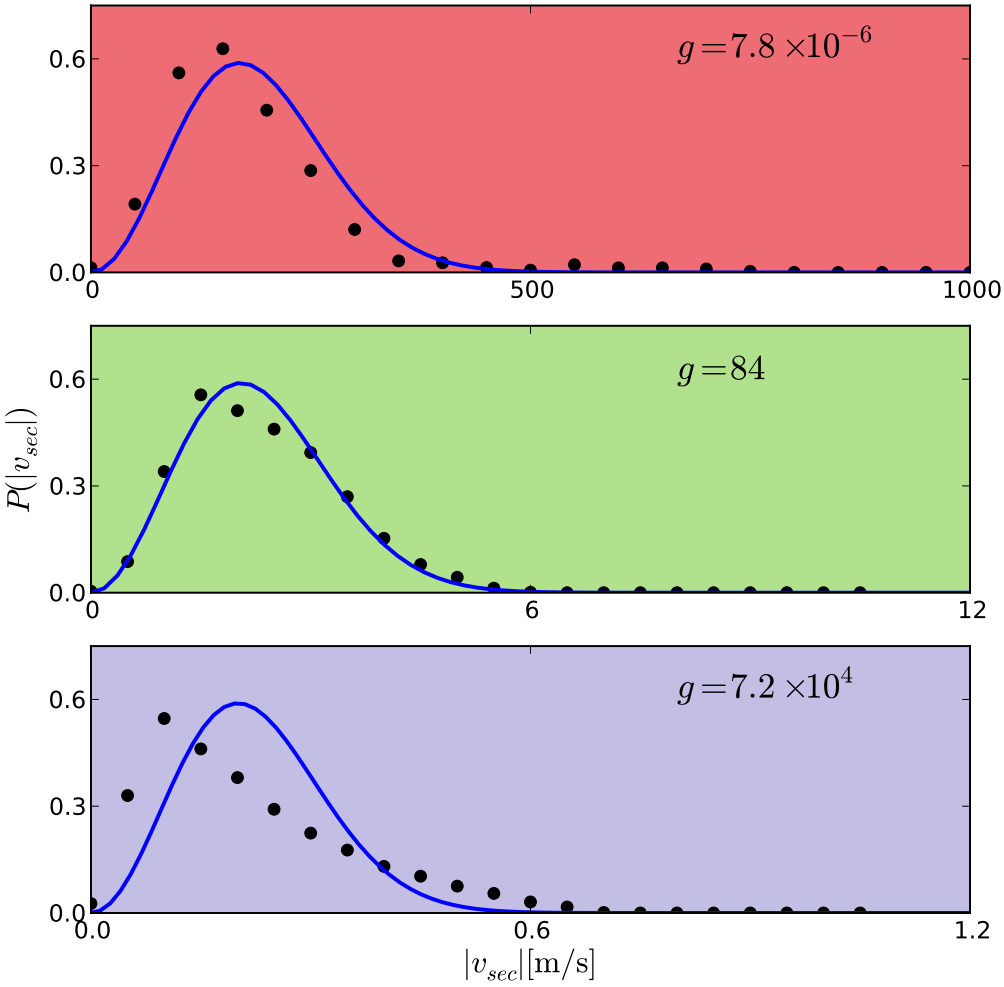

Figure 4.5: Secular velocity distribution function $P(|v_{sec}|)$ for selected g-values from molecular-dynamics simulation. From top to bottom are $g(r/a_{ws})$ for gas, liquid and solid phase.

4.5 Discussion

Several analytical results can be derived using Eq. 4.5 that provide insight into the plasma dynamics and have important consequences for quantum computation with trapped ions. First, for $g \ll 1$, $\ln \Lambda$ can be approximated as a constant (as is typical for low density plasma [103]) and Eq. 4.3 integrated, yielding $T_{sec} \propto t^{1/3}$. In this regime, the ion temperature grows

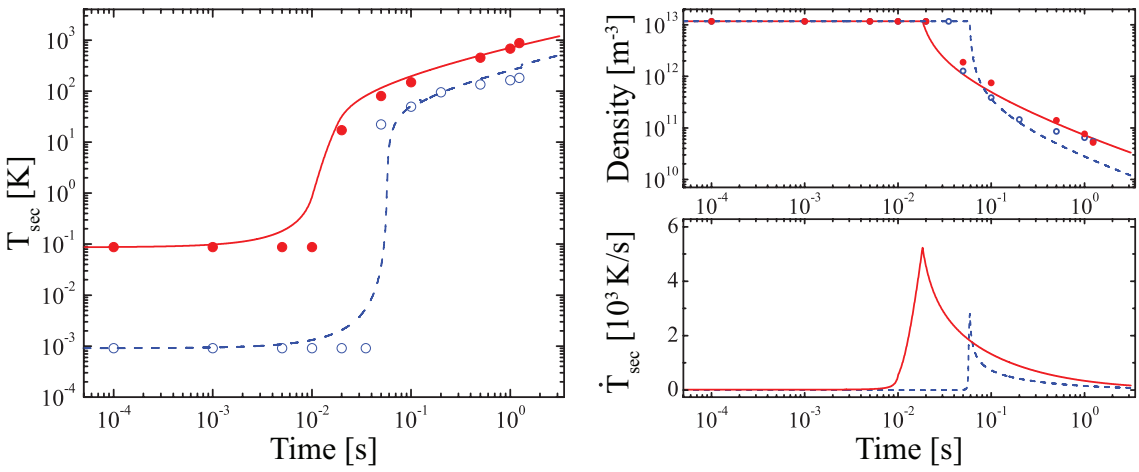

Figure 4.6: Comparison of experimental temperature, density and heating rate (dots) for two ion clouds ($N = 280$ (blue) and $N = 2800$ (red)) as a function of time to the result predicted by Eq. 4.3 with $\ln\Lambda$ given by Eq. 4.5 (line).

slowly until it is eventually balanced by evaporative loss from the trap or sympathetic cooling from residual neutral background gas. Second, assuming that $T_{ex} \gg T_{sec}$ in the initial ion crystal, Eq. 4.3 can be directly integrated for $g > 1$ yielding $T_{sec} = [c(t_m - t)]^{-2}$, where $c = f_1(1)2\pi\epsilon_0 k_B^{3/2}\bar{\epsilon}\eta T_{ex}/(\sqrt{m}e^2)$ and the time of the dramatic rise in temperature as the ions move into the gas phase is $t_m = T_{sec}^{-1/2}(t=0)/c$, which in the case of our experiment we have found it is accurate to within 10 ms. Interestingly, in quantum computation with strings of trapped ions the computational gate operations occur with the laser cooling extinguished. Therefore, t_m represents the upper limit for the time to implement a computational algorithm since, once the ion string melts, the quantum information is lost and the register must be reinitialized. For the parameters of *e.g.* Ref. [104] with 14 ions and $T_{ex} \approx 1$ mK, we find this fundamental limit to be $\sim 10^3$ s. If this system is scaled to a larger number of ions, as necessary for many practical quantum computation applications, t_m will be significantly reduced if excess micromotion is not controlled and may limit the number of possible gate operations. Likewise, recent proposed experiments to use kinked ion chains to study the Kibble-Zurek mechanism [105] and the coherence of discrete solitons [106] will be fundamentally limited to timescales less than $1 \sim 10$ s. In addition to providing the upper limit for a single computation/simulation, the expression for t_m can be used to guide future efforts. For

example, linear string geometries of heavy ions at low Mathieu q parameter should exhibit the longest lifetimes.

Finally, to demonstrate the utility of the expression for $\ln\Lambda$, Fig. 4.6 compares experimental data for two ion clouds of different size ($N = 280$ and 2800), taken in the same manner as the data of Fig. 4.1, with the temperature and density predicted by the integration of Eq. 4.3 using Eq. 4.5. In addition to providing a simple means to accurately calculate the thermodynamic properties of a system of trapped ions, these expressions explain several well-known experimental observations. For example, the smaller ion-ion heating rate (Fig. 4.6(c)) in the solid phase is due to ion-ion correlation as quantified through $\ln\Lambda$.

4.6 Conclusion

In conclusion, we have measured the heating rate of ions trapped in a linear rf Paul trap due to micromotion interruption. These data, and detailed molecular dynamics simulations, have been used to determine the value of $\ln\Lambda$ over a range of $10^{-7} \leq g \leq 10^{3}$. Though most determinations of $\ln\Lambda$ are process dependent [90], we expect our results to be comparable to $\ln\Lambda$ in other one-component plasmas for $g \ll 1$, as the Mathieu trajectories accurately describe the ion motion in this regime. This expectation is supported by the fact that our result converges to the traditional Landau-Spitzer result in this regime. However, as g grows the Mathieu solutions provide a less accurate description of the ion trajectories, leading to a change in e.g. $\bar{\epsilon}$. If future theoretical work accounts for these effects, then our measurement might be reinterpreted to give a model independent determination of $\ln\Lambda$, which we expect to be similar to the form suggested by Dimonte and Daligault [7]. Nonetheless, in its current form our result permits a simple, yet accurate, analytical description of ion cloud temperature, density, and structural phase transitions in a linear Paul trap. Thus, it should be immediately useful to a number of experimental efforts, including the growth of large ion crystals [107], sympathetic cooling of atomic or molecular ions [34, 108, 39], and trapped-ion quantum information.

CHAPTER 5

Photodissociation Spectroscopy of $BaCl^+$

5.1 Introduction

Ultracold molecular ions in the rovibronic ground-state hold immense promise for fundamental research in physics and chemistry. Of particular interest are novel applications to quantum chemistry [109]; a better understanding of interstellar cloud formation [110] and the identification of potential carriers of the diffuse interstellar bands [111]; the implementation of scalable quantum computation architecture [48]; and precision measurement tests of fundamental physics [14]. In pursuit of these goals, several groups have recently initiated work [39, 38, 1, 33] to realize samples of cold, absolute ground-state molecular ions. In fact, Refs. [38, 1, 33] have already reported the demonstration of species-specific cooling methods to produce molecular ions in the lowest few rotational states.

While these molecular ion cooling efforts, which include ultracold atom sympathetic cooling [39], rovibrational optical pumping [38, 1], and state-selective ionization [33], are diverse in approach, they share the common need for detailed spectroscopic understanding of diatomic ions. However, compared to that of neutral molecules, spectroscopic data for molecular ions is scarce. This can be attributed to the typically short lifetimes of molecular ions due to fast ion-molecule reactions and rapid diffusion under the influence of small electric fields [46]. A systematic review of the available spectroscopic data for simple diatomic ions was carried out by Berkowitz and Groeneveld [112] in 1983. In recent years, interest has shifted towards large molecular ions, atomic and molecular clusters, and multiply charged ions [113]. Thus, for ultracold molecular ion research to realize its full potential, a new effort in small molecular ion spectroscopy is required.

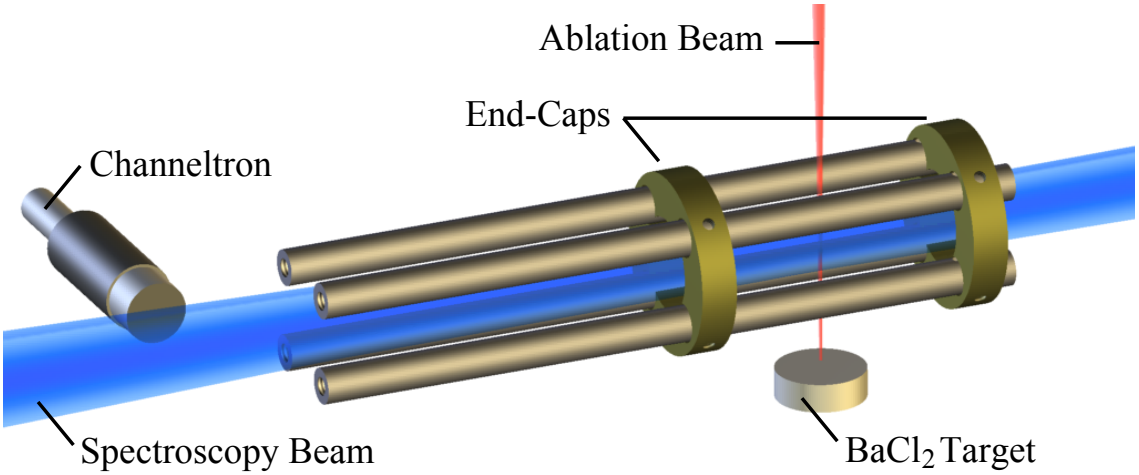

Figure 5.1: A schematic of the depletion spectroscopy apparatus based on a linear Paul trap.

Here, we report the use of a simple and general technique to record the first spectroscopic data for $BaCl^+$ – the molecular ion we have proposed to cool in Ref. [39]. As an ionically-bonded molecule composed of two closed-shell atomic ions, Ba^{2+} and Cl^-, $BaCl^+$ exhibits reduced chemical reactivity compared to other ions and is energetically forbidden from undergoing two-body chemical reactions with the ultracold calcium atoms proposed to use as a sympathetic coolant in Ref. [39]. Further, its large dipole moment and convenient rotational splitting are promising for cavity QED experiments [48]. Thus, these results are important not only as the demonstration of a technique for recording molecular ion spectroscopy, but also as an important first step towards the use and application of a generic, robust method for the production of cold ground-state molecular ions.

Spectroscopic data is taken using a trap-depletion approach. $BaCl^+$ ions are trapped in a linear Paul trap in the presence of a room-temperature He buffer gas and photodissociated by driving an electronic transition from the ground $X^1\Sigma^+$ state to the repulsive wall of the $A^1\Pi$ state. Ion trap parameters are carefully chosen to ensure that the photodissociation products are not trapped. The photodissociation spectrum is then recorded by simply monitoring the induced ion trap loss as a function of excitation energy. This technique, which we estimate should be easily applicable whenever the photofragments' mass-to-charge ratio differs by $\geq$15% from the parent molecular ion, may be a simple alternative to both photofragment

mass spectrometry [114] and storage ring based photodissociation spectroscopy [115].

In the remainder of this manuscript, we first give a detailed description of the experimental apparatus and technique. This is followed by the presentation of the first spectroscopic data for the $BaCl^+$ molecular ion. We continue with an ab initio calculation of the $BaCl^+$ molecular structure and thermalized photodissociation spectra, which we compare to the experimental observation.

5.2 Experiment Setup

Our apparatus, shown in Fig. 5.1, consists of a linear Paul trap housed in a vacuum chamber with a background gas pressure of 10^{-8} mbar. The ion trap is designed to allow radial loading of ions via laser ablation of a solid target, axial ejection of trapped ions into a channel electron multiplier for ion detection, and axial optical access for a spectroscopy beam. The ratio of the electrode radius r_e to field radius r_0 is $r_e/r_0 = 0.401$. A pressed, annealed target of $BaCl_2$ mounted below the ion trap is ablated by a $\sim$1 mJ, 10 ns pulse of 1064 nm laser radiation to create $BaCl^+$ molecular ions, which are trapped via the technique presented in Ref. [116]. A sample of Yb is mounted alongside the $BaCl_2$ target and is ablated to produce and trap Yb^+ ions, which are used as a control (described later). A leak valve is used to insert up to 10^{-3} mbar of He buffer gas into the chamber to enhance the trapping of high-energy ablated ions through sympathetic cooling. The spectroscopy beam is generated by a frequency-doubled pulse dye laser (PDL) capable of photon energies up to $49,000$ cm^{-1} with pulse energies of $\sim$1 mJ at a 10 Hz repetition rate.

Ablation is a complicated process that creates a plume of atoms, molecules, and clusters in various charge states [117], all of which can potentially be loaded into the ion trap. For this experiment it is critical that $BaCl^+$ is the only ablation product stable in the trap. Further, we require that the possible photodissociation products, *i.e.* Ba and Cl ions, are not trapped. To ensure the exclusivity of the trapping process, we record ion trap stability as a function of trap radiofrequency (rf) voltage and dc offset voltage at a rf driving frequency of $\Omega = 2\pi \times 200$ kHz. Based on the measurement of the trapped ion signal and comparison

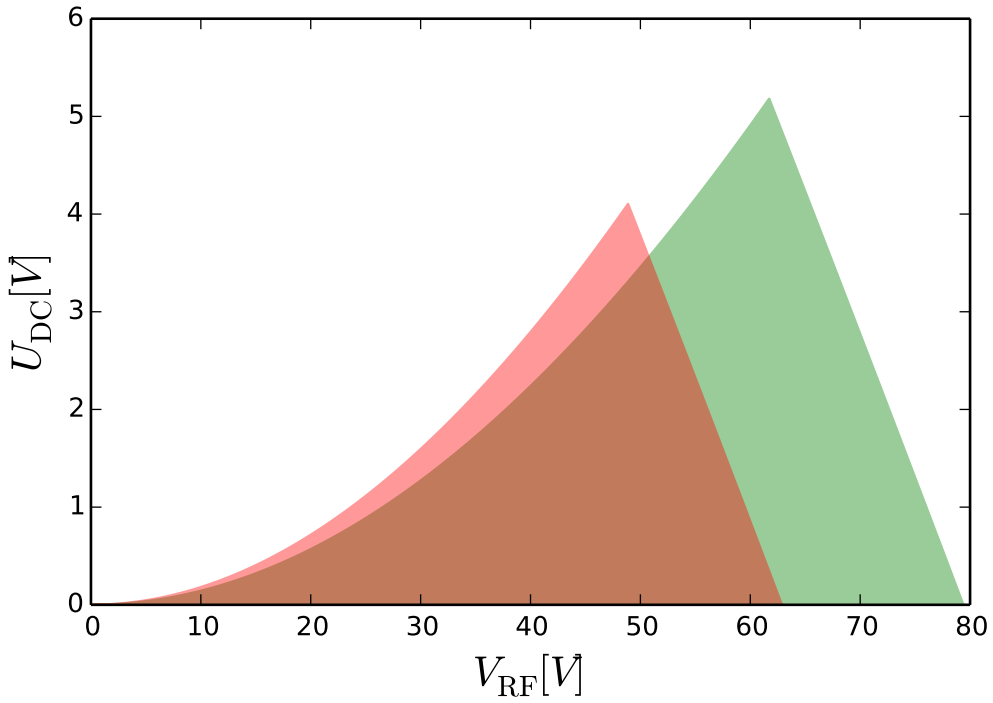

Figure 5.2: Ion trap stability region for Ba^+ (red) and $BaCl^+$ (green). Trap operates at green-only region, such that only $BaCl^+$ is stablely-trapped.

to theory [65], trapping parameters are chosen outside the stability region of Ba^+ (Fig. 5.2). The presence of singly-charged ions heavier than $BaCl^+$ is ruled out by the lack of significant ion detection when operating the trap for heavier ions. To further confirm the exclusivity of $BaCl^+$ in the trap, the resonant excitation spectra [65] of $BaCl^+$ and Yb^+, both with mass to charge ratio of $\sim$173, are recorded and compared.

This work contains the only spectroscopic information for $BaCl^+$ beyond a prior estimate of the ground-state dissociation energy, D_0, from a ligand field theory calculation [118], which suggests $D_0 = -38,500 \pm 1,100$ cm^{-1}. Using this energy as the minimum direct dissociation energy, we search for photodissociation using trap-depletion spectroscopy. During each measurement, $BaCl^+$ ions are loaded into the trap via ablation, where collisions with the He buffer gas cool the ions' translational motion to $\sim$300 K in ≤ 1 ms based on classical collision theory [119]. Next, the spectroscopy beam is unshuttered potentially photodissociating the trapped $BaCl^+$ ions into untrapped Ba^+ and Cl atom fragments. After a variable exposure

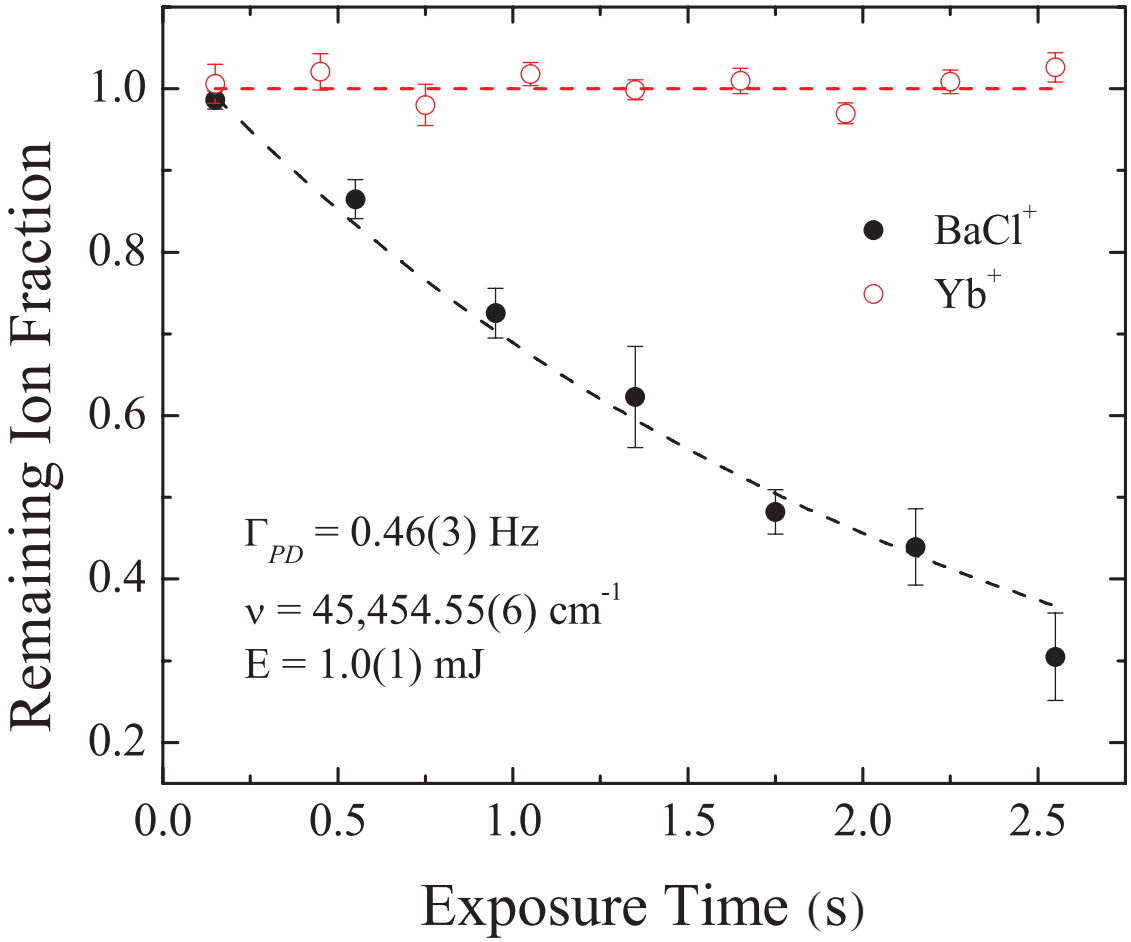

Figure 5.3: The effect of the PDL light on $BaCl^+$ and Yb^+. Each data point represents the mean of eight measurements with error bars reflecting the corresponding standard error. A single exponential decay curve is fit to the $BaCl^+$ data to calculate the photodissociation rate.

time, the spectroscopy beam is reshuttered and the remaining ions are axially ejected from the trap by grounding one of the end-cap electrodes. The ejected ions are then detected by a channel electron multiplier. The resulting ion signal is normalized to a control signal, for which the spectroscopy beam is always shuttered, in order to measure the fraction of ions remaining for a given exposure time. By repeating this procedure for a range of exposure times, a decay profile is measured and fit to a single exponential decay curve to obtain the photodissociation rate, Γ_{PD}. Typical data is shown in Fig. 5.3.

To rule out systematic effects due to species-nonspecific loss processes, such as collisions with spectroscopy-beam-induced photoelectrons that result when scattered UV light impinges on the metallic trap electrodes, we also observe the spectroscopy beam's effect on Yb^+ as shown in Fig. 5.3. For the range of photon energies used, we do not expect the PDL to induce a loss of Yb^+ through one-photon processes due to its high ionization potential, $\mathrm{IP}(Yb^+) = 98,207\ \mathrm{cm}^{-1}$ [120]. For all photon energies used, we do not observe any significant change in Yb^+ trap population, indicating the observed loss of $BaCl^+$ is species-specific.

To rule out systematic effects due to species-specific loss processes other than direct photodissociation, such as multi-photon ionization of $BaCl^+$, we measure the dependence of Γ_{PD} on the pulse energy and find a strong, linear relationship, shown in Fig. 5.4, indicative of a one-photon process. One-photon photo-ionization is ruled out by the high ionization energy of $BaCl^+$, $\mathrm{IP}(BaCl^+) \sim \mathrm{IP}(Ba^+) > 80,000\ \mathrm{cm}^{-1}$. This data, combined with the results of our *ab initio* calculations, confirms that the observed loss is due to single-photon photodissociation through the $A^1\Pi \leftarrow X^1\Sigma^+$ transition.

5.3 Measured Photodissociation Cross-section

The photodissociation cross-section is calculated as

$$\sigma_{PD}(\nu) = h\nu\frac{\Gamma_{PD}}{\overline{I}} = \frac{h\nu A}{r}\left(\frac{\Gamma_{PD}}{E}\right),$$

where Γ_{PD}/E is the fitted slope in Fig. 5.4, A is the PDL elliptical beam area, and the average light intensity for the $r = 10$ Hz repetition rate PDL is $\overline{I} = rE/A$. The measured photodissociation spectrum for a range of photon energies is shown in Fig. 5.5 alongside the results of our *ab initio* calculation (described later).

Statistical error in the measurement of the photodissociation cross section arises from the measurement of the photodissociation rate and the average intensity of the PDL light. Error in the photodissociation rate is determined by a nonlinear fitting algorithm and is typically $< 10\%$. The error in the average intensity is experimentally manifested in the measurement of the PDL pulse energy ($\lesssim 10\%$) and PDL beam area (typically $10-20\%$). Ultimately, the

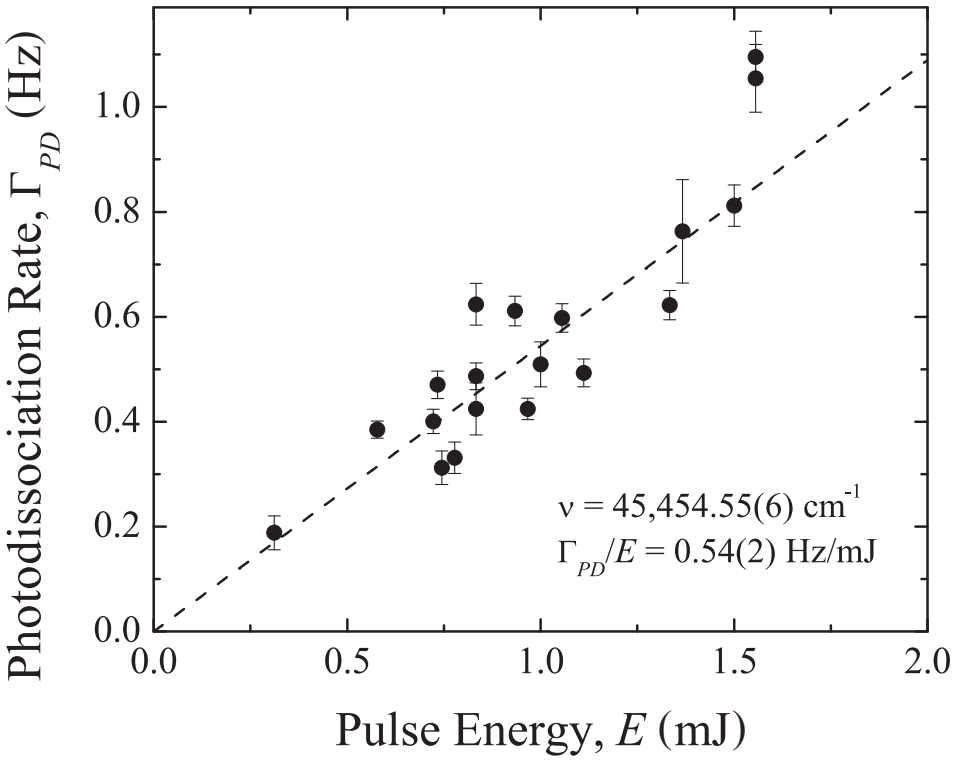

Figure 5.4: Measured $BaCl^+$ photodissociation rate versus PDL pulse energy. The linear dependence is indicative of a one-photon photodissociation process. Each point is the result of a decay rate fit shown in Fig. 5.3 with error bars reflecting fitting error.

total statistical error for photodissociation cross-section values is $< 30\%$.

The majority of the systematic error in the measurement is attributed to deviations from optimal overlap between the trapped ions and the PDL light, which leads to systematically underestimating the photodissociation rate. To counter this problem, we ensure to align the beam such that the photodissociation rate is maximized – however, optimization is limited by the variation in ablation yield. We estimate a total systematic error $\leq 40\%$.

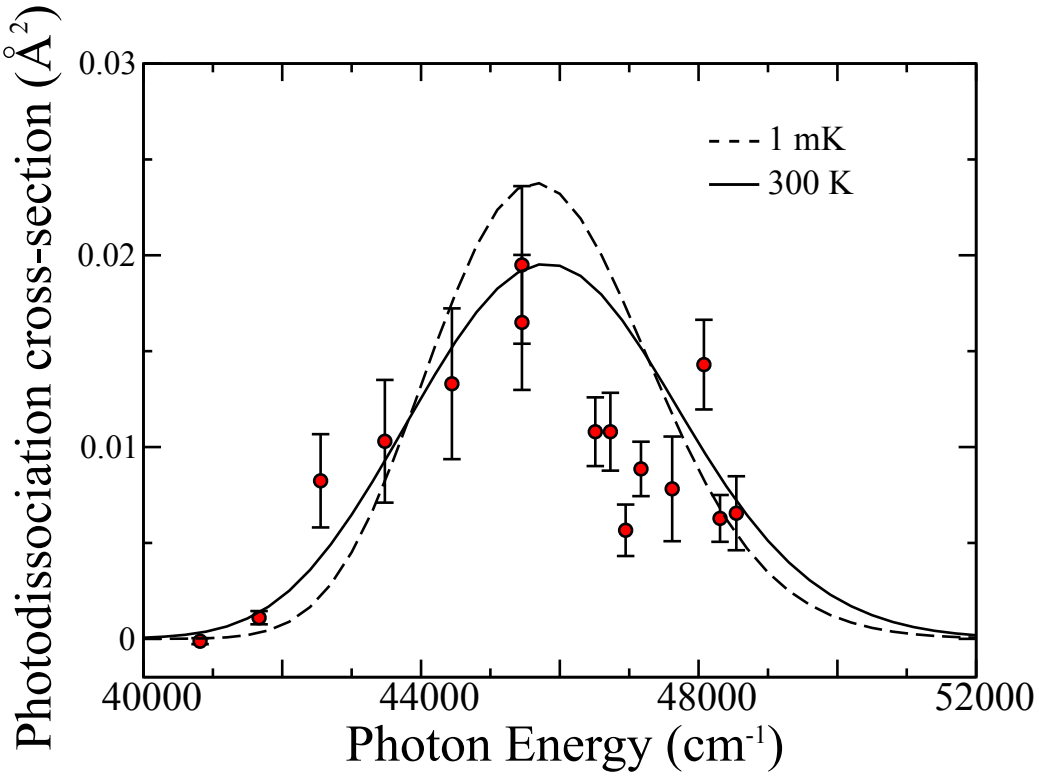

Figure 5.5: Experimental and theoretical cross-section values for the $A^1\Pi \leftarrow X^1\Sigma^+$ transition as functions of the photon energy. Each data point is associated with set of data similar to that in Fig. 5.4. The theoretical curves are thermally averaged for temperatures of 300 K and 1 mK.

5.4 Quantum Chemistry Calculation, Reflection Principle

To interpret the recorded photodissociation spectrum we have calculated the ground and lowest excited electronic potentials of the $BaCl^+$ molecular ion, see Fig. 5.6, using a non-relativistic multi-configurational second-order perturbation theory (CASPT2) implemented in the MOLCAS software suite [121]. The potential curves relevant to the experimental observation have solid lines and are labeled $X^1\Sigma^+$ and $A^1\Pi$ for the ground and first excited states, respectively – spectroscopic constants are given in Tab. 5.1. To our knowledge there exists no $BaCl^+$ electronic potentials derived from experimental observation. Comparing

our theoretical energies at large internuclear separations to the experimental energies of the Ba^+ and Cl atoms, we find differences of approximately 300 cm^{-1}. In addition, our value for $D_0 = D_e + \omega_e/2$ = -38,891 cm^{-1} for the $v = 0, J = 0$ level of the X state is consistent with the value D_0 = -38,500 ± 1,100 cm^{-1} of Ref [118]. Conservatively, we estimate a 3% uncertainty in our spectroscopic constants. Other $^1\Sigma$ (dashed lines) and $^1\Pi$ (dash-dotted lines) potentials shown in Fig. 5.6 are presented for completeness. A detailed description of these and other symmetry potentials will be given in a forthcoming publication [122].

Using these potentials we have developed a quantum mechanical model of the photodissociation process $BaCl^+(X^1\Sigma^+, vJM) + h\nu \rightarrow BaCl^+(A^1\Pi, J'M') \rightarrow Ba^+(6s) + Cl(3p^5)$ with photon energy $h\nu$ and kinetic energy release E. Based on the Franck-Condon principle, the absorption of a photon occurs for an internuclear separation where the kinetic energies in the initial and intermediate state are the same [123]. Fig. 5.6 shows this separation by a vertical arrow for the $v = 0$ vibrational level of the $X^1\Sigma^+$ state to the continuum or scattering states of the $A^1\Pi$ potential, leading to a Ba^+ ion and Cl atom. For the photon energies used in this experiment, this is the only viable dissociation pathway. Thus, the photodissociation cross-section for each rovibrational level vJ of the $X^1\Sigma^+$ state, assuming equal population in projections M and linear photon polarization, is [124]:

$$\sigma_{vJ}(\nu) = 4\pi^2 \alpha a_0^2 \frac{h\nu}{E_h} \frac{1}{2J+1} \sum_{J'MM'} \frac{|\langle A, E, J'M'|d_z|X, vJM\rangle|^2}{(ea_0/\sqrt{E_h})^2} \tag{5.1}$$

where E_h is the Hartree, a_0 is the Bohr radius, and α is the fine-structure constant. The quantity $\langle A|d_z|X\rangle/(ea_0/\sqrt{E_h})$ is dimensionless and contains both the radial and angular parts of the dipole moment. To evaluate the dipole matrix element, we have used a MRCI

Table 5.1: Theoretical CASPT2 molecular spectroscopic constants of $BaCl^+$. The estimated uncertainty is 3%.

State	$R_e[a_0]$	$D_e[cm^{-1}]$	$\omega_e[cm^{-1}]$	$\omega_e x_e[cm^{-1}]$	$B_e[cm^{-1}]$
$X^1\Sigma^+$	4.85	-39 055	328.3	-1.56	0.0918
$A^1\Pi$	6.42	-2 075	90.53	-1.26	0.0524

electronic-structure method, developed in Ref. [125]. For reference, at R_e of the $X^1\Sigma^+$ state, the dipole moment is $\sim 0.2\ ea_0$, which is solely due to the $Ba^{2+}Cl^-$ character of the electronic wavefunction.

For comparison with experimental data, we thermally average the photodissociation cross-section as

$$\sigma_{PD}(\nu) = \langle \sigma(\nu) \rangle_T = \frac{1}{Z} \sum_{vJ} (2J+1) \sigma_{vJ}(\nu) e^{-E_{vJ}/(kT)},$$

where Z and k are the partition function and the Boltzmann constant, respectively. In Fig. 5.5, the agreement between the experimentally observed and the theoretical $T = 300$ K photodissociation cross-section is shown to be good, indicating that the dissociation energy, dipole moment, and the slope of the A state potential at R_e of the X state potential are accurate.

Reflection Principle The fact that the measured photodissociation cross-section resembles a Gaussian shape is not a coincidence. As a matter of fact, the cross-section reflects the square of the ground state vibrational wavefunction. This so-called "reflection principle" [Ref] can be understood by first realizing that near classical turning point $R_c(E)$, the molecular potential $V(R)$ can be approximated linearly as

$$V(R) \approx E - \left| \frac{dV}{dR} \right|_{R_c} (R - R_c(E)) \tag{5.2}$$

where $R(E)$ is the classical turning point. Thus, as the solution to the radial Schrodinger's equation

$$\left(\frac{d^2}{dR^2} - \frac{2\mu}{\hbar^2} (V(R) - E) \right) \Psi(R) = 0, \tag{5.3}$$

the radial part of the continuum wavefunction $|A, E, J', M'\rangle$ is given by Airy function [126]

$$\Psi_A(R; E) \approx \xi \rho(E)^{1/2} \left| \frac{dV}{dR} \right|_{R_c}^{-1/2} \mathrm{Ai}\left(\xi (R_c(E) - R)\right) \tag{5.4}$$

where $\xi = \left| \frac{2\mu}{\hbar^2} \frac{dV}{dR} \right|_{R_c}^{1/3}$, $\rho(E)$ is the density of states. The pre-factor is chosen such that the wavefunctions are energy-normalized [127]

$$\int_{-\infty}^{\infty} \Psi_A(R; E_1) \Psi_A(R; E_2) dR = \rho(E_1) \delta(E_1 - E_2) \tag{5.5}$$

where $\rho(E) = E^{-1}$ is the density of states for the continuum states at energy E.

Shown in Fig. 5.7 is the continuum radial wavefunction for $A^1\Pi$ state calculated from Eq. 5.4. From $R = 0$ outward, $\Psi_A(R)$ continuously increases to a maximum near $R \approx R_c$, which is followed by rapid oscillation. In the calculation of matrix element, this oscillation tends to cancel one another out, leaving significant contributions solely from the probability amplitude at R_c. Mathematically, it has been shown in Ref. [128] that for many purposes, the following formula is valid,

$$\mathrm{Ai}(x) \approx \delta(x) + \frac{1}{3}\delta'''(x) \tag{5.6}$$

The initial radial wave function Ψ_X (shown in Fig. 5.7) and the transition dipole moment $d(R)$ (shown in Fig. 5.8) are smoothly varying functions, therefore it is safe to ignore the term $\frac{1}{3}\delta'''(x)$ in Eq. 5.6. Plugging Dirac delta function back into Eq. 5.1, the photodissociation cross-section is found to be proportional to $|\Psi_X(R_c)|^2$

$$\sigma_{vJ}(\nu) = \frac{4\pi^2\alpha}{e_0^2}\frac{h\nu}{2J+1}d^2(R_c)\,|\Psi_X(R_c)|^2\left|\frac{dV}{dR}\right|^{-1}_{R=R_c} \tag{5.7}$$

Since photon energy $h\nu$ is linear in R_c, cross-section $\sigma_{v,J}(\nu)$ as a function of ν thus reflects the square of probability amplitude of the initial state.

The vibrational energy splitting $v = 0$ state and $v = 1$ state is $\omega_e = 328.3\mathrm{cm}^{-1} \sim 469\mathrm{K}$ (see Tab. 5.1). At room temperature, around 80% of the $BaCl^+$ population is on $v = 0$ state. Therefore the shape of thermally averaged cross-section resembles the ground vibrational state, which is a Gaussian under harmonic approximation. For reference, the calculated photodissociation cross-section for $v = 0$ and $v = 1$ state, along with refined experimental cross-section taken with LQT-ToF device [3] are shown in Fig 5.9.

The thermalized photodissociation cross-section for a temperature of 1 mK is also presented in Fig. 5.5, where a weak dependence of the cross-section on T is evident. Thus, it would be difficult to use photodissociation spectroscopy to probe the internal molecular ion temperature. However, with the experimentally verified molecular potentials we have identified a strong predissociation channel between the first excited $^1\Sigma$ and $A^1\Pi$ states, which we are now investigating (see Section 6.1.1). It is expected that the rovibrational resolution

afforded by predissociation spectroscopy will allow us to efficiently measure molecular ion rovibrational temperatures [129], a crucial step in the demonstration of the method proposed in Ref. [39].

5.5 Conclusion

In conclusion, we have demonstrated a simple technique for molecular ion trap-depletion spectroscopy and used it to record the first experimental spectroscopic data for $BaCl^+$. We have also performed *ab initio* calculations of $BaCl^+$ structure and found good agreement with experimental data. From these results, we have reported the first spectroscopic constants for $BaCl^+$ and suggested assignments for the $BaCl^+$ molecular potentials. Finally, as $BaCl^+$ is a leading candidate for ultracold molecular ion experiments, this work represents a necessary step towards these important goals.

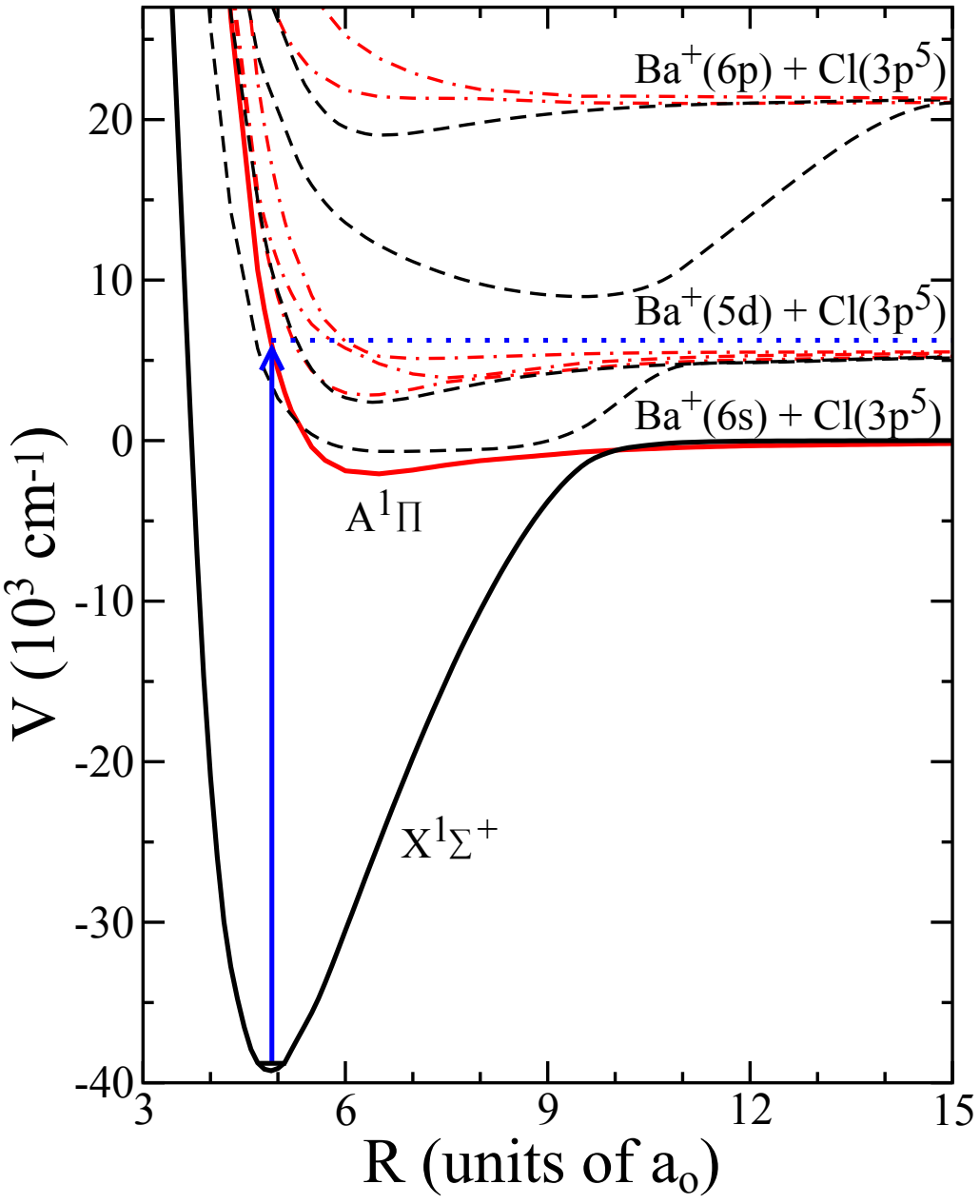

Figure 5.6: Potential energy curves of the $BaCl^+$ molecular ion as a function of the internuclear separation R. Solid, labeled curves indicate the potentials that are involved in the photodissociation scheme. Other $^1\Sigma^+$ ($^1\Pi$) potentials are shown by dashed (dash-dotted) lines. The vertical arrow indicates the $A^1\Pi \leftarrow X^1\Sigma^+$ single-photon photodissociation transition.

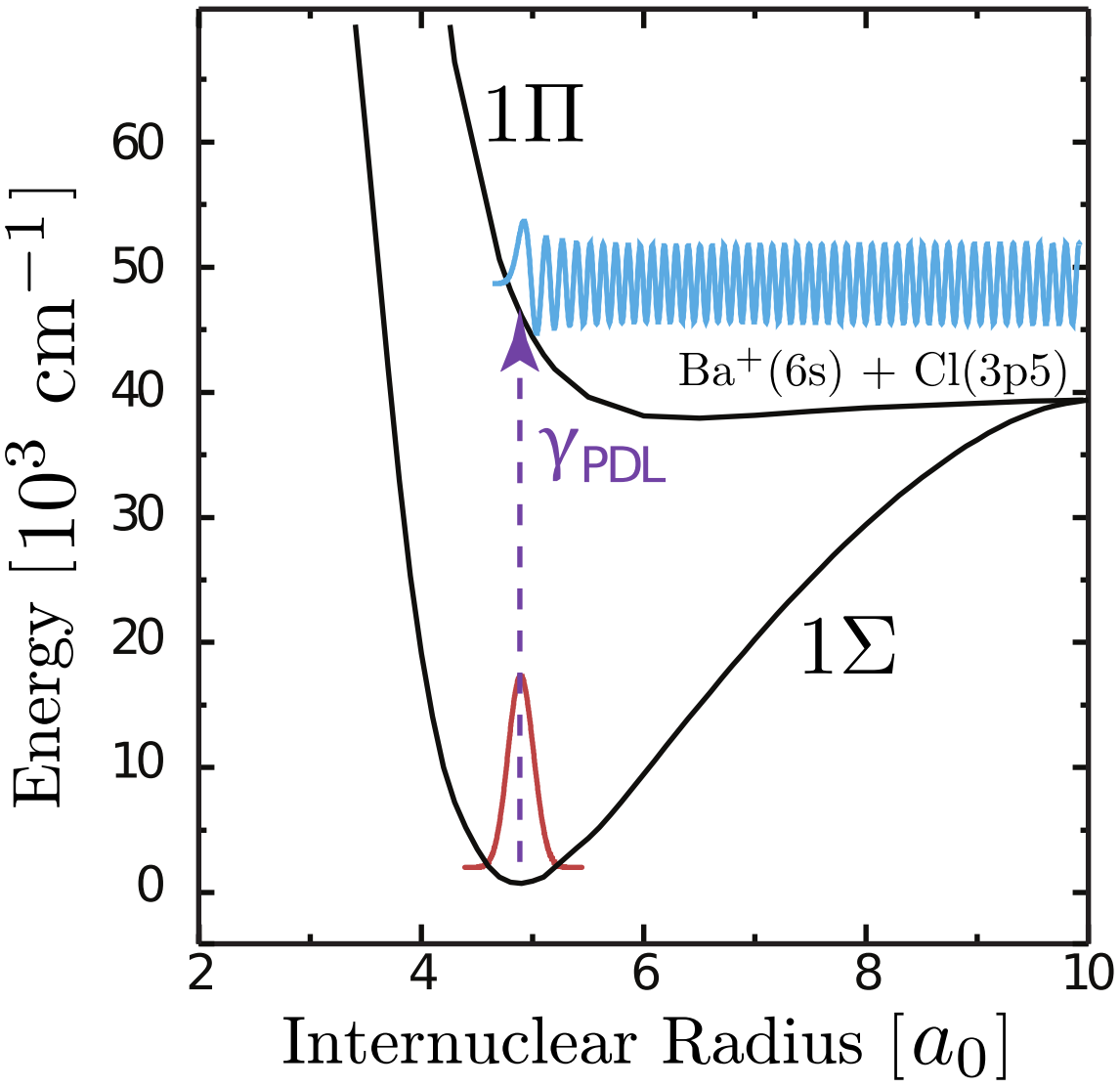

Figure 5.7: Simplified $BaCl^+$ photodissociation scheme, with ground (red) and excited (blue) vibrational wavefunctions.

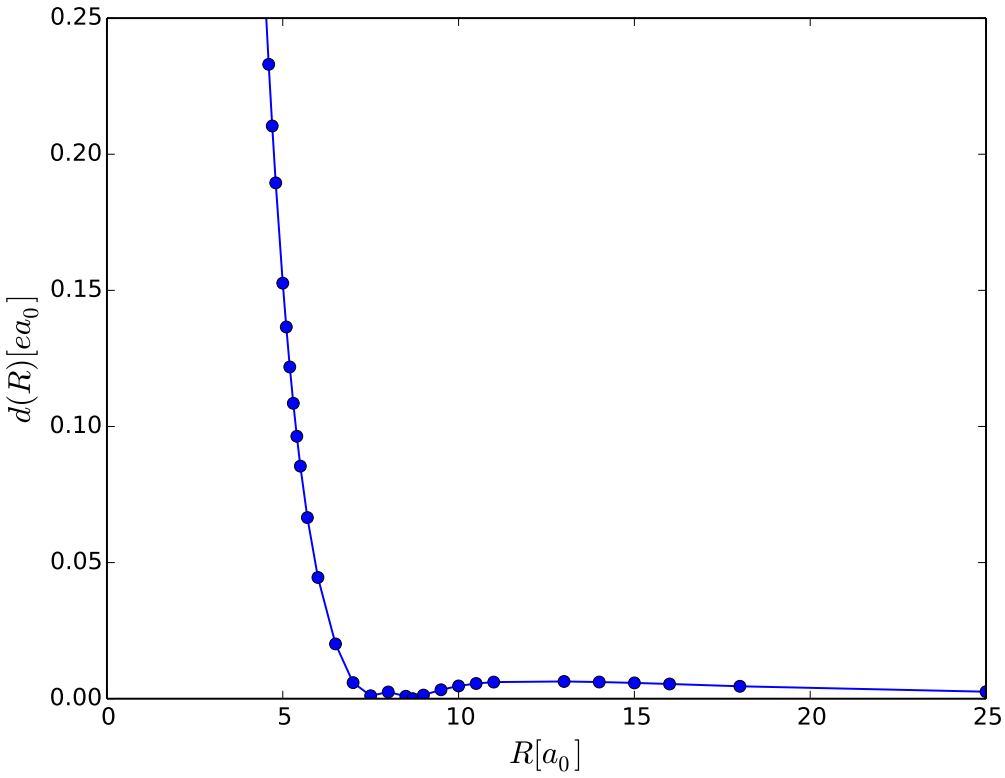

Figure 5.8: Transition dipole moment for $BaCl^+$ A← X transition.

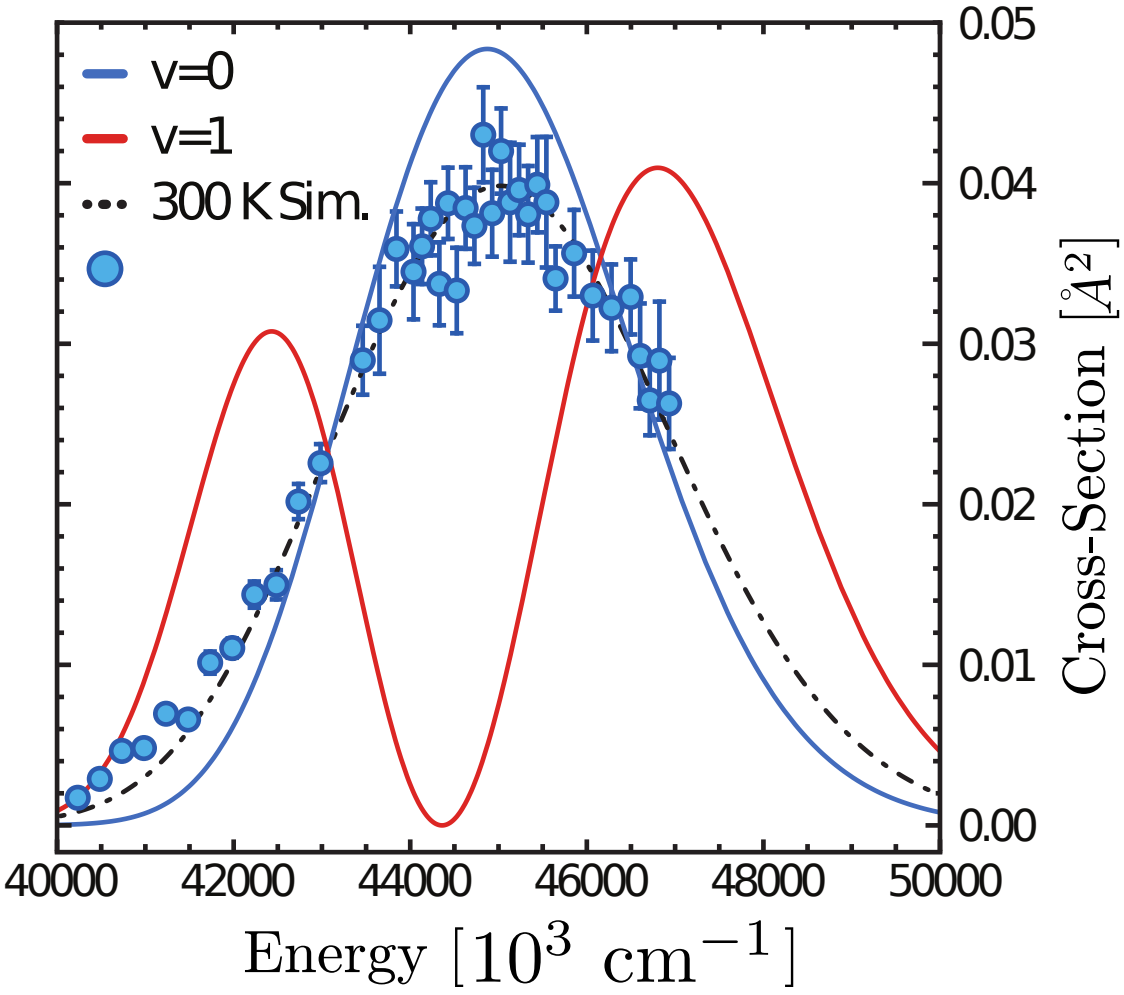

Figure 5.9: Refined $BaCl^+$ direct photodissociation cross-section taken from [9] using LQT-ToF device in [3].

CHAPTER 6

Outlook

6.1 Rotational State-selective Spectroscopy for Molecular Ions

Stated in the previous chapter, direct photodissociation spectroscopy is not capable of resolving each ro-vibrational quantum state of $BaCl^+$. Two undergoing directions of state-selective spectroscopy experiments are predissociation spectroscopy and resonant-enhanced multi-photon spectroscopy. These are described below.

6.1.1 Predissociation Spectroscopy

In this method, a laser excites $BaCl^+$ from the initial state $X^1\Sigma(v'', j'')$ to an intermediate state $B^1\Sigma(v', j')$, close to the crossing between $B^1\Sigma$ and repulsive $A^1\Pi$ states, which undergoes predissociation with $A^1\Pi$ state due to non Born-Opponheimer term $\frac{J^{\pm}L^{\mp}}{2\mu R^2}$ in the molecular Hamiltonian. The calculated predissociation linewidth, detailed in the following section, is smaller than the spacing between rovibrational states, allowing the resolution of individual rovibrational state of $BaCl^+$.

Rate Equation Model We model the population dynamics by an effective three-state rate equation model with loss to unobserved states via spontaneous emission. This model includes the following effects.

1. Broadening effects

   Homogeneous broadening such as spontaneous emission into other bound $X^1\Sigma$ state and the finite linewidth of pulsed laser. Doppler broadening is also included.

2. Other Ba^+ creation pathways

   Spontaneous emission into the continuum of $A^1\Pi$ state or $B^1\Sigma$ state. Direct photodissociation from $X^1\Sigma$ state can also provide a smooth Ba^+ background signal.

3. Population re-distribution This is not included yet, but would account for relaxation mechanisms such as blackbody radiation and collision. This leads to a conservative estimate of Ba^+ yield.

4. Multiple excitation

   Multiple transitions could be excited if the laser linewidth is large and several transitions are very close in frequency.

Thus we model the population dynamics by rate equation:

$$\begin{aligned} \dot{n}_X &= \Gamma_{BX} n_X + \rho_L B_{BX}(n_B - n_X)g \\ \dot{n}_B &= -\Gamma_{BX} n_X - \rho_L B_{BX}(n_B - n_X)g - (\Gamma_{pred} + \Gamma_{loss})n_B - \Gamma_{dark} n_B \\ \dot{n}_{Ba^+} &= \sum_i (\Gamma_{pred} + \Gamma_{loss})n_B \end{aligned} \tag{6.1}$$

where

- n_{X_i}, n_{B_i} and n_{Ba^+} are the population of $X^1\Sigma$ and $B^1\Sigma$ state and Ba^+ ions.
- Γ_{BX} is the spontaneous emission rate.
- B_{BX} is the Einstein B-coefficient.
- ρ_L is the energy density of pulsed laser.
- g is the lineshape function that describes the various broadening mechanisms.
- Γ_{pred} is the predissociation rate from $B^1\Sigma$ to $A^1\Pi$ state.
- Other Ba^+ creation pathways are accounted for by Γ_{loss}.
- Γ_{dark} includes spontaneous emission into levels of $X^1\Sigma$ state that are not addressed by laser.

- Finally, summation is carried out over all possible $B^1\Sigma$-$X^1\Sigma$ dipole transitions that contribute to Ba^+ creation.

Calculations of these rates are detailed below.

Predissociation Rate Γ_{pred} The relevant mechanism in the predissociation of $BaCl^+$ is rotational perturbation [127], in which the nuclear rotation under the Born-Oppenheimer approximation gives rise to the mixing of $B^1\Sigma$ and $A^1\Pi$. The predissociation rate is given by Fermi's Golden rule

$$\Gamma_{pred}(v'', j'') = \frac{2\pi}{\hbar}\rho(E)|\langle\psi_A(E, j')|M|\psi_B(v'', j'')\rangle|^2 \tag{6.2}$$

where E is the energy shared by $A^1\Pi$ and $B^1\Sigma$ states denoted by $\psi_A(E, j')$ and $\psi_B(v', j'')$, and $\rho(E)$ is the density of $A^1\Pi$ states at energy E. M is L-uncoupling operator [127] given by

$$M = -\frac{1}{2\mu R^2}(J^+L^- + J^-L^+) \tag{6.3}$$

where μ is the reduced mass of $BaCl^+$, R is the internuclear distance, and $J(L)^\pm$ are the raising/lowering operator of total(orbital) angular momentum.

Under Born-Oppenheimer approximation, the total wavefunction for diatomic molecule can be broken into electronic, vibrational and rotational parts [127],

$$\Psi_{\Lambda,S,\Sigma,v,j,\Omega}(r; R, \theta, \phi) = \phi_{\Lambda,S,\Sigma}(r; R)\chi_{v,j}(R)\psi_{j,\Omega}(\theta, \phi) \tag{6.4}$$

where ϕ, χ, ϕ are the electronic, vibrational and rotational wavefunctions. r is the collective electronic coordinates, θ, ϕ are the spherical coordinates of internuclear vector. $\Lambda, S, \Sigma, \Omega$ are quantum numbers in Hunds coupling case (a). For reference, a schematic representation of them is depicted in Fig 6.1.

Likewise, Eq. 6.2 can be evaluated as product of coupling in radial, vibrational and rotational part, and the predissociation rate is given by

$$\Gamma_{pred}(v', j')[\text{Hz}] = \frac{16.85763}{\mu[\text{amu}]}\langle\frac{b(R)}{R[\text{Å}]^2}\rangle^2 j'(j'+1) \tag{6.5}$$

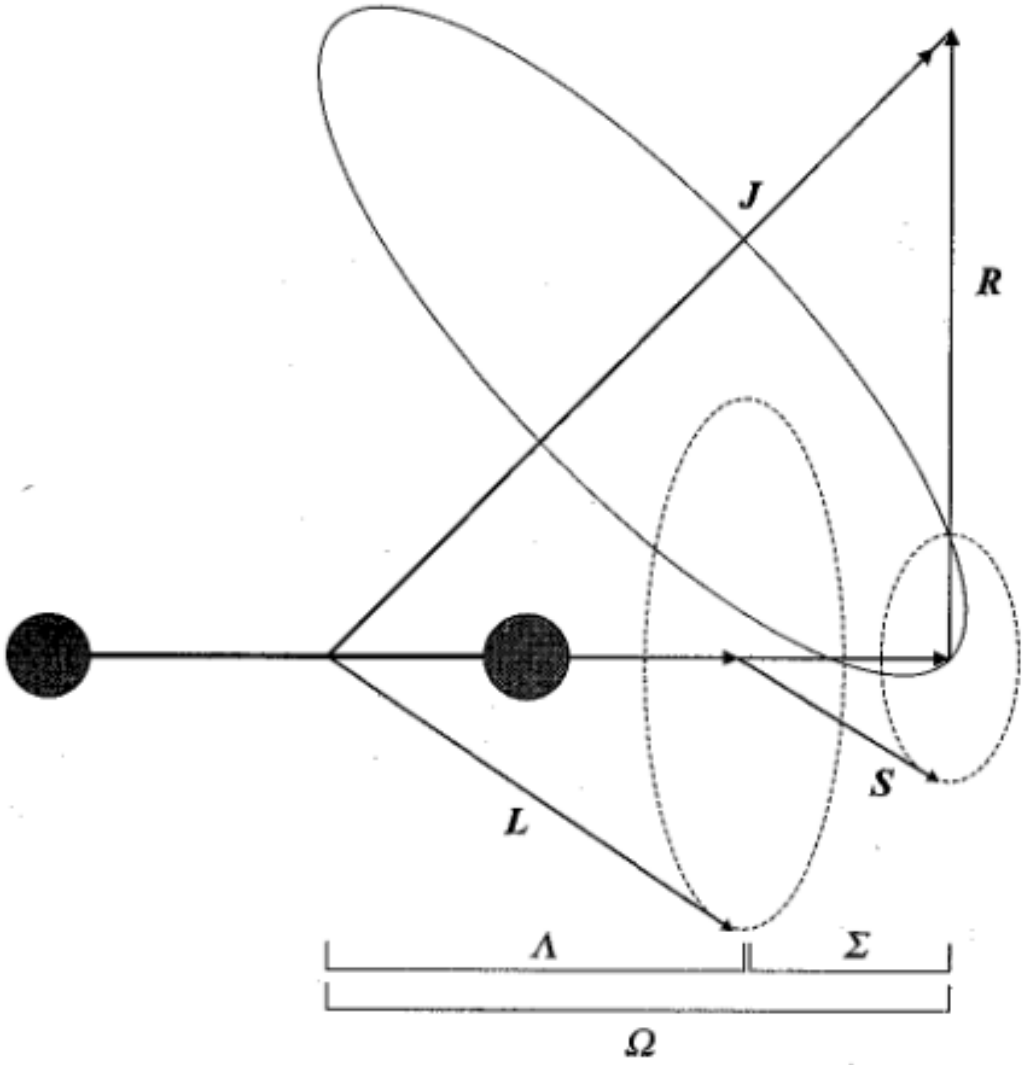

Figure 6.1: Hunds coupling case (a).

where $b(R)$ is a the matrix element of electronic angular momentum L^+,

$$\hbar b(R) = \langle \phi_A(r,R)|L^+|\phi_X(r,R)\rangle \tag{6.6}$$

. The value of $b(R)$ is provided from *ab initio* quantum chemistry calculations of molecular orbitals, shown in Fig. 6.2. The angled bracket denotes the following integral,

$$\left\langle \frac{b(R)}{R^2} \right\rangle \equiv \int_0^\infty \chi_A(R) \frac{b(R)}{R^2} \chi_B(R) dR \tag{6.7}$$

Predissociation rates calculated from Eq. 6.5 as a function of vibrational quantum num-

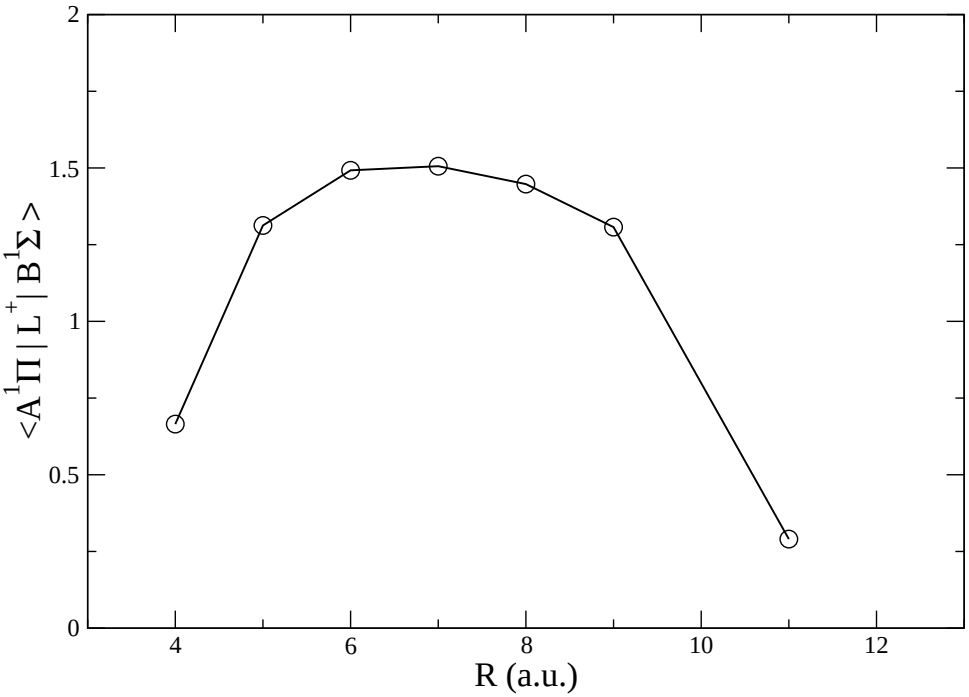

Figure 6.2: $b(R)$ calculated from $BaCl^+$ molecular orbitals of $A^1\Pi$ and $B^1\Sigma$.

ber v for constant j values are shown in Fig. 6.3. For example, Γ_{pred} for v'=34 and j'=1 and v'=59 and j'=1 are 2.2 MHz and 1.8 MHz respectively. Since $\Gamma_{pred} \propto j'(j'+1)$, simple scaling shows that predissociation broadens the B state by $\Gamma_{pred} \sim$ GHz for $j' \sim 30$.

Spontaneous Emission Rate Γ_{BX}, Γ_{Dark} The rate at which B state decays into other X state Γ_{dark} is calculated by

$$\Gamma_{dark}(v', j') = \sum_{v'', j'' \neq v_{initial}, j_{initial}} \Gamma_{BX}(v'', j'', v', j') \tag{6.8}$$

where $v_{initial}$ and $j_{initial}$ are the quantum numbers for the intital X state under consideration.

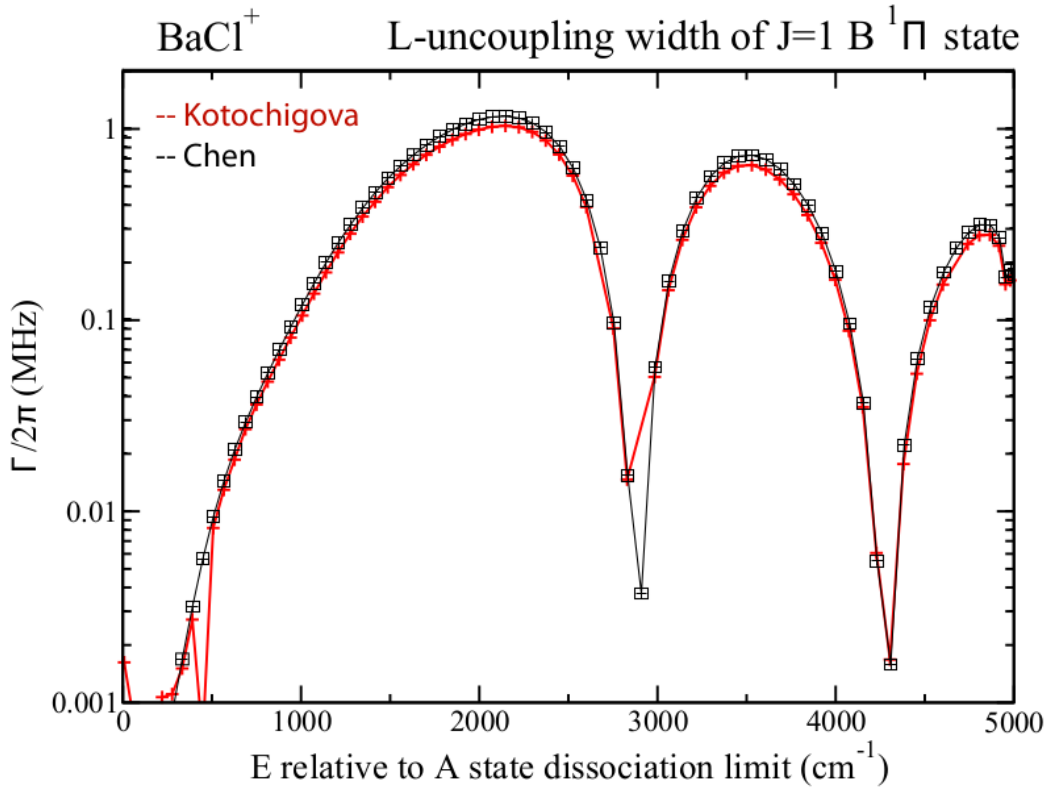

Figure 6.3: Calculated predissoication rate for ro-vibrational state (v',j').

The total radiative rate for a given (v', j') of $B^1\Pi$ potential is given by the summation,

$$\begin{aligned}\Gamma_{rad}(v', j') = \Gamma_{BX}(v', j') + \Gamma_{dark}(v', j') \\ + \sum_E \Gamma_{BX-cont}(E, v', j') \\ + \sum_E \Gamma_{BA}(E, v', j')\end{aligned} \tag{6.9}$$

where the first two terms are bound-to-bound transition. The rest are $B^1\Sigma$-$X^1\Sigma$ bound-to-continuum and $B^1\Sigma$-$A^1\Pi$ bound-to-continuum transitions, and E is the energy of continuum state. All these rates are calculated by LEVEL [130] or BCONT [131]. The calculation results are shown in Fig. 6.4.

Other Ba^+ creation channel Γ_{loss} These channels include any non-predissociation channel that contributes to more Ba^+, such as the transition from $B^1\Sigma$ state to the repulsive wall

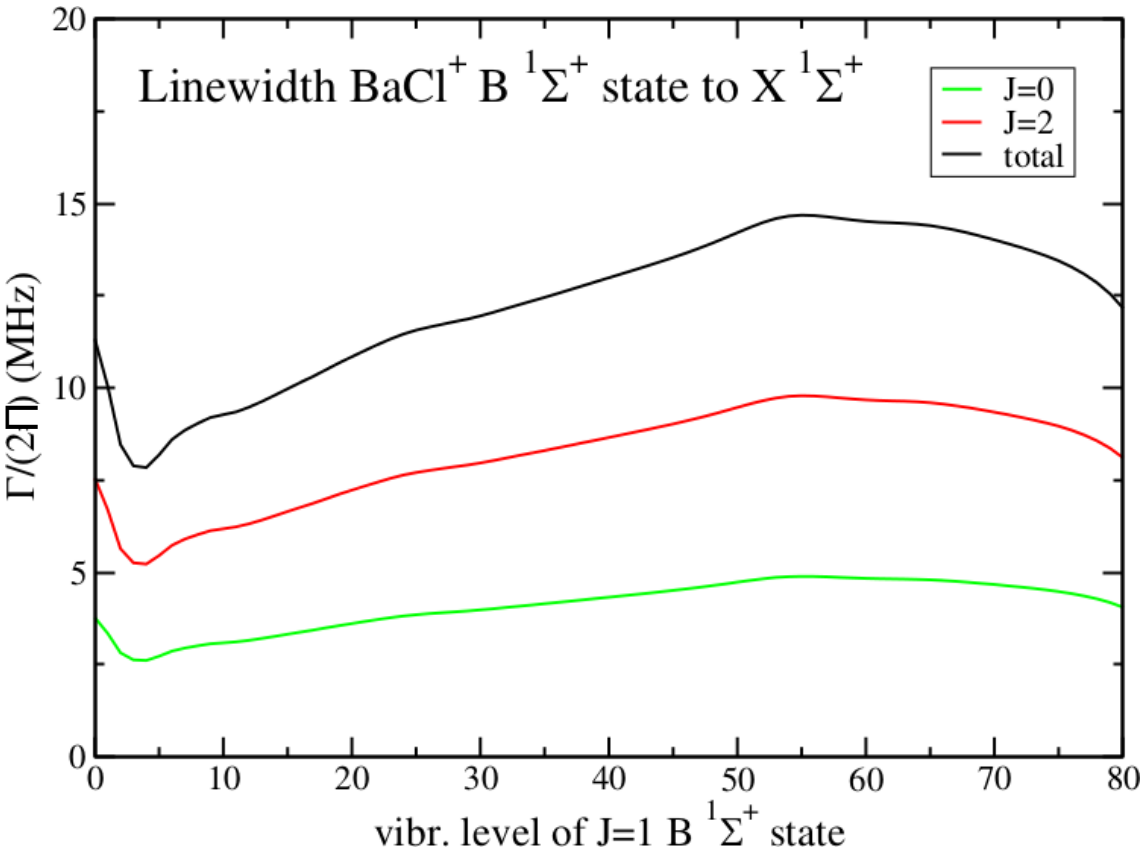

Figure 6.4: Calculated radiative lifetime for ro-vibrational state (v',$j' = 1$).

of $X^1\Sigma$ state or $A^1\Pi$ state. The rate Γ_{loss} is given by:

$$\Gamma_{loss} = \sum_E \Gamma_{BX-cont}(E, v', j') + \sum_E \Gamma_{BA}(E, v', j') \tag{6.10}$$

Lineshape Function g The lineshape function considered here is the convolution of all the broadening present in $BaCl^+$,

$$g(\nu) = V(\nu - \nu_0, \Gamma_{homo}, \Gamma_{inhomo}) \tag{6.11}$$

$$= V(\nu - \nu_0, \Gamma_{pred} + \Gamma_{rad} + \Gamma_{laser}, \Gamma_{Doppler}) \tag{6.12}$$

where $V(x, \sigma, \gamma)$ is the Voigt profile, with σ and γ being Gaussian and Lorentzian width respectively. ν_0 is the center of the transition. Γ_{pred} is the broadening due to predissociation of B state. Γ_{rad} is the broadening due to all other radiative processes. $\Gamma_{laser} = 0.12\text{cm}^{-1}$ is

the linewidth of pulsed dye laser. $\Gamma_{Doppler}$ is the thermal width of the transition, given by

$$\Gamma_{Doppler} = \nu_0 \sqrt{\frac{kT}{mc^2}} \tag{6.13}$$

Result We have carried out predissociation spectroscopy in the wavenumber range between 41986 and 41993 cm^{-1} at T=300K, as shown in Fig (6.5). Fragment Ba^+ ions are distinguished from $BaCl^+$ ion by their difference of time-of-flight. No obvious predissociation features have been found, on top of a direct photodissociation background indicated by the strip in the upper panel. Using the new time-of-flight spectrometer, Steven Schowalter has ruled out a broader spectral region including this one. More detailed data will be presented in his thesis.

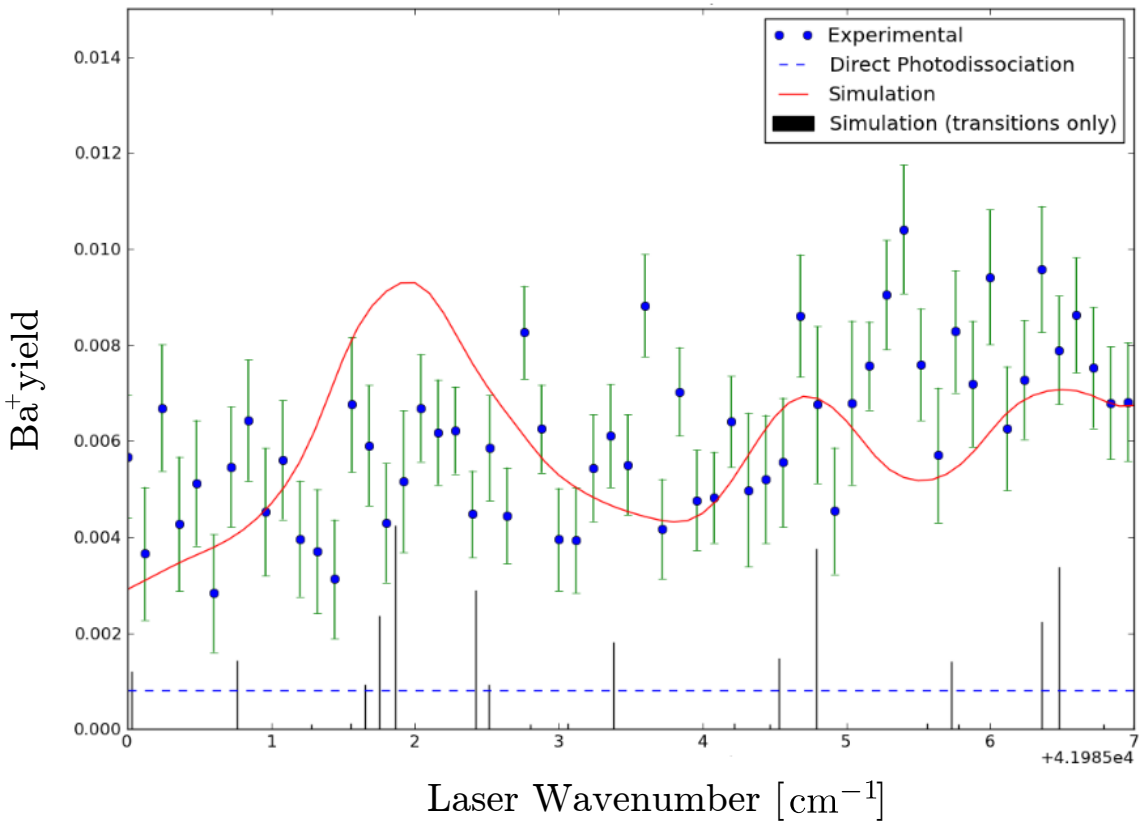

Figure 6.5: Preliminary measurement result of $BaCl^+$ predissociation spectrum (error bar), and comparison to theory (red line). Direct photodissociation background is denoted by the blue dashed line.

6.1.2 Resonantly-enhanced multi-photon dissociation

Under construction.

6.2 Sympathetic cooling of multiple ions

The sympathetic cooling of multiple ions via collisions with neutral gas poses a much bigger challenge than that of a single ion. Since ion-ion heating from micromotion interruption provides a large heating mechanism, multiple ions will reach a higher temperature than that of a single ion. For instance, a molecular-dynamics simulation shows that the temperature of 50 trapped $BaCl^+$ ions in a Ca MOT with density $\rho = \frac{1}{4} \times 10^{17}\text{cm}^{-3}$ reaches 20K, while a single ion will equilibrate to near MOT temperature at 5mK.

Shown in Fig. 6.6 is the competition of ion-ion heating and sympathetic cooling as a function of the ions' secular temperature. The ion-ion heating rates are suppressed at low temperature as a result of highly correlated motion of the ion (see Chapter 4), and at high temperature caused by reduced ion density. Consequently, the resultant shape of the ion-ion heating curve reaches a maximum at an intermediate temperature. The sympathetic cooling curve shows a monotonically decreasing trend as temperature is decreased. The steady-state temperature is where these two rates are equal and stable against fluctuations. As shown in Fig 6.6, the neutral atom has to be sufficiently dense, for the sympathetic cooling to overcome the ion-ion heating barrier to reach the low temperature necessary for quantum information and computation [48] applications.

6.3 Single ion in contact with two reservoirs - a model system to study non-equilibrium thermodynamics

In Chapter 2, we develop the theory of the single ion in contact with one reservoir. In reality, at any moment the ion is simultaneously in contact with multiple reservoirs at quite different temperatures. For the experiment proposed in Chapter 1 in addition to laser-cooled Ca atoms

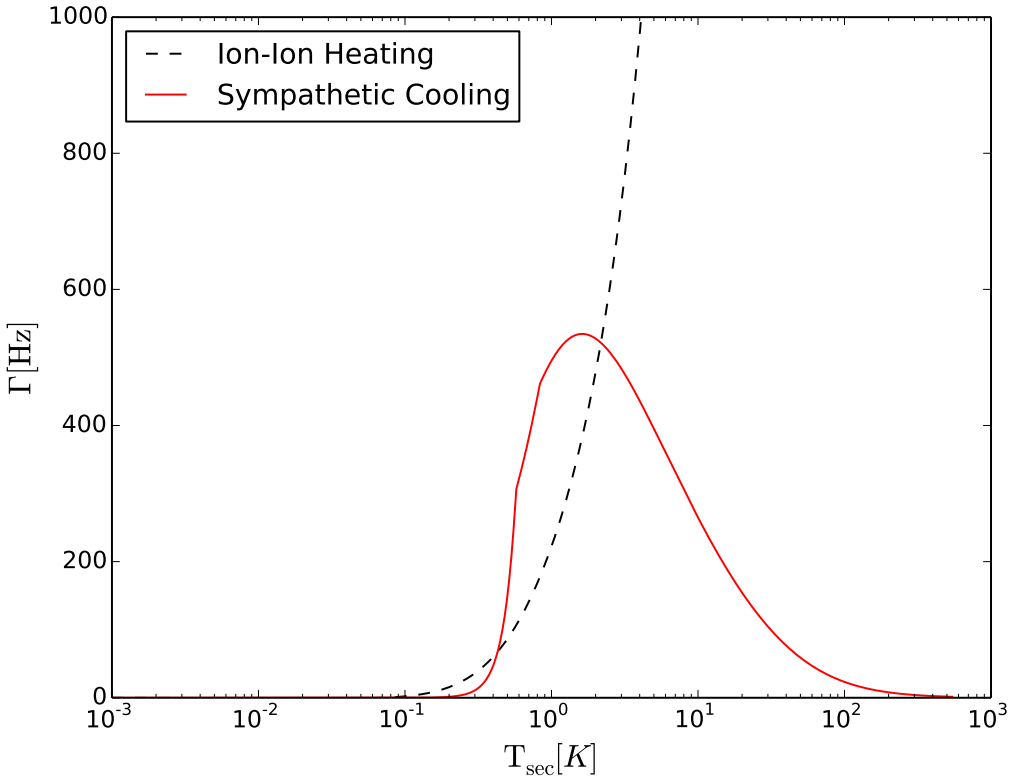

Figure 6.6: A schematic presentation of ion-ion heating (red solid line) and sympathetic cooling (black dashed line) for multiple ions in contact with laser-cooled atoms.

at temperature $T_1 \approx 5$mK, some residual hydrogen H_2 at room temperature $T_2 \approx 300$K still exist even with well-designed and well-baked UHV system. Now with these two neutral atoms, what is the temperature of the single ion?

When $T_1 = T_2$, ion's temperature is the common temperature $T = T_1 = T_2$ and at steady-state ion's energy E follows Boltzmann distribution,

$$P(E) = \frac{\exp(-E/k_B T)}{Z} \tag{6.14}$$

where Z is the partition function. However if $T_1 \neq T_2$, then there does not exist a general equation like Eq. 6.14 and temperature is ill-defined such system. In fact, $P(E)$ depends on the dynamics of the system and on its couplings with the two reservoirs [132]. To illustrate this, consider a really good vacuum with minimal amount of H_2 left, such that the ion undergoes frequent and infrequent ($\Gamma_1/\Gamma_2 = 100$) collisions with cold reservoir $T_1 = 5m$K,

and hot reservoir source $T_2 = 300$K, respectively. Presented in Fig 6.7, the results of Monte-Carlo simulation demonstrates that the steady-state velocity distribution is apparently not thermal described by 6.14. While the peak of the distribution closely resembles thermal distribution at T_1, the fat shoulder of the distribution indicates large velocity jump due to occasional collisions with hot reservoir.

Another way to illustrate the strangeness of this non-equlibrium system is to consider the average kinetic energy T_i at steady state. To calculate T_i, one might be tempted to write the change of ion's energy $\frac{dT_i}{dt}$ as the simple sum of heat exchange with two reservoirs,

$$\frac{d}{dt}T_i = \Gamma_1(T_1 - T) + \Gamma_2(T_2 - T) \tag{6.15}$$

with the steady state temperature found by setting $\frac{dT_i}{dt}$ equal to zero, yielding $T_i \approx 3K$. However, the average kinetic energy found from Monte-Carlo simulation is 30K, almost one order of magnitude higher!

To fully understand the kinetics of such system, we have initiated a collaboration of UCLA physics professor Robin Bruinsma. Our strategy is to begin with the master equation, and apply the Kramers-Moyal-van-Kampen expansion [133].

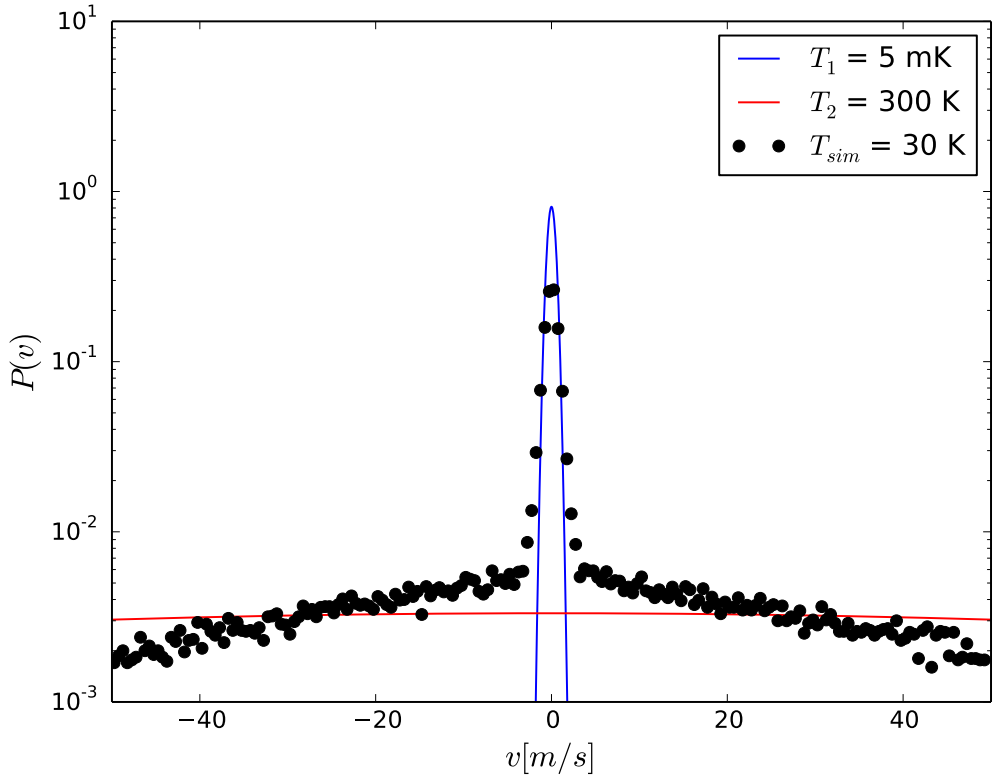

Figure 6.7: Velocity distribution of a single ion in contact with two reservoirs at $T_1 = 5m$K and $T_2 = 300$K with collision frequency ratio $\Gamma_1/\Gamma_2 = 100$.

APPENDIX A

Numerical simulation procedures

We perform two types of Monte Carlo simulations to verify the analytical theory. Their simulation details are described below respectively.

A.1 Type I

In Type I simulation, Eq. 2.5 is integrated numerically with fixed time step Δt using ProtoMol software [100], where Δt is chosen to be much smaller than the rf period Ω^{-1}. Elastic cross-sections σ_{el} are used in every collision. The simulation consists of following four steps,

1. The single ion is initialized at origin and zero velocity, i.e. $\mathbf{r}_0 = \mathbf{0}$, and $\mathbf{v}_0 = \mathbf{0}$. The simulation step index N is set to 0.

2. Ion's new position $\mathbf{r}_{N+1}$ and velocity $\mathbf{v}_{N+1}$ at the next step $N+1$ are calculated by leapfrog integration of Eq. 2.5.

3. To determine if a collision should happen during Δt, an ultracold atom is generated with velocity $\mathbf{v_n}$ sampled from thermal distribution characterized by W_n. The associated collision rate Γ is given by $\rho\sigma_{el}|\mathbf{v_{rel}}|$, where ρ is the density of ultracold atoms, $\mathbf{v_{rel}}$ is the relative velocity, and σ_{el} depends implicitly on the collision energy $\frac{\mu}{2}\mathbf{v_{rel}}^2$ in the center-of-mass frame. A collision happens during Δt if $1 - \exp(-\Gamma\Delta t) < d$, where d is the value of a random dice uniformly distributed in $[0, 1]$. If this is true, simulation then proceeds to S4, otherwise to S2.

4. Ion's velocity after the collision is updated according to Eq. 3.5. The rotation matrix $\mathcal{R}$ is specified by polar angle θ and azimuthal angle ϕ, defined with respect to $\mathbf{v_{rel}}$. θ is

sampled from the probability distribution function $\frac{d\sigma_{el}}{d\theta}\sin\theta$ defined on $[0,\pi]$, and ϕ is sampled from uniform distribution on $[0,2\pi]$. Simulation then loops back to S2, until the prescribed number of collisions have been reached.

A.2 Type II

In Type II simulation, Langevin cross-section σ_L are used instead in collisions. The collision rate Γ thus does not depend on collision energy, allowing for a much faster integration method based on transfer matrix similar to [6]. The simulation consists of following four steps,

1. Same as S1 in Type I simulation, the single ion is initialized at origin and zero velocity. However, a series of collision time $\tau_j (j = 1, 2, 3, \cdots)$ are pre-determined, which follows Poisson distribution with average interval equal to Γ^{-1}.

2. Ion's new coordinate $\mathbf{P}_{i+1} = [x_i, v_{i,x}, y_{i+1}, v_{i+1,y}, z_{i+1}, v_{i+1,z}]^{\mathrm{T}}$ at $\tau = \tau_{i+1}$ are obtained by multiplying the transfer matrix $\mathbf{M}(\tau_{i+1}, \tau_i)$ to $\mathbf{P}_i$. To be more specific, the transfer matrix $\mathbf{M}$ consists of three 2×2 submatrices,

$$\mathbf{M} = \begin{bmatrix} \mathbf{M}_x & \mathbf{0} & \mathbf{0} \\ \mathbf{0} & \mathbf{M}_y & \mathbf{0} \\ \mathbf{0} & \mathbf{0} & \mathbf{M}_z \end{bmatrix} \tag{A.1}$$

   where each submatrix $\mathbf{M}_j$ $(j = x, y, z)$ is given by

$$\mathbf{M}_j(\tau_2, \tau_1) = \frac{1}{w_{0,j}} \begin{bmatrix} c_j(\tau_2)\dot{s}_j(\tau_1) - s_j(\tau_2)\dot{c}_j(\tau_1) & -c_j(\tau_2)s_j(\tau_1) + s_j(\tau_2)c_j(\tau_1) \\ \dot{c}_j(\tau_2)\dot{s}_j(\tau_1) - \dot{s}_j(\tau_2)\dot{c}_j(\tau_1) & -\dot{c}_j(\tau_2)s_j(\tau_1) + \dot{s}_j(\tau_2)c_j(\tau_1) \end{bmatrix} \tag{A.2}$$

3. Collisions further modify ion's velocity according to Eq. 3.5, where $\mathcal{R}$ now represents rotation with equal probability into 4π solid angle. Simulation then loops back to S2, until the prescribed number of collisions have been reached.

APPENDIX B

Experimental/Numerical/Simulation Method

B.1 $\ln\Lambda$ and Chandreshakar-Spitzer Self-Collision Rate

Suppose a "test" ion is initially injected into a plasma with velocity $\mathbf{v}$. For each collision with a "field ion" in the plasma located at impact parameter b, under the approximation of small-angle scattering, some transverse momentum

$$\Delta\mathbf{p}_\perp = \frac{e^2}{2\pi\epsilon_0 v b} \tag{B.1}$$

is imparted to the "test" ion. As the "test" ion moves in the plasma, successive random collisions cause momentum diffusion in the transverse direction. The mean square value of the total transverse momentum $\Delta\mathbf{p}_\perp$, after flight time t, is thus the sum of mean square value of transverse momentum $\Delta\mathbf{p}_{\perp,i}$ for ith collision,

$$\langle\Delta\mathbf{p}_\perp^2\rangle = \langle(\sum_i \Delta\mathbf{p}_{\perp,i})^2\rangle = \sum_i \Delta\mathbf{p}_{\perp,i}^2 \tag{B.2}$$

which is equal to the number of "field ions" in each cylindrical shell of radius b and length vt, integrated over b,

$$\begin{aligned}\langle\Delta\mathbf{p}_\perp^2\rangle &= \int_{b_-}^{b^+} \left(\frac{e^2}{2\pi\epsilon_0 v b}\right)^2 2\pi b db \cdot vt \cdot \rho \\ &= \frac{\rho e^4 \ln\Lambda}{2\pi\epsilon_0^2 v} t\end{aligned} \tag{B.3}$$

where ρ is the ion density, $b_{-,+}$ are the lower and upper impact parameter cut-off, and $\ln\Lambda = \ln(b_+/b_-)$ is the Coulomb logarithm. The appropriate value of b_- and b_+ is mentioned in the introduction.

The "self-collision" rate γ is introduced by Chandreshakar and Spitzer in Ref. [84], whose inverse γ^{-1} characterizes the amount of time for the $\sqrt{\langle\Delta\mathbf{p}_\perp^2\rangle}$ to become equal to mv.

Under the assumption of Maxwell-Boltzmann velocity distribution, $v = \sqrt{3k_BT/m}$, and one obtains,

$$\gamma = \frac{\rho e^4 \ln \Lambda}{2\pi\epsilon_0^2\sqrt{m}(3k_BT)^{3/2}} \tag{B.4}$$

B.2 Ion-Ion Heating Through Micromotion Interruption

Similar to the approach in Chapter 2, the average effect of ion-ion collision on ion's energy W can be derived, except that now the sum of both ion's energy should be considered. Different from ion-neutral collision, upon averaging over the rf-phase and the ensemble, ion-ion collision always leads to heating. For simplicity, let's first consider 1D collisions, and rewrite Eq 3.6. in the following matrix form.

$$W = \frac{m}{2}\mathbf{P}^{\mathrm{T}}\mathbf{N}\mathbf{P} \tag{B.5}$$

where ion's phase-space coordinate $\mathbf{P}$ is a column vector, i.e. $\mathbf{P} = [x, v]^{\mathrm{T}}$, $\mathbf{N}$ is a 2×2 matrix given by

$$\mathbf{N} = \frac{\overline{\dot{c}^2}}{w_0^2}\begin{bmatrix} \dot{c}^2 + \dot{s}^2 & -c\dot{c} - s\dot{s} \\ -c\dot{c} - s\dot{s} & c^2 + s^2 \end{bmatrix} \tag{B.6}$$

As in Chapter 2, the bar denotes the time average.

Now suppose two identical ions a and b initially on their own Mathieu trajectories $\mathbf{P}_a$ and $\mathbf{P}_b$. The total energy of the system before the collision is

$$W = \frac{m}{2}\mathbf{P}_a^{\mathrm{T}}\mathbf{N}\mathbf{P}_a + \frac{m}{2}\mathbf{P}_b^{\mathrm{T}}\mathbf{N}\mathbf{P}_b \tag{B.7}$$

By introducing the center-of-mass and relative coordinates

$$\begin{aligned} \mathbf{P}_{\mathrm{COM}} &= \frac{1}{2}(\mathbf{P}_a + \mathbf{P}_b) \equiv \Big[x_{\mathrm{COM}}, v_{\mathrm{COM}}\Big]^T \\ \mathbf{p} &= \mathbf{P_a} - \mathbf{P_b} \equiv \Big[x, v\Big]^T \end{aligned} \tag{B.8}$$

the total kinetic energy is separated into two parts,

$$W = \frac{2m}{2}\mathbf{P}_{\mathrm{COM}}^T\mathbf{N}\mathbf{P}_{\mathrm{COM}} + \frac{m/2}{2}\mathbf{p}^T\mathbf{N}\mathbf{p} \tag{B.9}$$

At time τ_C, a Coulomb collision occurs which changes the $\mathbf{P}_a$ and $\mathbf{P}_b$ into $\mathbf{P}'_a$ and $\mathbf{P}'_b$. The center-of-mass part of kinetic energy in Eq. (B.9) remains unchanged as a result of conservation of momentum and assumption that average position of two ions barely moves during the collision. Therefore, the energy change is solely from the relative position and velocity,

$$\Delta W = \frac{m/2}{2}\mathbf{p}'^{\mathrm{T}}\mathbf{N}\mathbf{p}' - \frac{m/2}{2}\mathbf{p}^{\mathrm{T}}\mathbf{N}\mathbf{p} \tag{B.10}$$

In the center-of-mass frame, collision flips the sign of the relative velocity, but does not change the relative position,

$$x' = x \quad v' = -v \tag{B.11}$$

Plugging Eq. (B.11) into Eq. (B.10), only the cross-product term xv remains,

$$\Delta W = m\overline{\dot{c}^2}xv\frac{s\dot{s} + c\dot{c}}{w_0^2}\bigg|_{\tau_C} \tag{B.12}$$

To get an average ΔW, Eq. (B.12) needs to be averaged for all possible trajectories $\mathbf{P}_a$'s and $\mathbf{P}_b$'s and all collision time τ_C's [4]. If ions' oscillation amplitudes before the collision are $[A_a, B_a]$ and $[A_b, B_b]$, then

$$\langle\Delta W\rangle = \frac{m\overline{\dot{c}^2}}{w_0^2}\Big(\langle\Delta A^2\rangle\overline{c\dot{c}(s\dot{s} + c\dot{c})} + \langle\Delta B^2\rangle\overline{s\dot{s}(s\dot{s} + c\dot{c})} + \langle\Delta A\Delta B\rangle\overline{(c\dot{s} + s\dot{c})(s\dot{s} + c\dot{c})}\Big) \tag{B.13}$$

where $\Delta A = A_a - A_b$, $\Delta B = B_a - B_b$ and the bracket denotes ensemble average. The last term on the right-hand side of Eq. B.13 vanishes because the time-dependent part is an odd function of time τ_C. The other two terms are related to the total kinetic energy before the collision by

$$\langle\Delta A^2\rangle = \langle\Delta B^2\rangle = 2\langle A^2\rangle = 2\langle B^2\rangle = \frac{\langle\overline{W}\rangle}{\frac{m\overline{\dot{c}^2}}{2w_0^2}} \tag{B.14}$$

Plugging Eq. (B.14) into (B.13), we obtain the result in [4],

$$\langle\Delta W\rangle = \epsilon\langle W\rangle \tag{B.15}$$

where ϵ has been defined in Chapter 2. The numerical value of ϵ is given by Eq 3.16. If the ions are trapped in static trap, like the confining field in z direction, $\epsilon_z = 0$, and there would be no ion-ion heating.

Extending the above discussion to three-dimensional, and getting an analytical expression for ϵ proves to be difficult. For one thing, $\mathbf{N}$ are different in three directions. In particular, $\mathbf{N}_z$ is diagonal as there is no rf-field in the z direction. For another, full differential cross section for Coulomb scattering need to be considered, making simplifications in Eq. (B.11) non-existent in 3D. Although the numerical value of ϵ could be found through simulation, it can simply be approximated by the average value of ϵ in all three directions,

$$\epsilon_{3\mathrm{D}} = \frac{1}{3}\sum_i \epsilon_i \approx \frac{2}{3}(1 + 2q^{2.24}) \tag{B.16}$$

B.3 Determination of ion's initial temperature T_0

After the ensemble of ions have been laser-cooled, T_0 is measured by scanning the laser's detuning from the far red side of the cooling transition to almost zero [1]. The ion's fluorescence follows a Voigt profile, resulting from the convolution of Doppler broadening and Lorentzian profile,

$$V(\delta;\sigma,\gamma) = \int_{-\infty}^{\infty} G(\delta';\sigma)L(\delta-\delta';\gamma)d\delta' \tag{B.17}$$

where δ is the detuning. $G(\delta;\sigma)$ is the centered Gaussian profile:

$$G(\delta;\sigma) = \frac{1}{\sqrt{2\pi}\sigma}\exp\left(-\frac{\delta^2}{2\sigma^2}\right) \tag{B.18}$$

$\sigma(T_0) = \sqrt{\frac{k_B T_0}{mc^2}}\nu_{\mathrm{Yb}^+}$ and ν_{Yb^+} is ion's center transition frequency. $L(\delta,\gamma)$ is the centered Lorentzian profile

$$L(\delta;\gamma) = \frac{1}{\pi}\frac{\gamma}{\delta^2+\gamma^2} \tag{B.19}$$

where $\gamma = \sqrt{1+s}\gamma_{\mathrm{Yb}^+}$ is power-broadened linewidth. γ_{Yb^+} is ion's natural linewidth, $s = I/I_{\mathrm{Yb}^+}$ is the transition saturation parameter, I and I_{Yb^+} are laser's intensity at the location of ion cloud and ion's saturation intensity. The value of ν_{Yb^+}, I_{Yb^+}, γ_{Yb^+} are given in Tab. B.1. T_0 is found from the optimal value of $\sigma(T_0)$ that fits the $V(\delta;\sigma,\gamma)$ to ion's fluorescence profile.

[1] Blue detuning causes rapid heating of ion.

Physical Quantity	Meaning	Value
ν_{Yb^+}	Center transition frequency	369.5 nm
I_{Yb^+}	Saturation intensity	60 mW $\cdot$ cm^{-2}
γ_{Yb^+}	Natural linewidth	20 MHz

Table B.1: Physical property of $^{174}\mathrm{Yb}^+$

B.4 Determination of the number of ions N

The number of $^{174}\mathrm{Yb}^+$ ions, N, is proportional to the photo multiplier voltage V_p at zero detuning $\delta = 0$,

$$V_p = N\beta_{174}\rho_{ee}\gamma_{^{174}\mathrm{Yb}^+}Ge\eta\Omega TR \tag{B.20}$$

where ρ_{ee} is the average fraction of ion's population on the excited state, given by

$$\rho_{ee} = \frac{\Gamma\sqrt{1+s}}{2}\frac{s}{2(1+s)}V(0;\sigma,\gamma) \tag{B.21}$$

The value of various experimental parameters in Eq. B.20 are given in Tab. B.2.

Physical Quantity	Meaning	Value
β_{174}	$^{174}\mathrm{Yb}^+$ isotope abundance	31.8 %
G	PMT Gain	10^7
e	Charge of an electron	1.6×10^{-19}C
η	PMT quantum efficienty	30 %
Ω	Solid angle fraction for photon collection	0.12
T	Optical transmission for $\lambda = nm$	0.27
R	Terminal Resistance	50 Ω

Table B.2: Experimental parameters

B.5 Determination of ion's temperature $T(t)$

As ion's temperature increases due to micro-motion interruption (see Appendix), ion's fluorescence changes, as the combined result of a broadened Doppler profile, and reduced overlap between the ion cloud and cooling laser. To account for these two effects, we make the following assumptions:

1. The laser beam has a Gaussian intensity profile centered at the trap center,

$$I(r,z) = I_0 \exp\left(-\frac{2r^2}{w^2(z)}\right)\left(\frac{w_0}{w(z)}\right)^2 \tag{B.22}$$

   where $w(z) = w_0\sqrt{1+\frac{z^2}{z_R^2}}$ and $z_R = \frac{\pi w_0^2}{\lambda}$. Because the size of ion cloud along the z direction is typically smaller than z_R of the laser beam, $w(z)$ can be assumed to be constant and equal to w_0, which simplifies Eq. B.22 to

$$I(r) = I_0 \exp\left(-\frac{2r^2}{w_0^2}\right) \tag{B.23}$$

2. Ion cloud is aligned with the trap center. Ion's density $\rho(r;T)$ is described by Eq. 4.4, namely for $T < T_p$, ion's density is saturated at ρ_{max}, and

$$\rho(r,T) = \rho_0 \exp(-\frac{m\omega_r^2 r^2}{2k_B T}) \tag{B.24}$$

   for $T > T_p$, where w_r is the ion's secular frequency in the radial direction.

Then ion's fluorescence $F(t)$ at time t is proportional to the product of density and Voigt profile integrated along the radial direction,

$$F(\delta,t) \propto \int_0^\infty V(\delta;\sigma(T),\gamma(I(r)))\rho(r;T)2\pi r dr \tag{B.25}$$

The dependence of σ, γ on $T(t)$ is written out explicitly. The exact proportionality factor is not relevant, because experimentally the ratio of fluorescence

$$x = \frac{F(\delta,t)}{F(\delta,0)} \tag{B.26}$$

is measured, from which $T(t)$ can be solved numerically.

A minimum of 10% experimental uncertainty is assigned to the fluorescence ratio, to reflect the noisy nature of measurement. As presented in Fig. 4.1 in the manuscript, close to the phase transition, this method yields a temperature which depends sensitively on the fluorescence ratio. Therefore, a 90% threshold value of fluorescence ratio is compared with each time, above which the temperature is simply set to the initial T_{sec}.

APPENDIX C

ProtoMol Manual

C.1 Introduction

ProtoMol is an "object-oriented, component based, framework for molecular dynamics (MD) simulations". Written in C++, ProtoMol can simulate classical mechanical systems with very high accuracy and efficiency. For a detailed review of ProtoMol, see Ref [100]. In the remainder of this manual, we first explain the ProtoMol installation process, then we detail the usage of ProtoMol and its add-ons. At last, we describe the processing of writing customized add-ons for future simulation studies.

C.2 Obtaining ProtoMol

ProtoMol is an open-source and cross-platform software hosted at SourceForge. Considerable modifications have been added for simulations in this dissertation, so it is highly recommended to have the modified version to start with, which can be found at github https://github.com/kuangchen/ProtoMol. Any git tool should be able to clone this online repository into local copies.

C.3 Compiling ProtoMol

To compile modified ProtoMol, a C++ compiler compatible with C++11 standard is needed. Modified ProtoMol also depends on two external library, Lua v5.2 and HDF5 v1.8.10, which can be found in the package repository (for Linux system) or downloaded

online (for Windows system) at the following URL,

- LUA http://code.google.com/p/luaforwindows/
- HDF5 http://www.hdfgroup.org/HDF5/release/obtain5.html

The compilation and installation process is automated by CMAKE tool. On Linux system, installation is accomplished by the following commands,

```
# Remove previous CMakeCache and CMakeFiles folder
rm -rf CMakeCache.txt CMakeFiles

# Turn on build_lapack switch and set the build_lapack_type to lapack
cmake -DBUILD_LAPACK=ON -DBUILD_LAPACK_TYPE=lapack

# Tell cmake to generate Makefiles
cmake .

# Install ProtoMol into system folder
sudo make install
```

The basic usage of CMAKE is documented at http://www.cmake.org/cmake/help/documentation.html. To toggle other build switches (cluster computing, $\cdots$), see CMAKELISTS.TXT for detail.

C.4 Basic Usage

To start a simulation a user needs to provide a configuration file (in plain text) that defines simulation initial conditions, integrator, outputs, and other properties of simulation. These entries are organized in the format of self-explanatory "keyword - value" pairs. The definition of integrators and forces have their own special syntax. A sample configuration file is presented below, with the meaning of each entry explained in the comment line. To see a full list of keywords, please see Ref [100, 134].

```
# Number of steps in simulation
numsteps 100000000

# The number assigned to the first step
firststep 0

# Random Number seed
seed 11

# Initial temperature of particles
temperature 1e4

# Simulation cell size
cellsize 5000000

# Boundary Conditions
boundaryConditions vacuum

# Cell Manager
cellManager Cubic
exclude none

# Initial position and velocitiy definition
posfile ion_neutral_cooling_ini_pos_32.xyz
psffile ion_neutral_cooling_32.psf

# Par file definition
parfile ion_neutral_cooling.par

# Output Setting
outputfreq 10000

# Add IonSnapshot as the output
IonSnapshot ss.lua
```

```
# Integrator Setting
integrator {
  # 0th level integrator
  level 0 LeapfrogBufferGas {
    timestep 1e8
    filename buffer_gas.lua

    # Add Coulomb force between ions
    force Coulomb
    -algorithm NonbondedSimpleFull

    # Add ion trap force
    force LQT
    -lqt_filename trap.lua
  }
}
```

C.5 Using ProtoMol Add-Ons

A set of new forces, integrators and outputs have been added specifically to simulate ion trap dynamics, whose usage are detailed below.

C.5.1 New Forces

Rf-trapping force

Rf-trapping force is defined with the following syntax,

```
force LQT
    -lqt_filename your_file
```

where LQT is the name of the force, and the argument of -lqt_filename, i.e. -your_file is a LUA file that defines an ion trap.

The trap definition declares a variable named trap, a LUA table that contains the mass of the ion in the trap, the physical dimensions of the trap and the trap voltage. A sample trap definition file is given below, where the meanings of each filed are the same as in Eq. 2.2 and their units are given in the comment.

```
trap = {
  m = 173,          -- AMU
  r0 = 12e-3,       -- m
  z0 = 21.5e-3,     -- m
  v_rf = 175/2,     -- V (Note arithmetic operations can be done in Lua file)
  v_ec = 10,        -- V
  eta = 0.1275,     -- 1
  omega = 300e3     -- Hz
}
```

Harmonic static trapping force

The harmonic static trap is introduced to simulate ion dynamics under the secular approximation, in which ions are confined by a harmonic potential with the trapping frequency equal to ion's secular frequency. Harmonic trapping force is defined with the following syntax,

```
force HarmonicTrapForce
    -ht_def your_file
```

where HarmonicTrapForce is the name of the force, and the argment of -ht_filename, i.e. -your_file is a LUA file that defines an harmonic trapping force.

The trap definition declares a variable trap, a Lua table that contains a single field freq, which in turn contains three fields x, y, z. A sample trap definition file is given below,

```
trap = {
  freq = { x = 39.63e3 * 2 * 3.14159,
           y = 39.63e3 * 2 * 3.14159,
           z = 39.63e3 * 2 * 3.14159
         }
}
```

The meanings and units of these fields are given in the following Tab. C.1.

Field	Unit	Meaning
`trap.freq.{x,y,z}`	Hz	$\omega_{x,y,z}$ as defined in $V = \frac{1}{2}(\omega_x^2 x^2 + \omega_y^2 y^2 + \omega_z^2 z^2)$

Table C.1: Harmonic trap definition syntax.

Damping force

The damping force, *i.e.* $\mathbf{F} = -b\mathbf{v}$, is introduced to emulate the laser-cooling force, which quickly removes ions' kinetic energy, and cause the ions to form Coulomb crystal. Damping force is defined with the following syntax,

```
force DampingForce
    -damping_def your_file
```

where `DampingForce` is the name of the force, and the argment of `-damping_def`, i.e. `-your_file` is a LUA file that defines a damping force.

The trap definition declares a variable `damping` that contains the damping magnitude, and when the damping is on. A sample damping definition file is given below,

```
damping = {
  coeff = 3e-22,
  t_start = -1,
```

```
  t_end = 0.01
}
```

The meanings and units of the fields in the `damping` table are given in Tab. C.2.

Field	Unit	Meaning
`coeff`	?	damping coefficient b, defined by $\mathbf{F} = -b\mathbf{v}$
`t_start`	s	start time. Laser is on only when `t_start` $\leq$ t $\leq$ `t_end`.
`t_end`	s	end time

Table C.2: Damping force definition file

C.5.2 New Integrators

Buffer-gas Leapfrog Integrator V2

A leapfrog integrator is introduced to simulate random collisions with ultracold neutral atoms. It is defined with the following syntax,

```
level X LeapFrogBufferGas2 {
  timestep 1e8
  filename your_file
}
```

where `LeapFrogBufferGas2` is the name of the integrator, and the argument of `filename`, i.e.`your_file` is a LUA file that defines the buffer gas integrator, by declaring a table variable `neutral`. A sample buffer-gas leapfrog integrator definition file is given below

```
neutral = {
  mass = 40,
  polarizability = 50,
  temperature = 5e-3,
```

```
  density = 1e16
}
```

The meanings and units of the fields in the `neutral` table are given in Tab. C.3

Field	Unit	Meaning
`mass`	AMU	Mass of neutral atom
`polarizability`	10^{24}cm^3	Polarizability of neutral atom
`temperature`	K	Temperature of neutral atom
`density`	m^3	Density of neutral atom

Table C.3: Buffer-gas leapfrog integrator definition file

C.5.3 New output

Ion Snapshot

At each simulation time step, ions' positions and velocities form a *frame*. A consecutive series of *frames* form a *snapshot*. For analysis at a later time, an end user might want to record an array of snapshots starting at different time t_i ($i = 1, 2, 3, \cdots$) during the simulation, and for simplify, let's suppose every snapshot contains the same number of frames. It is defined with the following syntax,

```
  IonSnapshot your_file
```

where `your_file` is a LUA file that defines the ion snapshots.

The `IonSnapshot` definition declares a table variable `ss` that contains the number of snapshots, and frames in each snapshot. A sample `IonSnapshot` definition is given below,

```
start_time = {}
```

```
for i=1, 50 do
   start_time[i] = (i-1) * 2e-2
end

ss = {
  num_frame = 250,
  start = start_time
  dir = ./
}
```

Ion Snapshot syntax

The meanings and units of the fields in the `ss` table are given in Tab. C.4

Field	Type	Unit	Meaning
`num_frame`	integer	1	N_f, if set to -1, then N_f is set to number of steps in the longest secular periods in x, y, z three directions
`start`	table	sec	t_i, i.e. the start time of each snapshot
`dir`	string	N/A	The name of directory where snapshot files are stored

Table C.4: Snapshot Definition

All the snapshot files are stored under the same directory, specified by the `dir` keywords in the definition file. They are named by the pattern snapshot_i.hd5, where i ranges from 0 to $N_s - 1$.

The snapshot files are stored in HDF5 format, for its compact size and support by major programming languages, including C/C++/Python/Matlab. For an overview of HDF5 file, visit its official website at http://www.hdfgroup.org/HDF5/. Shown in Fig. C.2, every HDF5 file has a hierachical data structure, similar to the file system in an operating system. In addition to N_f consecutive frames, a `config` header is also included which con-

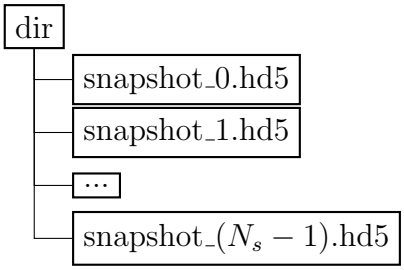

Figure C.1: Directory structure of snapshot output.

sists of auxillary information intended to make the snapshot file self-inclusive. The meanings of various fields in `config` is explained in Fig. C.5.

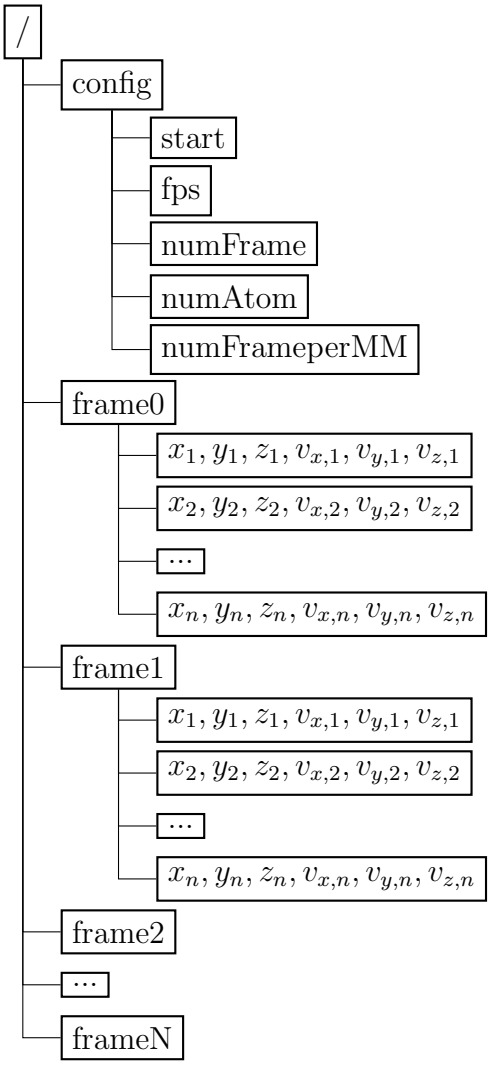

Figure C.2: File structure of each snapshot file

Field	Type	Unit	Meaning
`start`	float	s	Start time of the snapshot
`fps`	integer	1	Number of frames per second
`numFrames`	integer	1	Number of frames in the snapshot
`numAtoms`	integer	1	Number of atoms in the simulation
`numFrameperMM`	integer	1	Number of frames in one micromotion period

Table C.5: Snapshot config header

C.6 Writing ProtoMol Add-Ons

ProtoMol makes use of object-oriented programming language, and it has been carefully designed to ensure extensibility for new model encapsulation. How to add new modules to ProtoMol is beyond the scope of this thesis. For interested readers, it is recommended to read Ref. [135], combined with the newest ProtoMol source code to

References

[1] P. F. Staanum, K. Hø jbjerre, P. S. Skyt, A. K. Hansen, M. Drewsen, Nat. Phys. 6 (4) (2010) 271–274.

[2] S. T. Sullivan, W. G. Rellergert, S. Kotochigova, K. Chen, S. J. Schowalter, E. R. Hudson, Phys. Chem. Chem. Phys 13 (42) (2011) 18859–63.

[3] S. J. Schowalter, K. Chen, W. G. Rellergert, S. T. Sullivan, E. R. Hudson, Rev. Sci. Inst. 83 (4) (2012) 043103.

[4] Y. Moriwaki, M. Tachikawa, Y. Maeno, Jpn. J. Appl. Phys 31 (1992) L1640–L1630.

[5] F. Major, H. Dehmelt, Phys. Rev. 170 (1) (1968) 91–107.

[6] R. DeVoe, Phys. Rev. Lett. 102 (6) (2009) 1–4.

[7] G. Dimonte, J. Daligault, Phys. Rev. Lett. 101 (13) (2008) 135001.

[8] E. Lifshitz, L. Pitaevskii, Physical Kinetics, Elsevier, Butterworth & Heinemann, Oxford, 2006.

[9] W. G. Rellergert, S. T. Sullivan, S. J. Schowalter, S. Kotochigova, K. Chen, E. R. Hudson, Nature 495 (7442) (2013) 490–4.

[10] J. J. Hudson, D. M. Kara, I. J. Smallman, B. E. Sauer, M. R. Tarbutt, E. A. Hinds, Nature 473 (7348) (2011) 493–6.

[11] M. Kozlov, D. DeMille, Phys. Rev. Lett. 89 (13) (2002) 133001.

[12] a. C. Vutha, W. C. Campbell, Y. V. Gurevich, N. R. Hutzler, M. Parsons, D. Patterson, E. Petrik, B. Spaun, J. M. Doyle, G. Gabrielse, D. DeMille, J. Phys. B: At. Mol. Opt. Phys. 43 (7) (2010) 074007.

[13] D. DeMille, S. B. Cahn, D. Murphree, D. a. Rahmlow, M. G. Kozlov, Phys. Rev. Lett. 100 (2) (2008) 023003.

[14] V. Flambaum, M. Kozlov, Phys. Rev. Lett. 99 (15) (2007) 1–4.

[15] E. Hudson, H. Lewandowski, B. Sawyer, J. Ye, Phys. Rev. Lett. 96 (14) (2006) 143004.

[16] D. DeMille, S. Sainis, J. Sage, T. Bergeman, S. Kotochigova, E. Tiesinga, Phys. Rev. Lett. 100 (4) (2008) 043202.

[17] K.-K. Ni, S. Ospelkaus, D. Wang, G. Quéméner, B. Neyenhuis, M. H. G. de Miranda, J. L. Bohn, J. Ye, D. S. Jin, Nature 464 (7293) (2010) 1324–8.

[18] M. Baranov, Phys. Rep. 464 (3) (2008) 71–111.

[19] G. Pupillo, A. Micheli, P. Zollerarxiv:arXiv:0805.1896v1.

[20] D. DeMille, Phys. Rev. Lett. 88 (6) (2002) 1–4.

[21] S. Yelin, K. Kirby, R. Côté, Phys. Rev. A 74 (5) (2006) 050301.

[22] L. D. Carr, D. DeMille, R. V. Krems, J. Ye, New J. Phys. 11 (5) (2009) 055049.

[23] M. T. Hummon, M. Yeo, B. K. Stuhl, A. L. Collopy, Y. Xia, J. Ye, Phys. Rev. Lett. 110 (14) (2013) 143001.

[24] E. S. Shuman, J. F. Barry, D. Demille, Nature 467 (7317) (2010) 820–3.

[25] K.-K. Ni, S. Ospelkaus, M. H. G. de Miranda, A. Pe'er, B. Neyenhuis, J. J. Zirbel, S. Kotochigova, P. S. Julienne, D. S. Jin, J. Ye, Science (New York, N.Y.) 322 (5899) (2008) 231–5.

[26] J. Weinstein, Nature 190 (June) (1998) 148–150.

[27] J. Koelemeij, B. Roth, a. Wicht, I. Ernsting, S. Schiller, Phys. Rev. Lett. 98 (17) (2007) 173002.

[28] K. C. Cossel, D. N. Gresh, L. C. Sinclair, T. Coffey, L. V. Skripnikov, A. N. Petrov, N. S. Mosyagin, A. V. Titov, R. W. Field, E. R. Meyer, E. a. Cornell, J. Ye, Chem. Phys. Lett. 546 (2012) 1–11.

[29] E. Meyer, J. Bohn, M. Deskevich, Phys. Rev. A 73 (6) (2006) 062108.

[30] S. Schiller, V. Korobov, Phys. Rev. A 71 (3) (2005) 032505.

[31] J. H. V. Nguyen, C. R. Viteri, E. G. Hohenstein, C. D. Sherrill, K. R. Brown, B. Odom, New J. Phys. 13 (6) (2011) 063023.

[32] J. Nguyen, B. Odom, Phys. Rev. A 83 (5) (2011) 1–7.

[33] X. Tong, A. Winney, S. Willitsch, Phys. Rev. Lett. 105 (14) (2010) 1–4.

[34] K. Mölhave, M. Drewsen, Phys. Rev. A 62 (1) (2000) 11401.

[35] A. Ostendorf, C. Zhang, M. Wilson, D. Offenberg, B. Roth, S. Schiller, Phys. Rev. Lett. 97 (24) (2006) 1–4.

[36] B. Roth, a. Ostendorf, H. Wenz, S. Schiller, J. Phys. B: At. Mol. Opt. Phys. 38 (20) (2005) 3673–3685.

[37] A. Bertelsen, S. Jörgensen, M. Drewsen, J. Phys. B: At. Mol. Opt. Phys. 39 (5) (2006) L83–L89.

[38] T. Schneider, B. Roth, H. Duncker, I. Ernsting, S. Schiller, Nat. Phys. 6 (4) (2010) 275–278.

[39] E. R. Hudson, Phys. Rev. A 79 (3) (2009) 1–9.

[40] W. Federer, W. Dobler, F. Howorka, W. Lindinger, M. Durup-Ferguson, E. E. Ferguson, J. Chem. Phys. 83 (3) (1985) 1032.

[41] P. Schwerdtfeger, Atomic static dipole polarizabilities, in: Computational Aspects of Electric Polarizability Calculations: Atoms, Molecules and Clusters, IOS Press, Amsterdam, 2006, Ch. 1, pp. 1–32.

[42] P. Langevin, Ann. Chim. Phys 5 (1905) 245.

[43] A. Grier, M. Cetina, F. Oručević, V. Vuletić, Phys. Rev. Lett. 102 (22) (2009) 223201.

[44] L. Ratschbacher, C. Zipkes, C. Sias, M. Köhl, Nat. Phys. 8 (9) (2012) 649–652.

[45] S. T. Sullivan, W. G. Rellergert, S. Kotochigova, E. R. Hudson, Phys. Rev. Lett. 109 (22) (2012) 223002.

[46] R. J. Saykally, R. C. Woods, Ann. Rev. Phys. Chem. 32 (1) (1981) 403–431.

[47] E. Hirota, Chem. Rev. 92 (1) (1992) 141–173.

[48] D. Schuster, L. Bishop, I. Chuang, D. DeMille, Phys. Rev. A (2011) 9.

[49] R. March, J. Mass. Spec. 32 (1997) 351–369.

[50] W. Demtröder, Laser Spectroscopy: Basic Concepts and Instrumentation, third edit Edition, Springer Verlag, New York, 2003.

[51] K. Chen, S. Schowalter, S. Kotochigova, A. Petrov, W. Rellergert, S. Sullivan, E. Hudson, Phys. Rev. A 83 (3) (2011) 1–4.

[52] C. Zipkes, S. Palzer, C. Sias, M. Köhl, Nature 464 (7287) (2010) 388–91.

[53] C. Zipkes, S. Palzer, L. Ratschbacher, C. Sias, M. Köhl, Phys. Rev. Lett. 105 (13) (2010) 133201.

[54] F. H. J. Hall, M. Aymar, N. Bouloufa-Maafa, O. Dulieu, S. Willitsch, Phys. Rev. Lett. 107 (24) (2011) 243202.

[55] W. G. Rellergert, S. T. Sullivan, S. Kotochigova, A. Petrov, K. Chen, S. J. Schowalter, E. R. Hudson, Phys. Rev. Lett. 107 (24) (2011) 243201.

[56] S. Schmid, A. Härter, J. H. Denschlag, Phys. Rev. Lett. 105 (13) (2010) 133202.

[57] L. Ratschbacher, C. Sias, L. Carcagni, J. M. Silver, C. Zipkes, M. Köhl, Phys. Rev. Lett. 110 (16) (2013) 160402.

[58] K. Chen, S. T. Sullivan, W. G. Rellergert, E. R. Hudson, Phys. Rev. Lett. 110 (17) (2013) 173003.

[59] H. J. Metcalf, P. Van Der Straten, Laser Cooling and Trapping, Vol. 39, 1999.

[60] M. H. Anderson, J. R. Ensher, M. R. Matthews, C. E. Wieman, E. a. Cornell, Science (New York, N.Y.) 269 (5221) (1995) 198–201.

[61] R. Grimm, M. Weidemüller, Y. B. OvchinnikovarXiv:9902072.

[62] S. Earnshaw, Trans. Camb. Phil. Soc 7 (1842) 97–112.

[63] M. Abramowitz, I. A. Stegun, Handbook of mathematical functions with formulas, graphs, and mathematical tables, Dover Publications, New York, 1964.

[64] P. H. Dawson, Quadrupole mass spectrometry and its applications, American Institute of Physics, 1995.

[65] D. J. Douglas, A. J. Frank, D. Mao, Mass Spectrom. Rev 24 (2005) 1–29.

[66] S. Haze, S. Hata, M. Fujinaga, T. MukaiyamaarXiv:arXiv:1305.3346v1.

[67] S. Lee, K. Ravi, S. a. Rangwala, Phys. Rev. A 87 (5) (2013) 052701.

[68] M. Drewsen, a. Mortensen, R. Martinussen, P. Staanum, J. Sø rensen, Phys. Rev. Lett. 93 (24) (2004) 243201.

[69] B. Gao, Phys. Rev. Lett. 104 (21) (2010) 213201.

[70] M. Cetina, A. T. Grier, V. Vuletić, Phys. Rev. Lett. 109 (25) (2012) 253201.

[71] R. DeCarvalho, J. Doyle, B. Friedrich, T. Guillet, J. Kim, D. Patterson, J. Weinstein, Eur. Phys. J. D 7 (3) (1999) 289.

[72] H. Friedrich, Theoretical Atomic Physics, third edit Edition, Springer Verlag, New York, 2005.

[73] B. R. Johnson, J. Chem. Phys. 67 (9) (1999) 4086.

[74] P. Zhang, A. Dalgarno, R. Côté, Phys. Rev. A 80 (3) (2009) 030703.

[75] A. Dalgarno, M. R. C. McDowell, A. Williams, Phil. Trans. R. Soc. A 250 (982) (1958) 411–425.

[76] C. Zipkes, L. Ratschbacher, C. Sias, M. Köhl, New J. Phys. 13 (5) (2011) 053020.

[77] W. Campbell, E. Tsikata, H.-I. Lu, L. van Buuren, J. Doyle, Phys. Rev. Lett. 98 (21) (2007) 213001.

[78] T. Baba, I. Waki, Appl. Phys. B 74 (4-5) (2002) 375–382.

[79] H. Takayasu, M. Takayasu, Phys. Rev. Lett. 79 (6) (1997) 966–969.

[80] H. Kesten, Acta Math. 131 (1) (1973) 207–248.

[81] S. Atzeni, J. Meyer-Ter-Vehn, The Physics of Inertial Fusion: Beam Plasma Interaction, Clarendon Press, Oxford, 2004.

[82] G. Werth, V. Gheorghe, F. Major, Charged Particle Traps II: Applications, Springer Series on Atomic, Optical, and Plasma Physics, Springer, 2009.

[83] L. Landau, Phys. Z. Sowjetunion 10 (1936) 154.

[84] L. Spitzer, Physics of Fully Ionized Gases, John Wiley, New York, 1962.

[85] L. Brown, D. Preston, R. Singleton Jr, Charged particle motion in a highly ionized plasma, Phys. Rep. 410 (4) (2005) 237–333.

[86] D. Gericke, M. Murillo, M. Schlanges, Phys. Rev. E 65 (3) (2002) 036418.

[87] L. X. Benedict et al., Phys. Rev. Lett. 102 (20) (2009) 205004.

[88] A. Mostovych et al., Phys. Rev. Lett. 66 (5) (1991) 612–615.

[89] A. Ng et al., Phys. Rev. E 52 (4) (1995) 4299–4310.

[90] G. Drake, Springer Handbook of Atomic, Molecular, and Optical Physics, Vol. 1, Springer, 2005.

[91] J. Schiffer, Phys. Rev. Lett. 61 (16) (1988) 1843–1846.

[92] V. Ryjkov, X. Zhao, H. Schuessler, Phys. Rev. A 71 (3) (2005) 033414.

[93] C. Zhang et al., Phys. Rev. A 76 (1) (2007) 012719.

[94] R. Blatt et al., Z. Phys. D. 4 (2) (1986) 121–126.

[95] I. Siemers et al., Phys. Rev. A 38 (10) (1988) 5121–5128.

[96] R. Blümel et al., Phys. Rev. A 40 (2) (1989) 808–823.

[97] D. J. Berkeland et al., J. Appl. Phys. 83 (10) (1998) 5025.

[98] J. Wesenberg et al., Phys. Rev. A 76 (5) (2007) 053416.

[99] L. Verlet, Phys. Rev. 159 (1) (1967) 98–103.

[100] T. Matthey et al., ACM Trans. Math. Softw. 30 (3) (2004) 237–265.

[101] D. Dubin, Phys. Rev. Lett. 66 (16) (1991) 2076–2079.

[102] S. G. Brush, H. L. Sahlin, E. Teller, J. Chem. Phys. 45 (6) (1966) 2102.

[103] J. Huba, NRL Plasma Formulary, NRL publication, Naval Research Laboratory, 1998.

[104] T. Monz et al., Phys. Rev. Lett. 106 (13) (2011) 130506.

[105] A. del Campo et al., Phys. Rev. Lett. 105 (7) (2010) 075701.

[106] H. Landa et al., Phys. Rev. Lett. 104 (4) (2010) 043004.

[107] M. Drewsen et al., Phys. Rev. Lett. 81 (14) (1998) 2878–2881.

[108] P. Blythe et al., Phys. Rev. Lett. 95 (18) (2005) 183002.

[109] S. Willitsch, M. T. Bell, A. D. Gingell, T. P. Softley, Phys. Chem. Chem. Phys. 10 (2008) 7200.

[110] D. Smith, Chem. Rev. 92 (7) (1992) 1473–1485.

[111] V. Reddy, S. Ghanta, S. Mahapatra, Phys. Rev. Lett. 104 (2010) 111102.

[112] J. Berkowitz, K.-. Groeneveld (Eds.), Molecular Ions: Geometric and Electronic Structures, Plenum Press, 1983.

[113] M. Duncan, Int. J. Mass. Spec. 200 (1-3) (2000) 545–569.

[114] A. Svendsen et al., Rev. Sci. Inst. 81 (2010) 073107.

[115] U. Hechtfischer et al., J. Chem. Phys. 127 (2007) 204304.

[116] Y. Hashimoto et al., Jap. J. Appl. Phys. 45 (2006) 7108.

[117] M. Henyk, F. Costache, J. Reif, Applied Surface Science 186 (1-4) (2002) 381–384.

[118] L. A. Kaledin, M. C. Heaven, R. W. Field, J. Mol. Spectrosc. 193 (285).

[119] P. Banks, Planet. Space Sci. 14 (11) (1966) 1105–1122.

[120] J. Sugar, V. Kaufman, J. Opt. Soc. Am. 69 (1979) 141–143.

[121] G. Karlström, R. Lindh, P.-Å. Malmqvist, B. O. Roos, U. Ryde, V. Veryazov, P.-O. Widmark, M. Cossi, B. Schimmelpfennig, P. Neogrady, L. Seijo, Computational Material Science 28 (2003) 222.

[122] S. Kotochigova, A. Petrov, E. Hudson, Prospects for cooling heavy molecular ions, In preparation.

[123] E. A. Gislason, J. Chem. Phys. 58 (9) (1973) 3702.

[124] C. J. Williams, K. F. Freed, J. Chem. Phys. 85 (1986) 2699.

[125] S. Kotochigova, P. S. Julienne, E. Tiesinga, Phys. Rev. A 68 (2003) 022501.

[126] O. Vallée, M. Soares, Airy Functions and Applications to Physics, Imperial College Pressh, London, 2004.

[127] H. Lefebvre-Brion, R. W. Field, The Spectra and Dynamics of Diatomic Molecules: Revised and Enlarged Edition, Academic Press, 2004.

[128] E. J. Heller, J. Chem. Phys. 68 (5) (1978) 2066.

[129] R. Frey, R. Kakoschke, K. Müller-Dethlefs, E. W. Schlag, Z. Phys. Atom. Nucl. 307 (1) (1982) 25–29.

[130] R. J. L. Roy, LEVEL 8.0 A Computer Program for Solving the Radial Schrödinger Equation for Bound and Quasibound Levels, Tech. Rep. April 2007, University of Waterloo, Ontario, Canada (2012).

[131] R. J. L. Roy, G. T. Kraemer, BCONT 2.2 A Computer Program for Calculating Bound to Continuum Transition Intensities for Diatomic Molecules, Tech. Rep. August, Univeristy of Waterloo, Ontario, Canada (2004).

[132] B. Derrida, J. Stat. Mech. Theo. Exp 2007 (2007) P07023–P07023.

[133] C.T.J.Alkemade, N. Kampen, D.K.C.MacDonald, Proc. Roy. Soc. London. A, Math. Phys. Sci.

[134] ProtoMol Ver. 2.0.3 - Quick Reference (2005).

[135] ProtoMol Ver. 2.0.3 - How-To Guide (2006).